DEPARTMENT OF PHYSICS
UNIVERSITY OF JYVÄSKYLÄ
RESEARCH REPORT No. 11/2014

Ultrasound Measurements in Bone Using an Array Transducer

Vantte Kilappa

Academic Dissertation
for the Degree of
Doctor of Philosophy

To be presented, by permission of the
Faculty of Mathematics and Natural Sciences
of the University of Jyväskylä,
for public examination in Auditorium FYS-1 of the
University of Jyväskylä on December 12, 2014
at 12 o'clock noon

UNIVERSITY OF JYVÄSKYLÄ
JYVÄSKYLÄ, FINLAND 2014

ABSTRACT

Osteoporosis is a prevalent bone disease, especially common among elderly individuals. It is characterized by increased fragility, caused by age-related resorption of the bone mineral content. In particular, osteoporotic resorption affects increase of porosity, decrease of elastic stiffness and thinning of the cortical wall. Osteoporotic fractures cause human suffering and heavy burdens to the economy, but the present clinical standard of diagnosing, dual energy X-ray absorptiometry (DXA), cannot reliably predict whether an individual will later sustain a fracture. Moreover, these devices are expensive and do not permit screening. There is thus a call for alternative approaches. Quantitative ultrasound (QUS) methods have shown promise in development of new alternative modalities for rapid, reliable and inexpensive screening and diagnosing of osteoporosis. As a part of this progress, this Thesis focuses on the development of a new array ultrasound probe, suitable for QUS assessment of the human radius and tibia.

The new probe was tested in an *in vivo* study on pre- and postmenopausal females (n=254), whose fracture history was recorded and who were also measured by other techniques. The array probe was used to measure the first arriving signal (FAS). It was shown that ultrasound assessment with this device predicted well bone mineral density and cortical thickness at the bone sites analyzed, especially in the radius. In the subset of postmenopausal subjects, the ability of the method to differentiate fractures was consistent to that of X-ray-based bone densitometry (including DXA), and could thereby be used for screening of osteoporosis.

Another emphasis in the Thesis relates to excitation and detection of a fundamental flexural guided wave (FFGW), a mode which is especially sensitive to cortical thickness. It is hard to detect this mode *in vivo* because it features weak amplitude and it is disturbed by other US modes which propagate in the layer of soft tissue on top of the bone. In one sub-study, a new signal processing method was introduced to determine the velocity of FFGW from signals measured by the array probe developed. In another sub-study, it was predicted by numerical simulations that this array probe can be configured as a phased array of sources. In particular, it was predicted that phased excitation can sufficiently gain the signal-to-interference ratio of FFGW on top of the soft tissue coating, so as to enable *in vivo* assessment of this mode.

In conclusion, results suggest that it is possible to develop a multi-mode QUS assessment utilizing both FAS and FFGW. Such a method would significantly improve the inference of different bone properties that determine its fracture toughness. Multi-mode QUS is thus expected to significantly improve the clinical relevance of US methods.

Keywords: quantitative ultrasound, axial transmission, guided waves, cortical bone, bone mineral density, cortical thickness, osteoporosis, fracture risk, finite-element simulations

Author Vantte Kilappa
Department of Physics
University of Jyväskylä
Jyväskylä, Finland

Supervisor Dr. Petro Moilanen
Department of Physics
University of Jyväskylä
Jyväskylä, Finland

Supervisor Prof. Jussi Timonen
Department of Physics
University of Jyväskylä
Jyväskylä, Finland

Reviewers Associate Prof. Michal Pakula
Institute of Mechanics and Applied Computer Science
Kazimierz Wielki University
Bydgoszcz, Poland

Reviewers Prof. Jari Hyttinen
Department of Electronics and Communications Engineering
Tampere University of Technology
Tampere, Finland

Opponent Prof. Kay Raum
Julius-Wolff-Institut & Berlin-Brandenburg School for Regenerative Therapies
Charité - Universitätsmedizin Berlin
Berlin, Germany

ISSN 0075-465X
ISBN 978-951-39-5864-0 (nid.)
ISBN 978-951-39-5865-7 (PDF)

YHTEENVETO (FINNISH SUMMARY)

Osteoporoosi on merkittävä ikääntymiseen liittyvä luuston sairaus, jossa luun lujuuden heikentyminen altistaa murtumille. Murtolujuus määräytyy luun geometriasta, mikrorakenteesta, vaihduntanopeudesta, mikrovaurioista, mineralisaatioasteesta ja kollageenin rakenteesta. Nämä tekijät heijastuvat luun mineraalitiheyteen, elastisiin ominaisuuksiin ja kuoriluun paksuuteen. Nykyisin käytössä oleva diagnostiikkamenetelmä, kaksienerginen röntgentutkimus (DXA), mittaa ainoastaan mineraalitiheyttä ja sillä on siksi rajallinen kyky ennustaa murtuman todennäköisyyttä yksilötasolla. DXA ei myöskään mahdollista tehokasta seulontaa laitteistojen korkean hinnan vuoksi. Kvantitatiivinen ultraääni (QUS) on yksi lupaavimmista vaihtoehdoista edulliseksi ja luotettavaksi osteoporoosin seulontamenetelmäksi, sillä QUS-mittaus kertoo myös elastisuudesta ja kuorikerroksen paksuudesta. Tämä väitöstutkimus liittyy kuoriluun mittaukseen perustuvan QUS-menetelmän kehittämiseen. Työssä kehitettiin värttinä- ja sääriluun *in vivo* -mittaukseen soveltuva sarja-anturi.

Uutta sarja-anturia testattiin *in vivo* -tutkimuksessa, jossa sillä mitattiin naispuoleisia koehenkilöitä laajassa ikäryhmässä (n=254) keskittyen niin sanotun ensin saapuvan aallon (FAS) mittaukseen. Vertailun vuoksi koehenkilöt mitattiin myös röntgenpohjaisilla menetelmillä ja heidän murtumahistoriansa kirjattiin ylös. Tulokset osoittivat, että QUS-laitteen määrittämä ultraäänen etenemisnopeus ennusti hyvin luun mineraalitiheyttä ja kuoriluun paksuutta, erityisesti värttinäluussa. Lisäksi menopaussin ohittaneilla koehenkilöillä QUS-menetelmä erotteli murtumahistorian omaavat koehenkilöt verrokeista yhtä hyvin tai paremmin kuin käytössä olleet röntgenmenetelmät, mukaanlukien DXA. Kehitetty QUS-menetelmä voisi siten soveltua seulontaan.

Väitöstutkimuksen toinen osa keskittyi niin sanotun taipuma-aallon (FFGW) lähettämiseen ja havaitsemiseen luusta. FFGW on erityisen herkkä kuoriluun paksuuden muutoksille ja sen mittaaminen mahdollistaa kuoriluun paksuuden arvioinnin. FFGW-mittauksen haasteena on se, että FFGW näkyy heikosti pehmytkudoksen pinnalla ja on vaikeasti erotettavissa voimakkaista häiriöistä jotka johtuvat ultraäänen kulkeutumisesta pehmytkudoksessa. Työn tavoitteena oli näiden haasteiden ratkaiseminen mallintamalla ja kokeellisin mittauksin. Yhdessä osatutkimuksessa testattiin uutta signaalinkäsittelymenetelmää FFGW:n nopeuden määrittämiseen sarja-anturilla mitatuista signaaleista. Toisessa osatutkimuksessa arvioitiin tietokonesimulaation avulla sarja-anturin käyttöä vaiheistettuna lähettimenä FFGW:n vahvistamiseksi. Arvioidut menetelmät paransivat merkittävästi FFGW:n havaittavuutta pehmeän kuorikerroksen läpi ja voivat siis mahdollistaa taipuma-aallon *in vivo* -mittauksen.

Väitöstutkimuksessa osoitettiin, että yhden moodin QUS-mittaus (FAS) voi mahdollistaa ultraäänipohjaisen seulonnan. Lisäksi tutkimuksen tulokset mahdollistavat kahden tai useamman moodin QUS-menetelmän (FAS ja FFGW) kehittämisen. Kahteen tai useampaan moodiin perustuvan menetelmän odotetaan parantavan luun ominaisuuksien arviointitarkkuutta ja murtumariskiennusteen luotettavuutta perinteelliseen yhden moodin QUS-mittaukseen verrattuna.

Asiasanat: kvantitatiivinen ultraääni, aksiaalinen ultraäänimenetelmä, ohjatut aallot, kuoriluu, luun mineraalitiheys, kuoriluun paksuus, osteoporoosi, murtumariski, FEM-simulaatiot

ACKNOWLEDGEMENTS

The work reported in this thesis was done during the years 2007-2014 (the first years of which I was still a masters student) in the departments of Physics and Health Sciences in the University of Jyväskylä.

I wish to extend my heartfelt thanks to Dr. Petro Moilanen, who was my supervisor during all this time. Without his immense work effort and patience, I surely would not be writing this paragraph. I'm also very grateful to Prof. Shulin Cheng and especially Prof. Jussi Timonen, to whom I owe a great deal of thanks for a huge amount of assistance and additional supervision. To all of you, I'm sorry that this took such a long time.

Further, I would like thank my other co-authors, Markku Alen, Edward Haeggström, Erkki Heikkola, T. Jämsä, Mikko Määttä, Patrick Nicholson, Risto Myllylä, Ari Salmi, Dean Ta, Kailiang Xu, Leiting Xu and Zuomin Zhao for their contributions towards the associated articles, and Jari Hyttinen and Michal Pakula for reviewing this thesis and giving a large amount of valuable critique.

The whole Tomography group of the Physics department and CALEX group of the Health Sciences department deserve thanks for their work camaraderie, but I would especially like to thank the FL-125 crew & associates Jarno Alaraudanjoki, Axel Ekman, Antti Juutilainen, Topi Kähärä, Johan Lindgren, Keijo Mattila, Timo Riikilä and Tuomas Tallinen for innumerable hours of *important* lunchtime discussions and advice during the years. In truth, this courtesy should be extended to the rest of my friends, but the length of such a list would border on the ridiculous. You know who you are.

The (direct and indirect) financial support from the University of Jyväskylä, Ellen and Artturi Nyyssönen Foundation, TEKES and the Academy of Finland is greatly appreciated.

Finally, I would like to thank my wife Elina. For everything, in the first place, but also for making me feel like a human being during these last stress-filled months.

ACRONYMS

2D-FFT	Two dimensional fast Fourier transform (section 5.3.2).
A0	The first asymmetric guided wave mode in plates (section 3.2).
AUC	Area under curve. In this work, the fraction of graph area under the receiver operator characteristic (ROC) curve
AT	Axial transmission (section 3.3.3)
BMC	Bone mineral content
BMD	Bone mineral density
BSI	Bone strength index
BUA	Broadband ultrasound attenuation
CC	The crazy climber mode separation method (section 5.3.3).
CSA	Cross-sectional area
CSMI	Cross-sectional moment of inertia
DXA	Dual-energy X-ray absorptiometry (section 2.5.1)
F1	The first guided wave mode in tubes and cylinders (section 3.2).
FAS	First arriving signal, a hybrid mode between longitudinal ultrasound vibration and the S0 guided wave mode (section 3.2).
FFGW	Fundamental flexural guided wave mode. The lowest order guided wave component detected in a given situation, typically A0 or BL1 (section 3.2).
GF	Group velocity filtering (section 5.3.2)
LF	Low frequency. In the context of this book, this means ultrasound in the range of tens or hundreds of kHz.
OR	Odds ratio
pQCT	peripheral quantitative computer tomography (section 2.5.2)
QUS	Quantitative ultrasound
RMS	Root mean square
RMSE	Root mean square error
ROC	Receiver operator characteristic
S0	The first symmetric guided wave mode in plates (section 3.2).
SCV	Standardized coefficient of variation
SIR	Signal-to-interference ratio
SoS	Speed of sound
SSI	Strength-strain index
STFT	Short-time Fourier transform (section 5.3.3)
T-score	In BMD calculations, the number of standard deviations from the mean for young healthy refrences.
TFR	Time-Frequency Representation (section 5.3.3)
$\mathbf{V_{FAS}}$	The speed of a low-frequency FAS pulse, mainly used for FAS velocity results from the array ultrasound device (section 5.1).
$\mathbf{V_{LF}}$	Used in place of V_{FAS} in I.
Z-score	In BMD calculations, the number of standard deviations from the age-matched mean.

LIST OF PUBLICATIONS

I V. Kilappa, P. Moilanen, L. Xu, P. H. F. Nicholson, J. Timonen, S. Chen. Low-frequency axial ultrasound velocity measurements in children and adults: correlations with bone mineral density and cortical thickness in the radius and tibia. *Osteoporos Int, 22(4):1103*, 2011.

II P. Moilanen, M. Määttä, V. Kilappa, L. Xu, P. H. F. Nicholson, M. Alén, J. Timonen, T. Jämsä, S. Cheng. Discrimination of fractures by low-frequency axial transmission ultrasound in postmenopausal females. *Osteoporos Int, 24(2):723–730*, 2013.

III V. Kilappa, K. Xu, P. Moilanen, E. Heikkola, D. Ta, J. Timonen. Assessment of the fundamental flexural guided wave in cortical bone by an ultrasonic axial-transmission array transducer. *Ultrasound Med Biol, 39(7):1223–1232*, 2013.

IV V. Kilappa, P. Moilanen, A. Salmi, Z. Zhao, E. Haeggström, J. Timonen, R. Myllylä. Tailoring the excitation of fundamental flexural guided waves in coated bone by phase-delayed array: two-dimensional simulations. *submitted for publication*, 2014.

The author is the principal author of publications **I**, **III** and **IV**. His role in publication **II** includes collection (measuring), management and analysis of ultrasound and pQCT data. Moreover, he has contributed to the following papers.

V P. Moilanen, M. Talmant, V. Kilappa, P.H.F. Nicholson, S. Cheng, J. Timonen, P. Laugier. Modeling the impact of soft tissue on axial transmission measurements of ultrasonic guided waves in long bones. *J Acoust Soc Am, 124(4):2364–2373*, 2008

VI P. Moilanen, V. Kilappa, A. Salmi, P. Karppinen, E. Haeggström, Z. Zhao, R. Myllylä, J. Timonen. Photo-acoustic phase-delayed excitation of guided waves in coated bone phantoms. *Proceedings of IEEE International Ultrasonics Symposium, 2080–2083*, 2013

VII P. Moilanen, Z. Zhao, P. Karppinen, T. Karppinen, V. Kilappa, J. Pirhonen, R. Myllylä, E. Haeggström, and J. Timonen. Photo-acoustic excitation and optical detection of fundamental flexural guided wave in coated bone phantoms. *Ultrasound Med Biol, 40(3):521–531*, 2014

VIII V. Kilappa, P. Moilanen, A. Salmi, P. Karppinen, E. Haeggström, Z. Zhao, R. Myllylä, J. Timonen. Obstructing propagation of interfering modes improves detection of guided waves in coated bone models. *Proceedings of IEEE International Ultrasonics Symposium, xxxx-xxxx, (submitted for publication)*, 2014

CONTENTS

1 INTRODUCTION

Osteoporosis is a significant health problem, as treatment of 3-4 million fragility fractures which occur each year in the EU cause an economic burden of approximately 30 billion euros (status of the year 2000) (Alzahouri et al., 2013) and cause, in addition, functional disability and human suffering. Yet, the annual rate of fractures is increasing, and for example in the US, it is expected to grow 50% by the year 2025 (Burge et al., 2007). Hence, there is a great socioeconomic call for early identification, prevention and treatment of osteoporosis.

The present clinical standard for diagnosing osteoporosis is dual-energy X-ray absorptiometry (DXA), but its ability to predict fractures is limited (Bolotin and Sievänen, 2001; Stone et al., 2003). This limitation is explained by the fact that DXA measures an average bone mineral content from a 2D projection and cannot assess bone's microstructure (e.g. porosity) and elastic properties, which are important factors in the fracture toughness (Griffith and Genant, 2008). Moreover, DXA is expensive enough to make it less useful for screening purposes.

Quantitative ultrasound (QUS) has been suggested to answer this call (Langton et al., 1984; Laugier, 2008). Ultrasound is sensitive to elastic properties, porosity and geometrical features of the bone. Moreover, it enables development of inexpensive devices which are relatively easy to use and do not involve ionizing radiation. These features of QUS make it suitable especially for screening.

The QUS approaches can be distinguished based on the type of the bone, trabecular or cortical, they are designed for. The QUS devices used clinically at present are mostly based on an assessment of the trabecular bone at the heel or at the ends of long bones such as the radius (Bréban et al., 2010; Glüer et al., 2004; Stein et al., 2013), utilizing a through-transmission technique (TT). Speed of sound (SOS) through the heel, and broadband ultrasound attenuation (BUA) on this site, have both been shown to predict fractures at the hip and (Hans et al., 1996; Khaw et al., 2004) spine (Heaney et al., 1995). During the past two decades, research interests have shifted to development of QUS techniques for the assessment of cortical bone in the shafts of long bones, such as the radius, tibia and femur (Barkmann et al., 2000; Foldes et al., 1995; Talmant et al., 2009). These approaches mainly rely on an axial transmission technique (AT), i.e. transmission

of ultrasound along the long axis of the bone (Camus et al., 2000), originally defined by Siegel et al. (1958), although TT has also been applied, for the femoral neck (Barkmann et al., 2007) in particular. AT-QUS of cortical bone has shown to exhibit good sensitivity to porosity and elastic properties of bone (Bossy et al., 2004c; Lee et al., 1997; Muller et al., 2008; Raum et al., 2005), bone mineral density (Moilanen et al., 2003; Muller et al., 2005) and cortical thickness (Bossy et al., 2004b; Njeh et al., 1999a).

Earlier work of our research group has introduced a low frequency (50-350 kHz) AT technique (LF-AT-QUS) for assessment of guided waves in the human radius and tibia (Moilanen, 2004). This approach combines measurement of the first arriving signal (FAS) and a fundamental flexural guided wave (FFGW). While FAS is measured by majority of AT-QUS techniques, at approximately 1 MHz frequency, it has shown to exhibit sensitivity mainly to the properties of periosteal cortical bone (Muller et al., 2005). Advantage of using lower frequencies (longer wavelength) is an enhanced sensitivity to cortical thickness (Bossy et al., 2004b; Njeh et al., 1999a) and endosteal parts of the cortical bone, (Haïat et al., 2009; Tatarinov et al., 2005) i.e. to the region where osteoporotic changes occur. The other mode, FFGW, has shown sensitivity to cortical thickness in particular (Muller et al., 2005), and has permitted an accurate ultrasonic evaluation of the cortical thickness in human radius *in vitro* (Moilanen et al., 2007a,b,c).

Because of a number of limitations, an *in vivo* application of the LF-AT-QUS technique has proven to be challenging. The device setup developed by Moilanen as part of his PhD thesis (2004) was bulky and featured poor *in vivo* reproducibility (Määttä, 2009), mainly because the mechanism did not permit proper correction for the impact of soft tissue tapering. While FAS has nevertheless been well excited and detected, it has been shown that there are additional obstacles in the proper detection of FFGW on top of the soft tissue covering. Magnitude of this mode is rapidly damped by the soft tissue, while, on the other hand, the soft tissue permits propagation of disturbing ultrasound modes which interfere at the receiver with FFGW. It has been shown that it is difficult to distinguish FFGW from these interfering disturbances. (Moilanen et al., 2008)

The purpose of this Thesis is to both test the clinical feasibility of a further development of our LF-AT-QUS method, to test the feasibility of this method for FFGW measurement and to address the challenges imposed by the soft tissue layer on FFGW excitation and detection. First, a new array transducer was developed to improve the reproducibility of the FAS measurement. The first half of the Thesis focused on *in vivo* testing of the new array transducer. The second part of the Thesis focused on a more fundamental analysis of the capability of the array transducer to permit an *in vivo* assessment of FFGW. To this end, a sub-study focused on the improvement of signal processing, and specifically on extraction of FFGW properties from data captured with the array transducer. Another sub-study addressed a tailored excitation of FFGW, so as to improve the reliability of FFGW detection on top of the soft tissue layer by enhancing the power ratio between FFGW and interfering disturbances.

2 BONE AND OSTEOPOROSIS

2.1 Structure and function

Skeleton is a network of connective tissues, which forms the framework of a body. Along with ligaments, muscle and tendons, it supports the body's weight and shields internal organs. It also acts as a storage for minerals (phosporous, calcium) and fat, and is used to temporarily store toxic materials such as heavy metals.

Human bone is a light weight, composite material formed mostly by calsium phosphate (hydroxylapatite, $Ca_{10}(PO_4)_6(OH)_2$) and other minerals which give the bone its characteristic hardness, ridigity and compressive strength. These inorganic materials amount to approximately 70% of the wet mass of live bone (Njeh et al., 1999b). The organic matrix of bone is mostly composed of a protein called type I collagen which gives bones elasticity, toughness and nucleation sites for mineral components.

Basically, bone can be categorized into cortical and trabecular bone. Cortical bone is also known as compact bone and trabecular bone as cancellous bone. These terms are used interchangeably. Cortical bone forms the outer layer of bone and the shafts of long bones such as tibia, radius and femur. It is designed to withstand compression and tensile stress, and is a dense material with little porosity ($5 - 30\%$). At first glance, cortical bone seems completely solid, but actually has a delicate microstructure formed by pipelike bone cell formations (osteons) and a series of small canals (fig. 1, fig. 3a).

The smallest open spaces are called lacunae, which host single osteocytes. Osteocytes are mature bone cells, which network with other osteocytes and exchange nutrients through the microscopic canaliculi. They form cylindrical patterns called osteons, which surround slightly larger (varies, but on the average have a diameter of 50 μm (Gray, 1918)) capillary structures called Haversian canals. These canals house nerve fibres and capillaries, and are used for transporting blood and minerals through the bone tissue (fig. 1). The cocentric cylinders of collagen fibrils around Harvesian canals or the sheets at the surface of the

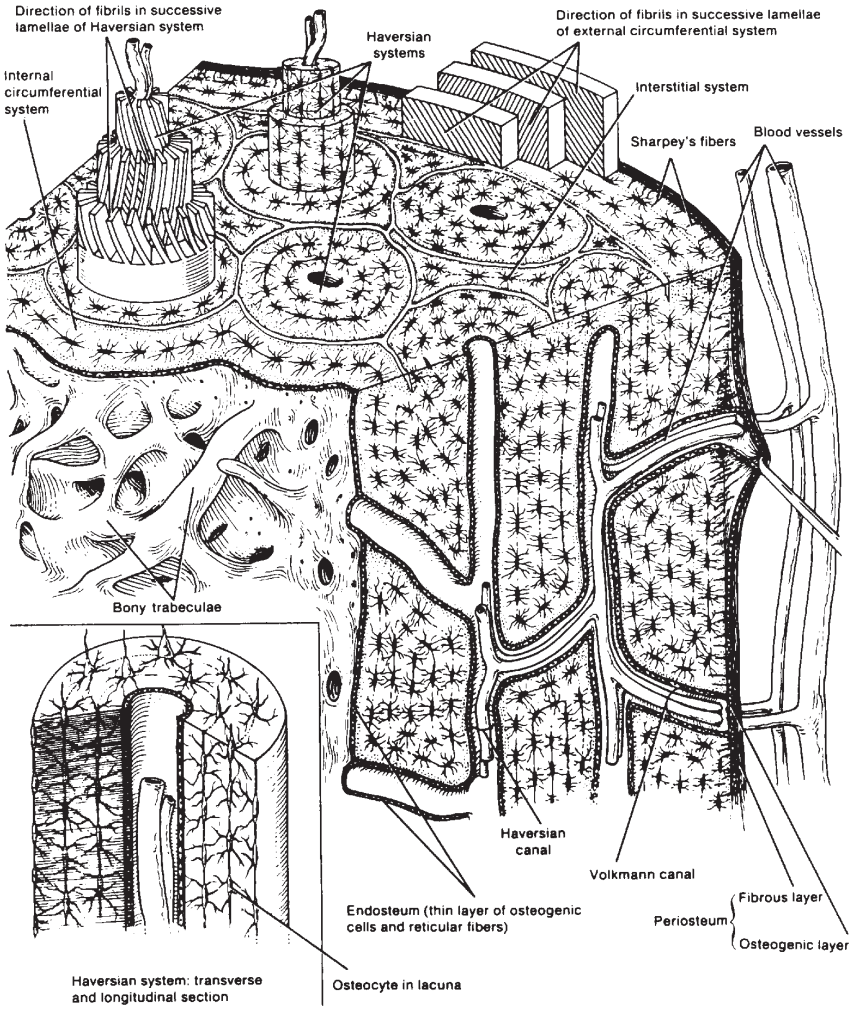

FIGURE 1 Internal structure of cortical bone (image after Buckwalter et al. (1995)).

bone are called lamellae (hence the term lamellar bone). Fibrils can also organize randomly instead of in planar patterns, creating a structure called woven bone. This is mainly seen at early stages of bone growth, and at sites, where structural damage is being repaired. In any case, woven bone will eventually be replaced by lamellar bone.

Trabecular bone is found in places of an asymmetric stress distribution, *i.e.* at the ends of long bones (*i.e.* femur, radius), inner surfaces of cortical bones (the same bones), large flat bones (scapula, pelvic girdle) and in irregularly shaped sections such as vertebrae. In trabecular bone, osteocytes arrange into trabeculae instead of osteons – in place of lamellae, trabeculae form a foamy, honeycomb like network consisting of interconnecting pillars and plates (fig. 3b). As such, porosity of the trabecular bone is much higher than that of the cortical bone ($30-90\%$) (Hall, 2007). This sparse grid of bone material is weaker than that of cortical bone, but optimized for assymetric load and bone mass instead of tensile stress, and requires less resources to construct.

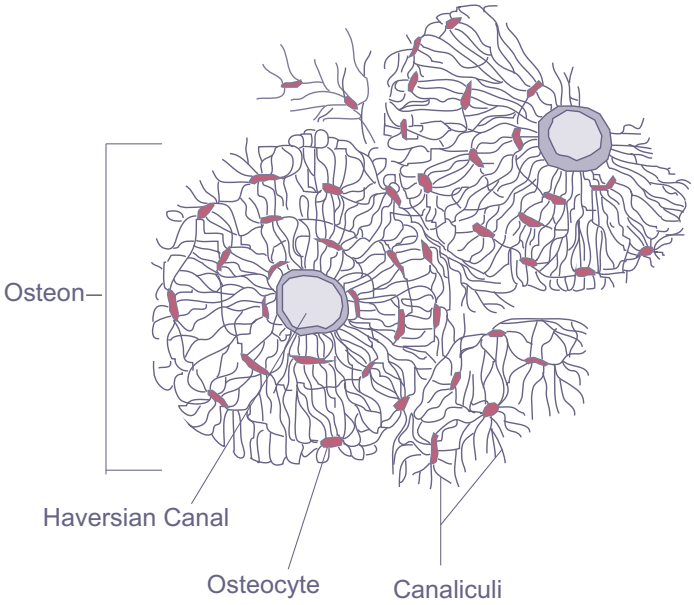

FIGURE 2 Osteons and lacunae (image after Gray (1918)).

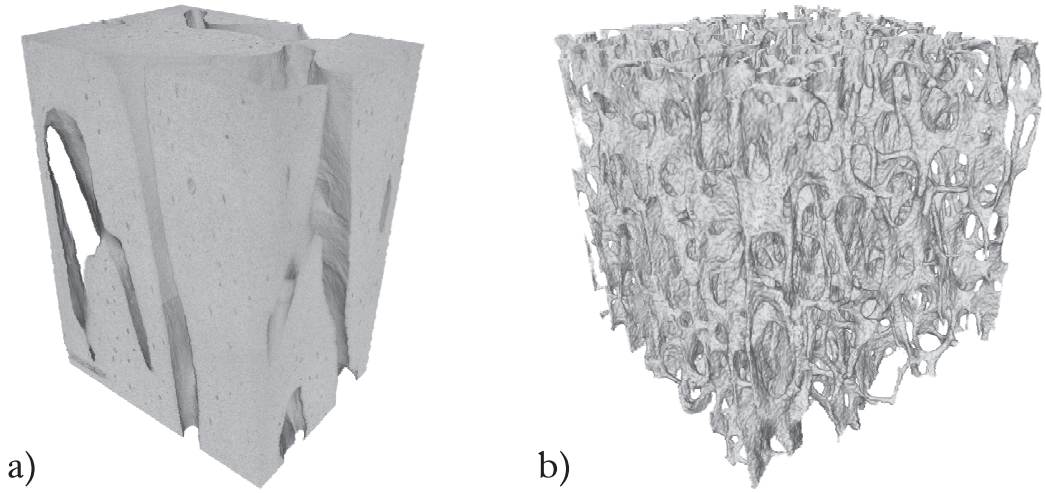

FIGURE 3 Microtomographic images of human (a) cortical bone structure at the proximal end of a femur and (b) trabecular bone structure at the distal end of a femur. Haversian canals can be seen in (a) and the typical network-like structure of cancellous bone in (b). The cortical bone volume imaged is approximately 0.7 mm $\times$ 0.6 mm $\times$ 1 mm, and in the trabecular case, each edge of the volume is 7.8 mm long (images by J. Pirhonen, University of Jyväskylä).

Because of the high surface area of trabecular bone, most of the mineral exchange between the skeleton and the rest of the body happens here. Likewise, trabecular networks have more space for blood vessels and bone marrow, being also the sites of formation of blood cells.

2.2 Life cycle

All bone consists of both live and dead cells, as it is constantly reorganized and remodelled by cells specialiced for this purpose – osteoblasts and osteoclasts. Osteoblasts form bone at the endo- and periosteal surfaces of bones, altering their sizes and shapes. They produce the organic matrix of collagen protein, called osteoid, and also secrete hormones and enzymes which later affect the mineralization process. Eventually they are entrapped in the matrix of the bone and become mature bone cells, osteocytes. Osteoclasts, on the other hand, are large, multinuclear cells derived from macrophages, which perform general immunological defense duties. Instead of engulfing and consuming material, osteoclasts secrete enzymes which destroy bone, forming resorption pits (Howship's lacunae).

Together, these cells form units that continually renew and remodel bone, called bone multicellular units (or basic multicellular units, BMUs). During youth, this process forms new bone, as the activity of osteoblast is higher, while in adulthood, the resorption and formation processes are ideally balanced, sustaining the mass and shape of the skeleton. To give an idea of the speed of this turnover process, approximately 10% of the skeleton is recreated each year in mature humans (Manolagas, 2000).

As humans age, balance of these turnover processes is disturbed, increasing the resorption rate and beginning a gradual deteoriration of bone mass (Alleyne et al., 2012; Seeman and Delmas, 2006). Peak bone mass is achieved between 20–30 years of age, and before death, females eventually lose 35–40% of their cortical and 55–60% of their trabecular bone, while males experience approximately two thirds of this loss. This effect reduces the density of bone, decreases bone strength and fracture resistance, and in severe cases, leads to a bone condition called osteoporosis.

2.3 Mechanical properties

In simple numbers, when the durability of bone is considered in the longitudinal axis of long bones, it has a compressive strength of approximately 170 MPa, a tensile strength of 104–121 MPa and a shear strength of 51.6 MPa (Turner et al., 2001). Thus, it resists compressive forces well, but any force not directed parallel to the axis of the lamellae fractures it more easily. Also, as the osteons travel along the long axis of bone, bone structure is radially symmetric. These types of material are called transversely isotropic. For a more specific look at the type of elasticity modelling used in the experimental part of this work, see section 5.5.1.

However, when discussing bone strength, various effects come to play a role. Typical terms used are the bone quantity and bone quality. Bone quantity simply measures the absolute amount of bone, while quality is a less clearly defined term. In current discussion, it is usually understood to simply mean the

TABLE 1 Physical and chemical characteristics of bone at various length scales (from Hernandez et al).

Scale (m)	Characteristics
$> 10^-3$	Bone size and shape
	Spatial distribution of BMD
10^-6 to 10^-3m	Microarchitecture
	Porosity
	Cortical Thickness
	Lacunar number and morphology
	Remodelling cavity number and morphology
10^-9 to 10^-6	Mineral and collagen distribution and alignment
	Microdamage
$< 10^-9$	Collagen structure and cross-linking
	Mineral type and crystal alignment
	Collagen-mineral interfaces

resistance to fracture (fig. 4), which in turn is explained by various material and structural properties such as mineral density, porosity, microporosity, shape and elastic parameters (Bouxein, 2006; Hernandez and Keaveny, 1996; Seeman, 2008). A length scale chart of these features is shown in table 1. The bone turnover process, mentioned earlier, affects all of the relevant parameters, and thus the whole concept of bone strength.

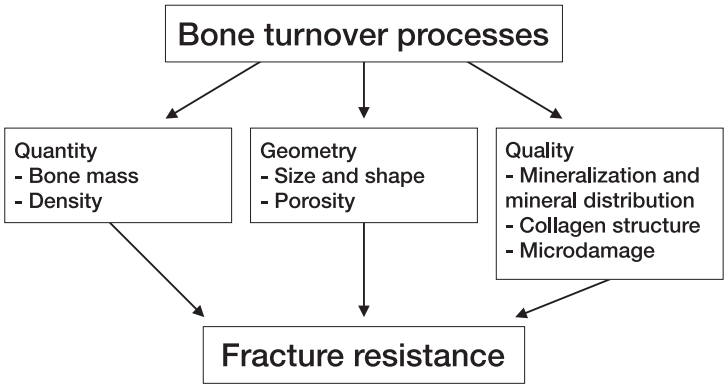

FIGURE 4 Various parameters which affect the fracture risk of bone (after Määttä (2012)).

Of these parameters, bone mineral density (BMD, g/cm^3) and bone mineral content (BMC, g) can be accurately measured by the dual X-ray absorptiometry (DXA) and peripheral quantitative computed tomography (pQCT) methods. They measure directly the amount and density of the inorganic matrix inside

bones, and especially BMD is a good predictor of fracture risk (Cummings et al., 1993, 2002; Marshall et al., 1996; Nguyen et al., 2005; Stegman et al., 1996). Because of resolution limitations, porosity and microporosity are invisible to these methods.

Several measures have been defined to quantify the macroscopic shape and size of the bone. These include bone strength indces, BSI_{CSMI} and BSI_{CSA}, of which the first is defined as $BMD \times CSMI$, and the second as $BMD \times CSA$, where CSMI denotes cross-sectional moment of inertia (moment of inertia without density information) and CSA a cross-sectional area (Martin, 1991). A similar term, the strength-strain index (SSI), is a quantity determined from pQCT images (section 2.5.2) by:

$$SSI = \sum_i \frac{r_i^2 a \left(\frac{CD}{ND}\right)}{r_{max}}, \tag{1}$$

where r_i is the distance from the considered pixel to the centre of gravity and r_{max} is the maximum radial distance among the bone voxels in the image; a is the area of the pixel and CD is its apparent density, while ND is the normal reference value for density (Y. Hasegawa and Reiners, 2001).

In practice the SSI and CSMI parameters measure the radial distribution of the bone mineral content in order to predict its bending and compressional strength, and they are normalized to increase as the bending strength of the object increases. For example, a thin-walled cylinder resists bending and torsional loads better if its radius is larger, while its other parameters remain constant (Bouxein, 2006), and the moment of inertia increases if the mass distribution is driven further away from the main axis. These are relevant both because they are geometric preditors of bone quality (Macdonald et al., 2006; Siu et al., 2003) and because body uses the same principles to combat deterioration of the bone mass. To overcome loss of the bone mass, which arises from old age, bone material is transported further away from the central axis, as bone forms on the periosteal surface (Seeman, 2008) of long bones.

In a microstructure scale, parameters which affect bone quality are microporosity and the elasticity parameters (Young's modulus, Poisson ratio and the directional stiffness coefficents), arising from the quality of the bone matrix. Unlike BMD and geometry, these typically cannot be measured from live specimens because of the high radiation doses required to obtain a sufficient resolution, or because distinguishing their effects from each other is difficult. Measuring stress-strain curves for determination of elastic moduli usually also requires destruction of the sample in question. As such, the relationships between microstructure and elastic properties are usually determined from cadavers through acoustic microscopy or microtomography (Raum et al., 2006a,b), and are correlated with macroscopic propertied obtained by destructive means. However, all of these parameters affect the propagation speeds or attenuation properties of the bulk (section 3.1) and guided waves (section 3.4), and they can be approximated by

other methods such as axial transmission of US (Baron et al., 2007; Muller et al., 2008; Raum et al., 2005; Sasso et al., 2008) (see section 3.3.3).

2.4 Osteoporosis

Osteoporosis is a common disease related to bone metabolism and is defined as a "disease characterized by low bone mass and micro-architectural deterioration of bone tissue, leading to enhanced bone fragility and consequent increase in fracture risk" (Consensus Development Conference, 1993). Currently it is defined through its primary method of diagnosis, dual energy X-ray absorptiometry, wherein a BMD result of more than 2.5 standard deviations (T-score) below the mean of young, healthy adult population is considered osteoporosis. A value between 1 and 2.5 SD below the mean is called osteopenia, and anything above this is considered normal.

During aging, and especially in older females, estrogen deficiency after menopause disrupts the balance of bone resorption. Remodelling rate is increased both through increased activation rate of BMUs, and because the duration of the resorption phase is prolonged (Manolagas, 2000; Hughes et al., 1996). During the course of the disease, BMD is reduced, bone microarchitecture deteriorates and the organic matrix is altered. Densely mineralized bone is replaced by a less dense inorganic matrix and bone stiffness decreases, while orientation of the collagen fibrils in the the organic matrix is altered, decreasing its toughness (Wang et al., 2002). Porosity increases as resorbed loci remain empty for longer periods or even permanently, making the structure more susceptible to microcracks.

As trabecular bone has more surface area for resorption, it is affected first and faster. Trabecular struts are lost and plates perforated, weakening the structure. This is also seen at the endosteal surfaces of long bones and other trabecular-cortical interfaces. This process propagates into the cortical bone, increasing endosteal porosity, manifesting in a lower effective cortical thickness (Bousson et al., 2001; Rosen, 2004; Seeman, 2003; Zebaze et al., 2010). Osteoporotic bone is less able to repair microcracks and other imperfections, which start to accumulate. The thus weakened bone is more susceptible to fatigue, and can sustain less loading cycles than a more compact bone, leading to increased fragility (Burr, 2011; Diab et al., 2006).

TABLE 2 WHO guidelines for osteoporosis diagnosis.

Category	T-Score	% of young women
Normal	T-Score ≥ -1.0	85%
Osteopenia	$-1.0 >$ T-Score > -2.5	14%
Osteoporosis	T-Score ≤ -2.5	0.6%
Severe osteoporosis	T-Score ≤ -2.5 with a fragility fracture	$\approx 0\%$

Osteoporosis can be caused by a number of diseases and conditions of the metabolism, by which it is categorized into primary and secondary osteoporosis. The primary one is related to normal bone aging processes and metabolism, and does not seem to be associated with any other illnesses. It is categorized into postmenopausal (type 1) and senile (type 2) osteoporosis, which occurs after an age of 75 years. Type 1 osteoporosis is naturally exclusive to females, but senile osteoporosis also occurs in males, although it is twice as common in females. However, due to the later age of the onset and lower life expectancy of males than females, the prevalence of osteoporosis among males is much lower than among females.

Secondary osteoporosis is associated with diseases inducing hormonal imbalance (e.g. hyperthyroidism), other diseases (rheumatoid arthritis), medications adversely affecting bone remodelling (glucocorticoids) or simpler causes such as malnutrition or lack of exercise. As bone remodelling is based on the load characteristics which bones experience during normal use, mechanical stimulation is essential for the preservation of the skeleton (Hind and Burros, 2006; Iwamoto et al., 2001). Immobilization rapidly weakens the skeleton and lengthy bedrest, wheelchair use or low-load enviroments such as space flight, cause a rapid loss of the bone mass (LeBlanc et al., 2007).

Progress of osteoporosis can be slowed by proper nutrition, exercise and certain medications such as hormone therapy and biophosponate treatment (Lindsay et al., 1999). While the usefulness of vitamin D and calcium supplements has been questioned, a recent meta-analysis suggests that they can reduce the fracture risk and the rate of BMD loss (Tang et al., 2007).

2.4.1 Fracture risk and cost to society

Osteoporosis significantly decreases the quality of life of the patient, and results in a large financial burden to society. It is difficult to accurately assess the prevalence of osteoporosis, as the disease is typically symptomless until the first adverse effects such as low impact fractures (with the low impact fracture meaning a fracture from light trauma, which would not cause a fracture in a healthy individual). Numerous estimates are presented in the literature. Tarantino et al. (2008) estimate the prevalence at 200 million subjects worldwide, and Wasnich (1999) estimates around 30% of the postmenopausal females in the US being osteoporotic, with another 54% having osteopenia, while it has been estimated, that 23% of all Italian females have osteoporosis, with the prevalence increasing to 45% for persons above 70 years of age (Piscitelli et al., 2011). Worldwide prevalence in developed countries has been estimated as 20% in women after 70 and 40% in women after 80 years (J. A. Kanis on behalf of WHO Scientific Group, 2007). Likewise, it is estimated that 9 million osteoporotic fractures occur annually around the world with 3-4 million in Europe, causing direct health care costs of more than 30 billion euros (Johnell and Kanis, 2006; Kanis and Johnell, 2005). 40-50% of females are expected to suffer an osteoporotic fracture during their lifetime (Johnell and Kanis, 2005).

Of osteoporotic fractures, the hip fracture is most dangerous, as it has a high mortality rate of 15-30% (Keene et al., 1993; Parker and Johansen, 2006), and the majority of deaths occur within the first year after the incident. In addition, hip fractures limit movement and reduce the patients' ability to care for themselves, with 60% requiring assistance a year later and 40% being unable to walk on their own (Kanis and Johnell, 2005). 0.9 million hip fractures happen in Europe each year, with approximately 1.6 million worldwide (Cooper et al., 2011) (data from the year 2000). However, both worldwide and in Finland, there are data showing that the incidence of hip fracture has plateaued during recent years (Cooper et al., 2011; Kannus et al., 2006) to 293/100000 in females and 180/100000 in males (Kanis et al., 2012), but these numbers may rise as the life expectancy and average age of populations are expected to increase in the future (Marks, 2011). In Finland, the unit costs for a hip fracture vary between 14000 €and 36000 €, depending on whether the patient required institutionalization (Nurmi et al., 2003; Sund et al., 2011), and similar figures have been reported in other countries (Budhia et al., 2012; Nikitovic et al., 2013; Zethraeus et al., 1997). In France, Maravic et al. (2005) report median costs of approximately 8000-8700 euros for a hip fracture hospitalization, with hip fractures comprising 82% of the osteoporotic fractures which require hospitalization (data from the year 2001).

2.5 Current X-ray based diagnosis methods

2.5.1 Dual energy X-ray absorptiometry (DXA)

DXA (sometimes DEXA) was introduced in 1987 and was quickly accepted in clinical medicine and research (Jergas and Genant, 1993). It operates by placing the subject on a flat bed and scanning the whole body or parts of it by two different X-ray frequencies which have different attenuation properties in bone and soft tissue[1]. At high frequencies, attenuation parameters are similar, but at low frequencies, a good contrast between tissue types is achieved (Blake and Fogelman, 1997). Thus, in combination, the techniques can determine the tissue type at a given location of the X-ray shadowgram, in addition to the total absorption coefficient.

When used in whole body scans, DXA can monitor various body composition parameters such as the body fat percentage, but it is mainly used to determine BMD and BMC. Typical sites for a BMD measurement are the hip and lumbar spine, composed mostly of cancellous bone, where the effects of osteoporosis can be readily seen. Also preripheral sites such as calcaneus and wrist are used (*i.e.* central DXA).

[1] In this context, soft tissue basically means everything else than bone. Elsewhere in this Thesis, soft tissue is used as a shorthand for the fat and muscle tissue surrounding long bones. Note however that since fat, muscle and other tissues have somewhat different attenuation properties, DXA can also measure muscle and fat mass.

DXA is today's clinical standard for diagnosing a reduced bone mass related to osteoporosis, largely because the WHO definition is based on measurements by that device. DXA is used for osteoporosis diagnosis, fracture risk assessment and monitoring response to treatment (Blake and Fogelman, 2009). Its advantage is that, using DXA, it is possible to measure the sites which are most susceptible to fractures (hip) and which have good response to treatment (spine) (Blake and Fogelman, 2009). Radiation dose from DXA is also low compared to other radiological investigations (from various sources, 0.1–0.37 μSv for a total body scan and 1.6–5 μSv for spine or hip scans (Albanese, 2003; Blake et al., 2006; Griffith and Genant, 2008)), so there need not be as high reservations on its use, and for example operator qualifications are less strictly regulated than for other radiological investigations.

However, DXA measurements have their limitations. As the measurement results are 2D projections of a 3D object, they are strongly correlated with the size and amount of bone, and densities are largely indistinguishable by this measurement method. 2D projection also hampers the reliability of the measurement of obese patients (Knapp et al., 2012). Because of its low resolution, DXA cannot be used to separate cortical and trabecular bone, or to observe bone geometry or architecture such as trabecular size, shape, orientation or the geometry of cortical cross section (Beck, 2003; Griffith and Genant, 2008). In addition, even though BMD is one of the best predictors of bone strength, it cannot comprehensively predict fractures by itself (Bolotin and Sievänen, 2001; Griffith and Genant, 2008; Hooven et al., 2009; Stone et al., 2003). Moreover, for an effective prevention of osteoporosis, the population base should be screened for the disease before fractures happen. As DXA is expensive enough to be typically only available in hospitals (*i.e.* the cost of GE Lunar devices is of the order of 20000€), and because it uses ionizing radiation, it is poorly suited for screening purposes. As such, osteoporosis remains a largely under-diagnosed disease (Kannus et al., 2006).

2.5.2 (Peripheral) Quantitative computed tomography (QCT and pQCT)

Quantitative computed tomography was invented in London and at the University of California in San Francisco during the 1970's, and has since been widely accepted as an imaging tool in many fields. In this technique, an object is imaged with X-rays from multiple angles around a single rotational axis (typically equally distributed along a circle or a half circle) and a large number of two-dimensional X-ray shadowgrams is obtained. A two or three dimensional image is then reconstructed using the Algebraic reconstruction technique, based on the work of Johann Radon and Stefan Kaczmarz (Radon, 1917; Kaczmarz, 1937). Technically the imaging method does not have to consist of X-rays, and multiple alternatives do exist for various applications, if the object is transparent for other wavelengths. However, for clinical applications in humans, X-rays are essential.

As the technique produces real slices of the object under investigation, it can be used to assess the size and geometry of bone, and the true volumetric BMD instead of the 2D approximation provided by DXA. Because of this, QCT is con-

sidered to be more sensitive to BMD variations than DXA (Griffith and Genant, 2008). QCT devices are typically used to measure the trabecular areas in spine and hip locations. Average bone mineral density from these locations is compared to age and sex matched controls. Unlike DXA, T-scores are not used and volumetric BMD is directly compared to reference values. American College on Radiology guidelines (American College of Radiology, 2008) state a BMD value of less than 80 mg/cm^3 to be osteoporotic and less than 120 mg/cm^3 to be osteopenic. Higher values are considered normal. The disadvantage of using QCT in the same sites as DXA is, that taking tomography images of spine and hip involves a radiation load significantly higher than DXA (up to 3 mSv in the hip (Damilakis et al., 2010)).

Peripheral QCT devices are aimed at appendicular bone sites such as distal radius and tibia. The advantage of this is that devices are cheaper and that radiation dose is both smaller (less than 10 μSv, even for high resolution scans (Damilakis et al., 2010)) and not aimed at regions which contain sensitive internal organs. Higher resolution pQCT devices are capable of a 80–90 μm^3 voxel size, which is sufficient to see individual trabeculae and their connectivity (Damilakis et al., 2010; Griffith and Genant, 2012). At lower resolutions and doses, it is still possible to separate trabecular and cortical bone and measure bone geometry parameters such as CSMI, CSA, SSI and cortical thickness.

3 QUANTITATIVE ULTRASOUND

The word *ultrasound* is defined as mechanical vibration (sound), with a frequency which is too high to be detected by human ears. In practice, this means frequencies greater than $20kHz$. In this Section, we outline the basic properties of ultrasound and discuss its use in skeletal quantitative ultrasound (QUS) in the context of characterizing osteoporosis. In particular, the status of background research is outlined, so as to give motivation for the present Thesis.

3.1 The basic physics of ultrasound

When considered to propagate in an infinite isotropic medium, ultrasound does not differ from any other sound vibration. A simple analogy for sound vibration is to think of a dense matrix of particless connected by massless strings. When a particle is disturbed, a force acts on its neighbours through its string connections and allows the disturbance to propagate. In a solid medium, two basic types of vibration can be detected, depending on whether particle oscillation occurs in the direction of wavefront propagation (longitudinal or compression waves) or perpendicular to it (transverse or shear waves). Longitudinal waves simply represent a pressure wave inside an elastic material, while shear waves are displacements of particles caused by neighboring particles dragging them in a transverse direction. Because shear waves rely on shear forces between adjacent particles to propagate, they cannot be detected in materials without rigid connections between particles (e.g. in ideal fluids). In these cases, only the longitudinal waves can effectively propagate. Depending on viscosity, shear waves may still be present in fluids, but they typically attenuate very quickly. This is also the case for the human soft tissue. As such, medical ultrasound imaging focuses on the use of longitudinal waves, their doppler shifts and reflections.

Velocity of the both longitudinal and transverse waves are, in the ideal case, independent of frequency. Their velocities are given by

$$c_L = \sqrt{\frac{E(1-\nu)}{\rho(1+\nu)(1-2\nu)}} \tag{2}$$

and

$$c_T = \sqrt{\frac{E}{2\rho(1+\nu)}}, \tag{3}$$

where E is Young's modulus, ν is Poisson's ratio and ρ is material density.

In practice almost everything, including factors not directly related to material properties such as pressure and temperature, affect wave propagation velocities. As ultrasound obeys basic wave dynamics, acoustic impedance (Z), a quantity analoguous to the refractive index in optics, can be defined for each material by

$$Z = \rho c, \tag{4}$$

where ρ and c are the density of and speed of sound in, respectively, the material in question. As with optics, acoustic impedance affects the intensity of transmitted and reflected waves at the interfaces of the material. Reflection and transmission coefficients are defined as

$$R = \frac{I_r}{I_i} = \left(\frac{Z_2 cos\theta_1 - Z_1 cos\theta_2}{Z_2 cos\theta_1 + Z_1 cos\theta_2}\right)^2 \tag{5}$$

and

$$T = \frac{I_t}{I_i} = \frac{4Z_1 Z_2 cos\theta_1 cos\theta_2}{(Z_2 cos\theta_1 - Z_1 cos\theta_2)^2}, \tag{6}$$

where I_i, I_r and I_t are the incident, reflected and refracted (transmitted) wave intensities, Z_1 and Z_2 are acoustic impedances on both sides of the interface and θ_1 and θ_2 are the angles of incidence or refraction, respectively. Angles θ_1 and θ_2 can also be determined from Snell's law,

$$\frac{sin\theta_1}{c_1} = \frac{sin\theta_2}{c_2}, \tag{7}$$

where c_1 and c_2 are the speeds of sound on the two sides of the interface. Note that in fluid-solid interfaces, when the transmission and reflection are not normal to the surface, these cases are more complex. The two materials cannot necessarily support the same forces, and shear stresses do not necessarily propagate through the interface.

Of the factors causing ultrasound attenuation, the most important are direct absorption of vibration energy by transformation to heat and scattering. In scattering, the principal mechanism is scattering of the wave, when it encounters particles made of some other material, or cracks or pores in the medium. These features act as interfaces, causing reflections and transmissions, and thereby alter the propagation direction (and speed) of the wavefront. In practice, scattering is a numerically and analytically hard problem, with only few easy solutions for very specific geometries. It is typically only treated as a numerical or measurement feature, and can be approximated, along with other attenuation properties, by

$$I = I_0 e^{-2\alpha(f)x}, \tag{8}$$

where I is the final and I_0 the initial intensity, and $\alpha(f)$ the (typically measured) pressure attenuation coefficient as a function of frequency. Fast amplitude changes are related to large displacements of particles inside the medium and large energy losses. High frequencies are thus more heavily dissipated in a medium. Factor 2 in the exponent results from the fact that intensity depicts energy which is related to the second power of the pressure amplitude of a plane wave. (Rose, 1999; Royer and Dieulesaint, 2000)

3.2 Ultrasonic guided waves

Unlike soft tissue, bone is a rigid material, wherein both longitudinal and transverse waves can be observed. Furthermore, the analogue between ultrasound waves and electromagnetic waves does not stop at basic reflections and refractions. Rigid materials can act as waveguides for sound waves, just as hollow metal tubes are waveguides for microwaves and optical fibers for visible light. Similarly to electromacnetic waveguides which utilize the refraction or conductivity properties of the waveguide, which are different from those of its inner material, so as to become constantly reflected and thus kept inside the waveguide, dense objects inside a sparse medium act as waveguides for sound waves. If the impedance difference at the interface is large, sound wave will experience a total reflection and remain inside the waveguide. Thus, in addition to longitudinal and shear waves, solid materials support the propagation of guided waves (GW), which arise from refractions, reflections and mode conversions of longitudinal and shear waves at the boundaries of the medium.

The problem of guided wave propagation has been studied extensively because of its relevance in material technology and seismology. There are many types of guided waves propagating in various geometries, such as Lamb, Love, Rayleigh and Stoneley waves (Lamb, 1917; Love, 1911; Rayleigh, 1885; Stoneley, 1924) (fig. 5). Of these, Lamb waves are most interesting for our purposes, since they are solutions to waves propagating in infinite solid plates of given thickness placed in vacuum (Viktorov, 1967). In addition to being useful for approximating

the behaviour of ultrasound propagation in many solids and subsequently being useful in the fields of construction and material testing, this solution (Lamb waves) can be adapted to multi-layered and tubular structures including bone walls (Gazis, 1958; Graff, 1991; Pavlakovic, 1998). In a typical measurement situation, the assumptions of the theory are less restrictive than is immediately evident, as air imitates vacuum rather well because of the big difference between its acoustic impedance and those of most solid materials.

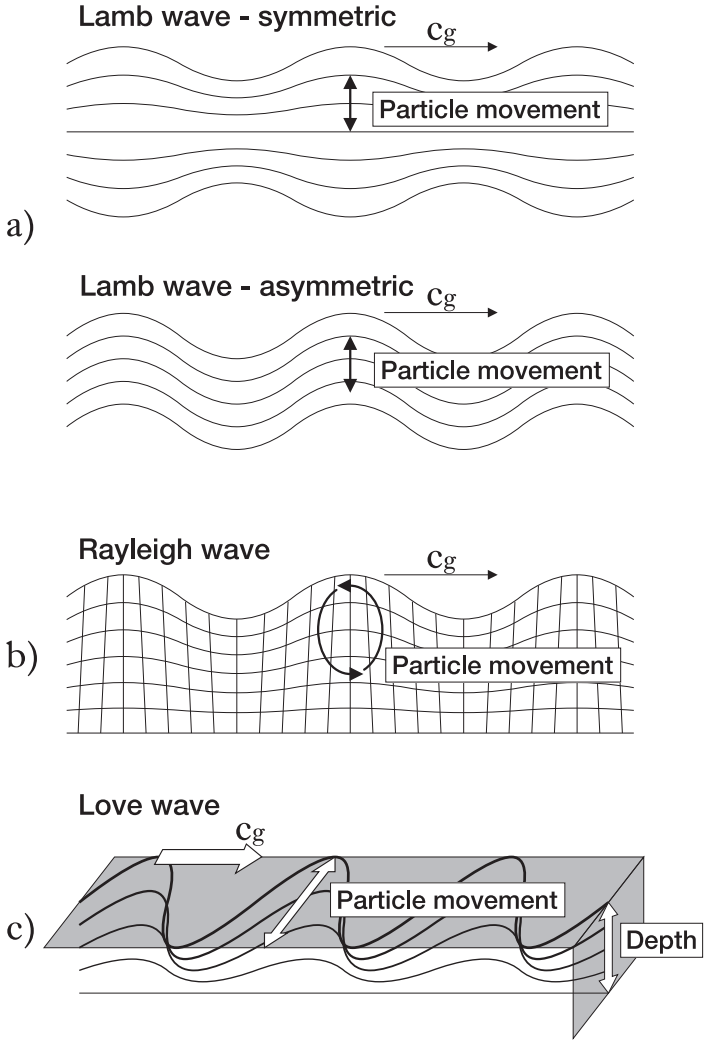

FIGURE 5 Main types of guided waves and related deformation shapes in solid structures. Depicted are (a) Lamb, (b) Rayleigh and (c) Love waves.

3.2.1 Lamb waves in free plates

The basis behind the formation of Lamb waves is that partial compression and shear waves form resonant standing waves at oblique angles between the boundaries of a plate. Because of these oblique angles, the standing waves are reflected with respect to the normal of the surface, and propagate along the plate. Finally, Lamb modes (wavenumber k) are born as a superposition of these compression

(k_L) and shear (k_T) standing wave components (fig. 6).Phase velocities (c_{ph}) and frequencies (f) of the partial waves must match based on the above principle and relation $c_{ph} = 2\pi f/k$. Thereby, at a certain frequency and thickness, only certain modes can exist. (Rose, 1999)

In a free plate, Lamb waves can thus be modelled using four partial waves, downward and upward propagating longitudinal and shear waves (fig. 6).

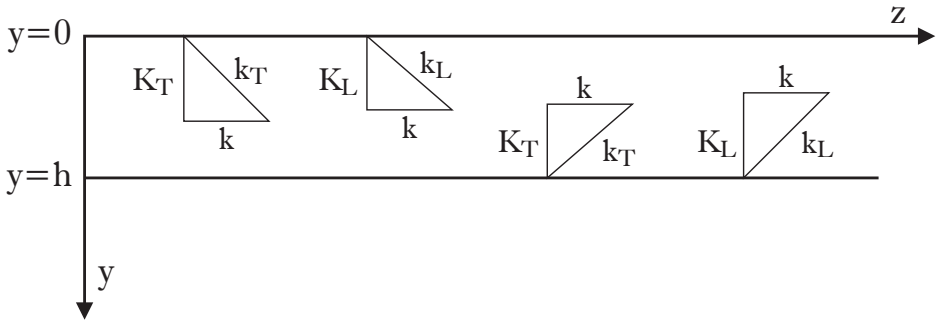

FIGURE 6 Schematic illustration of the free plate problem. $k_{L,T}$s are wave numbers of longitudinal and shear partial waves, $K_{L,T}$s are the normal components of the wave numbers of the partial waves and k is the (tangential) component of the wave number of the guided wave. Plate thickness is represented by h.

Navier's equation of motion for displacements,

$$(\lambda + \mu)u_{j,ij} + \mu u_{i,jj} = \rho \ddot{u}_i, \tag{9}$$

can model the motion of a linear, elastic solid. Herein u_i is the displacement vector, ρ is the mass density and λ and μ are the Lamé constants,

$$\begin{aligned} \lambda &= \frac{\nu E}{(1+\nu)(1-2\nu)} \\ \mu &= \frac{E}{2(1+\nu)}, \end{aligned} \tag{10}$$

or alternatively

$$\begin{aligned} \lambda &= \rho(c_L^2 - 2c_T^2) \\ \mu &= \rho c_T^2. \end{aligned} \tag{11}$$

Notation $u_{k,ij}$ stands for the partial derivative

$$u_{k,ij} = \frac{\partial^2}{\partial x_i \partial x_j} u_k. \tag{12}$$

Displacement vector can be expressed with the help of Helmholtz decomposition such that

$$u_i = \frac{\partial \phi}{\partial x_i} + e_{ijk}\frac{\partial \Psi_k}{\partial x_j}, \tag{13}$$

where ϕ and Ψ_j are scalar and vector potentials, respectively, e_{ijk} is the permutation symbol (-1 if the order of ijk represents an odd number of swaps away from the original lexicographic order, and +1 if that number is even). If eq. (13) is substituted into eq. (9), we get two uncoupled equations,

$$\left(\nabla^2 - \frac{1}{c_L^2}\frac{\partial^2}{\partial t^2}\right)\phi = 0 \text{ and} \tag{14}$$

$$\left(\nabla^2 - \frac{1}{c_T^2}\frac{\partial^2}{\partial t^2}\right)\Psi = 0, \tag{15}$$

where ∇ is the del operator, *i.e.* $\nabla^2 = \partial^2/\partial y^2 + \partial^2/\partial z^2$. As previously, c_L and c_T are the longitudinal and shear wave velocities, respectively. Using the partial wave formalism, solutions to eqs. (14) and (15) are of the form

$$\begin{aligned}\phi &= C_1 e^{ik_L(zsin(\theta_L)+ycos(\theta_L))} + C_2 e^{ik_L(zsin(\theta_L)-ycos(\theta_L))} \\ \Psi &= C_3 e^{ik_T(zsin(\theta_T)+ycos(\theta_T))} + C_4 e^{ik_T(zsin(\theta_T)-ycos(\theta_T))},\end{aligned} \tag{16}$$

where C_i are unknown constants determined by the boundary conditions of the problem, k_L and k_T are wavenumbers of the bulk and shear wave components, k that of the guided wave (fig. 6), and θ_L and θ_K are the angles between the vertical and bulk wavenumbers in fig. 6, obtainable from $\theta_L = arcsin(k/k_L)$ and $\theta_K = arcsin(k/k_K)$.

Potentials in eq. (16) have four terms, representing two longitudinal bulk plane waves and two bulk shear waves in the vertical direction ($K_{L,T}$ in fig. 6). Terms with a negative sign are downwards propagating waves and those with a postive sign are upwards propagating waves.

Substituting eq. (16) into eq. (13), displacements can be solved directly. Strains (ϵ_{ij}) are given by

$$\epsilon_{ij} = \frac{1}{2}\left(\frac{\partial u_i}{\partial x_j} + \frac{\partial u_j}{\partial x_i}\right) \tag{17}$$

and stresses (σ_{ij}) are given by

$$\sigma_{ij} = \lambda \delta_{ij}\epsilon_0 + 2\mu\epsilon_{ij}, \tag{18}$$

where δ_{ij} is the Kronecker delta and dilation is $\epsilon_0 = \epsilon_{11} + \epsilon_{22} + \epsilon_{33}$.

If the plate is in vacuum, traction and pressure are assumed to be zero in the upper and lower free surfaces, $y = h$ and $y = 0$. Thus, there are no forces acting at the surface either in the normal or transverse direction, and stresses are given by $\sigma_{yy} = \sigma_{yz} \equiv 0$. If horizontal shear displacements are ignored ($u_x \equiv 0$), using each of these boundary conditions in eq. (17) and eq. (18) we get four equations,

$$(\lambda k_L^2 + 2\mu K_L^2)(C_1 + C_2) + 2\mu k K_T (C_3 - C_4) = 0 \tag{19}$$

$$-2\mu k K_L (C_1 - C_2) + \mu (K_T^2 - 2k_T^2)(C_3 + C_4) = 0 \tag{20}$$

$$(\lambda k_L^2 + 2\mu K_L^2)(C_1 e^{iK_L h} + C_2 e^{-iK_L h}) + 2\mu k K_T (C_3 e^{iK_T h} - C_4 e^{-iK_T h}) = 0 \tag{21}$$

$$-2\mu k K_L (C_1 e^{iK_L h} - C_2 e^{-iK_L h}) + \mu (K_T^2 - 2k_T^2)(C_3 e^{iK_T h} + C_4 e^{-iK_T h}) = 0, \tag{22}$$

where

$$K_{L,T} \equiv k_{L,T} cos(\theta_{L,T}) = \sqrt{k_{L,T}^2 - k^2} = \sqrt{\left(\frac{\omega}{c_{L,T}}\right)^2 - k^2}, \tag{23}$$

and ω is the angular frequency.

Using a matrix notation and C_1–C_4 as a column vector $\mathbf{C}$, eq. (19)–eq. (22) can be expressed in a matrix form such that

$$[G]\mathbf{C} = 0, \tag{24}$$

where $[G]$ is a matrix of the form

$$\begin{bmatrix} \lambda k_L^2 + 2\mu K_L^2 & \lambda k_L^2 + 2\mu K_L^2 & 2\mu k K_T & -2\mu k K_T \\ -2\mu k K_L & 2\mu k K_L & \mu (K_T^2 - 2k_T^2) & \mu (K_T^2 - 2k_T^2) \\ (\lambda k_L^2 + 2\mu K_L^2) e^{iK_L h} & (\lambda k_L^2 + 2\mu K_L^2) e^{-iK_L h} & 2\mu k K_T e^{iK_T h} & -2\mu k K_T e^{-iK_T h} \\ -2\mu k K_L e^{iK_L h} & 2\mu k K_L e^{-iK_L h} & \mu (K_T^2 - 2k_T^2) e^{iK_T h} & \mu (K_T^2 - 2k_T^2) e^{-iK_T h} \end{bmatrix}.$$

Equation (24) is satisfied when the determinant of $[G]$ is zero. Thus, the characteristic equation for a plate in vacuum can be expressed in the form

$$det(G(\omega, k, c_L, c_T, h)) = 0, \tag{25}$$

Solutions to eq. (25) give the dispersion relations of the Lamb wave modes for an infinite plate of given thickness in vacuum. Roots can be solved numerically (Lowe, 1995; Pavlakovic, 1998; Rose, 1999). Choice of variables relies here on using wave speeds $c_{L,T}$ in the derivation of wavenumbers $k_{L,T}$ and from the fact that $K_{L,T}$s are functions of $c_{L,T}$, ω and k. This formulation of the problem only requires textbook values and geometric variables for the material in question.

In the typical case, this equation has multiple solutions for any given ω and k, and following the trajectories of the solutions through the space of their parameters forms the characteristic curves of the guided Lamb wave modes (often

called dispersion curves, as eq. (25) is a dispersion equation). Typically solutions are studied in the wave number – angular frequency space. It is also common to use transformations $f = \frac{\omega}{2\pi}$ and $c = \frac{\omega}{k}$ to study them in either wave number – frequency or phase/group velocity – frequency space (see fig. 8). As the thickness parameter only affects the wavelengths required for standing waves, it only affects the scale of frequency axis in the chosen representation. For this reason, it is common for more generalized dispersion curve diagrams to either use the frequency $\times$ thickness -axis, or, expressed in another form, the plate thickness / wavelength -axis.

In addition to representing the characteristic equation of Lamb waves by a matrix determinant (eq. (25)), also a classical analytical solution for the characteristic equation exists (Lamb, 1917; Viktorov, 1967). The classical solution is much more compact, but the advantage of the matrix solution is that it can be extended more easily to describe multi-layer (2D) and tube (3D) structures, and can conveniently be solved numerically.

In order to obtain the classical solution, solution to eqs. (14) and (15) is attempted in the form (Graff, 1991)

$$\phi = f(y)e^{i(kz-\omega t)} \tag{26}$$
$$\Psi = ih(y)e^{i(kz-\omega t)}, \tag{27}$$

where

$$f(y) = C_1 sin(K_L y) + C_2 cos(K_L y) \tag{28}$$
$$g(y) = C_3 sin(K_T y) + C_4 cos(K_T y). \tag{29}$$

In this representation, f and g are standing waves through the thickness of the plate and the periodic exponential term is a guided wave propagating along the z (horizontal) axis of the plate. Displacements, stresses and strains are the same as in eqs. (12), (17) and (18). The y axis is shifted slightly to simplify the computations, and the boundary conditions, $\sigma_{yy} = \sigma_{yz} \equiv 0$, are imposed at $y \pm h/2$. In this way we find the the Rayleigh-Lamb frequency equation in a more recognizable form,

$$\frac{tan(2K_T h)}{tan(2K_L h)} + \left(\frac{4K_L K_T k^2}{(k^2 - K_T^2)^2} \right)^{\pm 1} = 0, \tag{30}$$

where $K_{L,T}$s are the same as in eq. (23). Exponent ± 1 divides this equation into two separate equations, one of which $(+1)$ corresponds to axially symmetric and the other (-1) to antisymmetric modes. In practice interpretation of these modes will depend on whether the displacement at two opposite edges of the plate are directed in the same or opposite direction from their equilibrium positions (fig. 5a).

When investigating the actual results obtained (fig. 8), it should be noted that symmetric and antisymmetric modes alternate at any given frequency, and that not all Lamb wave modes are present in all frequency-thickness regions of the spaces portrayed. However, A_0 and S_0 span the whole space, which means that they should always propagate, without respect to the geometry of the plate and frequency used, albeit at speeds which are functions of thickness and frequency. At high frequency-thickness to wavelength ratios, their velocities converge towards the Rayleigh wave velocity (Viktorov, 1967), which is expected, as Rayleigh waves are surface waves propagating in semi-infinite solids, comparable to plates of infinite thickness.

3.2.2 Lamb waves in fluid-coated plates

In most situatios resembling real world geometries and materials excluding phantom measurements, the free plate case is insufficient. An important facet used in this work are cases of fluid-solid bilayers, which resemble situations with layer of soft tissue on top of the bone. The waves escaping to the fluid through the fluid-solid boundary are reflected and refracted from the fluid-vacuum (or air) boundary, and form a guided wave system in both materials. This causes strong coupling in the propagation of waves within the two subsystems, and as the material properties of fluids and solids differ greatly, also affects the dispersion characteristics of the modes in comparison with those which propagate in the solid alone. This situation has been discussed in detail in (Yapura and Kinra, 1995), but the solution strategy using the partial wave formalism from Rose (1999) is defined in fig. 7.

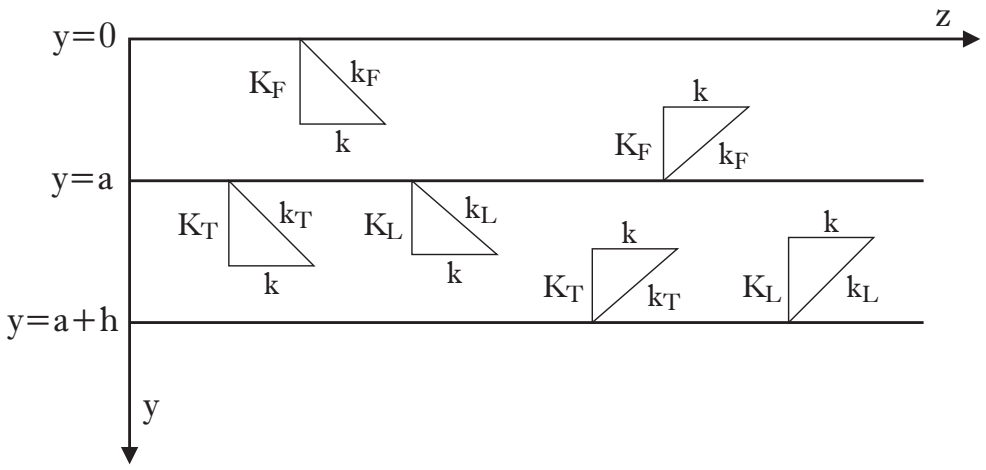

FIGURE 7 Schematic illustration of the fluid-solid bilayer problem. $k_{L,T,F}$s are wave numbers of tangential and shear partial waves in the plate and of the tangential wave in the fluid. $K_{L,T,F}$s are the normal wave numbers of the partial waves and k is the (tangential) wave number of the guided wave. Plate thickness is represented by h and fluid layer thickness by a.

In this solution, the fluid is considered ideal, i.e. unable to support shear

stresses. This increases the number of partial waves present to six. The wave equation for the fluid is given by

$$\left(\nabla^2 - \frac{1}{c_F^2}\frac{\partial^2}{\partial t^2}\right)\phi_F = 0, \tag{31}$$

where ϕ_F is the scalar potential and $c_F = \lambda_F/\rho_F$ is the bulk velocity of longitudinal wave in the fluid. λ_F and ρ_F are the bulk modulus and mass density of the fluid, respectively. Analoguous to eq. (16), solution to this is given by

$$\phi_F = C_1 e^{ik_F(zsin(\theta_F)+ycos(\theta_F))} + C_2 e^{ik_F(zsin(\theta_F)-ycos(\theta_F))} \tag{32}$$

with the longitudinal wave variables swapped (see eq. (16)) with those of the partial waves of the fluid. While $\Psi_F = 0$, displacements u_{iF}, stresses σ_{ijF} and strains ϵ_{ijF} are analogous to those of eqs. (13), (17) and (18).

There are six boundary conditions in this case. As the fluid carries no shear stress, it must be zero at the boundary between the two media, and on the bottom surface of the plate. Stresses normal to the bilayer structure must also be zero at the outer surfaces. However, stresses and displacements normal to the material surfaces must match at the interface,

$$\begin{aligned}
\sigma_{yyF}\big|_{y=0} &= 0 \\
u_{yF}\big|_{y=a} &= u_y\big|_{y=a} \\
\sigma_{yyF}\big|_{y=a} &= \sigma_{yy}\big|_{y=a} \\
\sigma_{yz}\big|_{y=a} &= 0 \\
\sigma_{yy}\big|_{y=a+h} &= 0 \\
\sigma_{yz}\big|_{y=a+h} &= 0
\end{aligned} \tag{33}$$

Similarly to eq. (24), substituting these into eqs. (17) and (18), and transforming to a matrix form, we find that

$$[G]\mathbf{C} = 0, \tag{34}$$

where $[G]$ is a global matrix, and $\mathbf{C}$ is a column vector of six unknowns C_i, $i = 1, \ldots, 6$. This equation is satisfied when the determinant is zero. The $[G]$ matrix is a 6x6 matrix of the form

$$
\begin{array}{ccc}
G_{11} = -\lambda_F k_F^2 & G_{31} = \lambda_F k_F^2 e^{iK_F a} & G_{51} = 0 \\
G_{12} = -\lambda_F k_F^2 & G_{32} = \lambda_F k_F^2 e^{-iK_F a} & G_{52} = 0 \\
G_{13} = 0 & G_{33} = -(\lambda k_L^2 + 2\mu K_L^2) e^{iK_L a} & G_{53} = (\lambda k_L^2 + 2\mu K_L^2) e^{iK_L (a+h)} \\
G_{14} = 0 & G_{34} = -(\lambda k_L^2 + 2\mu K_L^2) e^{-iK_L a} & G_{54} = (\lambda k_L^2 + 2\mu K_L^2) e^{-iK_L (a+h)} \\
G_{15} = 0 & G_{35} = -2\mu k K_T e^{iK_T a} & G_{55} = 2\mu k K_T e^{iK_T (a+h)} \\
G_{16} = 0 & G_{36} = 2\mu k K_T e^{-iK_T a} & G_{56} = -2\mu k K_T e^{-iK_T (a+h)} \\
G_{21} = K_F e^{iK_F a} & G_{41} = 0 & G_{61} = 0 \\
G_{22} = -K_F e^{-iK_F a} & G_{42} = 0 & G_{62} = 0 \\
G_{23} = -K_L e^{iK_L a} & G_{43} = -2\mu k K_L e^{iK_L a} & G_{63} = 2\mu k K_L e^{iK_L (a+h)} \\
G_{24} = K_L e^{-iK_L a} & G_{44} = 2\mu k K_L e^{-iK_L a} & G_{64} = -2\mu k K_L e^{-iK_L (a+h)} \\
G_{25} = -k e^{iK_T a} & G_{45} = \mu (K_T^2 - k^2) e^{iK_T a} & G_{65} = -\mu (K_T^2 - k^2) e^{iK_T (a+h)} \\
G_{26} = -k e^{-iK_T a} & G_{46} = \mu (K_T^2 - k^2) e^{-iK_T a} & G_{66} = -\mu (K_T^2 - k^2) e^{-iK_T (a+h)}
\end{array}
, \tag{35}
$$

where K_F is analogous to eq. (23) and the other terms are equivalent to their definitions in section 3.2.1. Thus, dispersion equation for a fluid-solid bilayer can be expressed in the form

$$det(G(\omega, k, c_F, c_L, c_T, a, h, \rho_F, \rho)) = 0. \tag{36}$$

Choice of variables in eq. (36) relies on using $c_{F,L,T}$ instead of $k_{F,L,T}$, $K_{F,L,T}$ being a function of ω, $c_{F,L,T}$, k, and the Lamé constants and bulk modulus of the fluid being functions of wave propagation speeds and densities (ρ and ρ_F , see eq. (10)). Other choices are possible, but these only rely on textbook data for the materials in question. The roots of this equation are best solved numerically, due to which the solutions are referred to as semianalytical models. Figure 8 shows an example of the dispersion curves of both fluid-solid bilayer and free plate Lamb wave modes in various spaces. Implementation of the numerical solution is from (Moilanen, 2004).

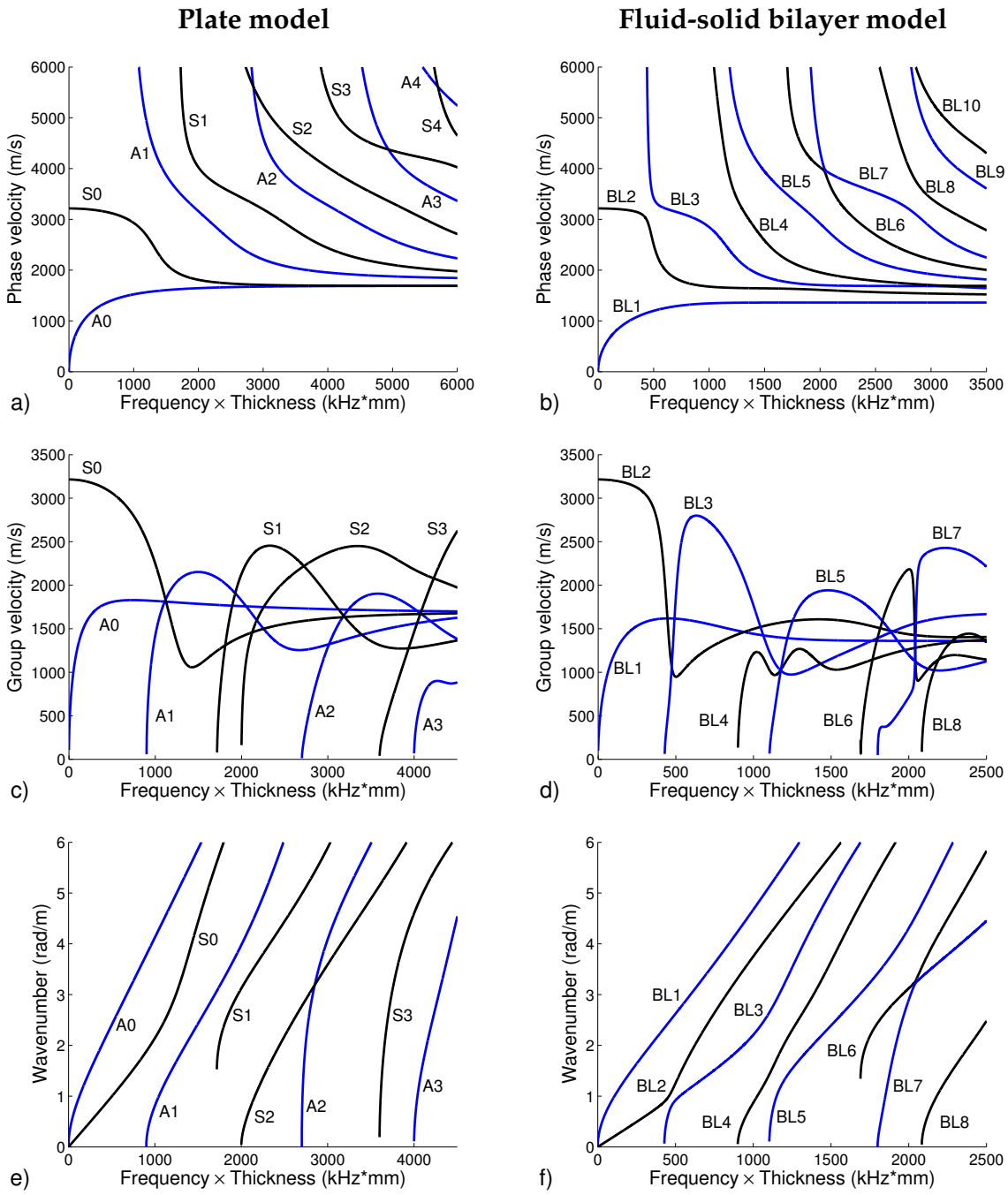

FIGURE 8 Dispersion curves of Lamb waves displayed in the phase velocity – frequency × thickness (a-b), group velocity – frequency × thickness (c-d) and wave number – frequency × thickness space (e-f). In this example, $c_F = 1481$ m/s, $c_L = 4000$ m/s, $c_T = 1800$ m/s, $\rho_F = 1$ g/cm^3, $\rho = 1.8$ g/cm^3 and thicknesses a and h were equal.

3.3 Methods of skeletal quantitative ultrasound

Ultrasound has been used in a medical context since 1937, when Karl Dussik developed a through-transmission technique usable for detecting brain tumors by

mapping attenuation variations in the brain tissue. While the most typical applications of ultrasound relate to soft tissue imaging, it has also been applied to bone characterization. Methods similar to Dussik's original one are still used in through-transmission measurements (section 3.3.1). Moreover, methods based on pulse-echo techniques (section 3.3.2) and axial transmission have been developed.

The main motivation in the use of QUS is its sensitivity to bone properties other than BMD, which is the main property assessed by the pQCT and DXA devices (Laugier, 2008). BMD is mostly associated with compressional strength, but also bending and torsional strength, determined by elastic moduli of the bone, are a factor in bone toughness (Peterlik et al., 2006; Turner, 2006; Glüer, 2008). QUS has the advantage of being sensitive to both cortical thickness and elastic moduli of the bone in addition to BMD (Moilanen et al., 2008).

3.3.1 Through-transmission

At the moment, the only QUS devices approved for clinical use are based on the through-transmission method, mainly applied to the heel bone (calcaneus). Since the introduction of QUS on heel in 1984 (Langton et al., 1984), many devices (Njeh et al., 2000; Kaufman et al., 2007) have reached the market, and are used to measure patients either in a gel-coupled through-transmission or water bath (fig. 9). Calcaneus is considered the most reliably reachable location because of a large semi-flat region of almost exclusively cancellous bone, which should both acccurately predict bone loss and be an easy location for a transducer (Black et al., 1992; Wasnich et al., 1987). It has also been shown to predict hip fractures as effectively as, but not consistently with DXA (Glüer, 1997).

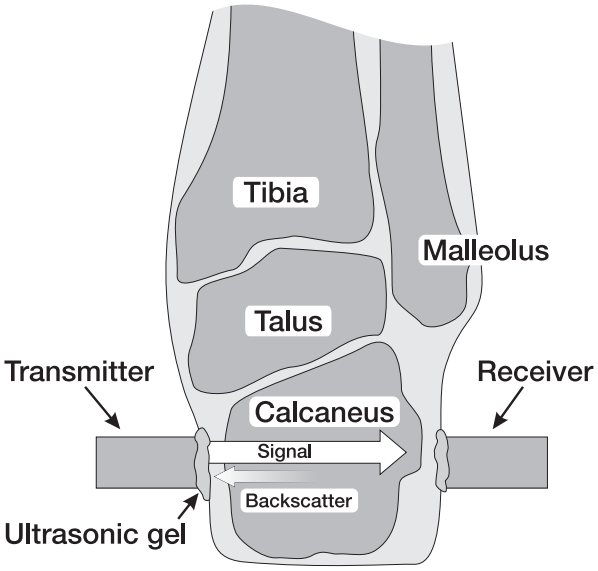

FIGURE 9 Principle of a QUS through-transmission measurement on heel.

Operation of these QUS devices is mostly based on either time of flight (ToF)

or broadband ultrasound attenuation (BUA). Speed of sound in bone tissue is higher than in water bath or soft tissue, so ToF directly tells about the absolute amount of bone. In addition, time differences between the arrival times of the first arriving signal and a more energetic guided wave component can be used to gauge the amount of bone. As the first arriving signal mostly travels in the cortical bone covering the bone site, and the through-transmission signal mostly travels through the cancellous part of the bone, a higher time lag between the pulses signifies a lower amount of cancellous bone. Alternatively, devices can track the time differences between propagation through the bone and soft tissue (Bréban et al., 2010; Evans and Tavakoli, 1990; Miller et al., 1993; Stein et al., 2013).

When measuring BUA, ultrasound pulses of varying frequency are transmitted through a cancellous bone specimen. Attenuation of the pulse has a complex relation with the amount and material properties of bone, as multiple effects simultaneously affect it (scattering, diffusion, absorption, transmission, reflection). While this means that the absolute amount of attenuation is not easily associated with any quantity, attenuation fortunately has the useful property of being linearly proportional to frequency in the 0.2–0.6 MHz range. Slope of the attenuation curve with respect to frequency is then a function of other bone properties, and has been shown to depend on BMC (Langton et al., 1984) and BMD (Chappard et al., 2012).

In addition to the QUS devices on heel, applications exists which use ultrasound transmission through finger phalanges (Reginster et al., 1998; Baroncelli et al., 2006) or the hip and proximal femur (Barkmann et al., 2007). The latter device is capable of measuring attenuation through the bone structure, reflections from the cortical surface and backscatter from the trabecular structure of the bone, and can use these data to form rudimentary images of the sites via scanning. Devices using through-transmission at the distal radius are also available (Bréban et al., 2010; Stein et al., 2013).

Despite the presence of various devices and the evidence supporting their effectiveness, heel QUS and quantitative ultrasound in general are not widely used in practice. At the time of its introduction, physics behind the relation of ultrasonic measurement parameters with bone fragility remained largely unknown, failing to provide an accurate bone assessment, and even for a specific region of calcaneus, QUS assessment was not well standardized. Different devices based on calcanean ultrasound measure either BUA, ToF, group or phase velocity or a synthetic benchmark of many of these quantities. Each use a varying frequency of their own, different frequency sweeps, or are immersed in water or are gel-coupled, and make different assumptions about the measurement situation or transducer location (static transducers or BUA map of calcaneus, measured heel width or assumed standard heel width) etc. (Glüer, 2008)

3.3.2 Pulse-echo ultrasound and ultrasonic backscatter

In the pulse-echo method, ultrasound is used in the same way as sonar locates submarines, icebergs and fish. A pulse is transmitted by a receiver and its echo is

read shortly thereafter, possibly by the same receiver. Devices track time of flight, attenuation and frequency properties of the pulse to obtain information about the structure being investigated. The most prominent application uses sound waves scattered from cancellous bone, using some of the same frequency dependent properties of the pulse as the through-transmission experiments.

Like BUA, also backscattering intensities depend on the frequency used, but more importantly, scattered wave intensity is heavily influenced by the geometry of the object it scatters from. For the purposes of the method, the relevant parts are the trabeculae themselves, which have a thickness of about 127 microns on average (Seghal and Greenleaf, 1984). This is much smaller than the wavelength of the pulse, and modelling and experiments suggest that in this scale, backscattering intensity should be proportional to the third power of the trabecular thickness (Wear and Laib, 2003). Experimental results have verified similar power laws (3.38 ± 0.31 @ 0.4–1.2 MHz, 3.1 ± 1.09 @ 0.4–1.2 MHz) (Chaffai et al., 2000; Padilla et al., 2006). Once the relation with respect to frequency is known, backscatter coefficient can be correlated with known bone properties, just like BUA, and correlations of the order of $r^2 = 0.66$ against BMD (Wear and Armstrong, 2000) and $r^2 = 0.76$ against the bone volume fraction (BMV) (Riekkinen et al., 2007) have been found *in vitro*. The clinical use of backscattering has been tested early by Laugier et al. (1997); Wear and Garra (1998), but so far there are no commercial devices relying on this technique.

Other applications attempt to use the simplest possible method and measure time between the echo from the periosteal (outer) and endosteal (inner) surface of cortical bone, coupled with an assumed speed of sound, to estimate cortical thickness (Karjalainen et al., 2008). The time of flight estimate is either formed directly from the waveform's estimated amplitude, or by the cepstrum method, in which a power spectrum is processed with an inverse Fourier transform and the resulting time domain signal is transformed to thickness data by $d = c\Delta t$, where c is the estimate for speed of sound and Δt is the frequency band of the harmonic oscillation. Though the ability of such a method to measure quantities other than cortical thickness is limited, correlations of up to $r = 0.98$ *in vitro* and $r = 0.95$ *in vivo* have been reported (Karjalainen et al., 2008). Certain applications use the pulse-echo measurement technique in combination with backscattering (Riekkinen et al., 2008).

3.3.3 Axial transmission

In the axial transmission (AT) method, propagation of ultrasonic waves is assessed along the axis of long bones (such as the radius or tibia). This method was first introduced in Siegel et al. (1958), where it was used to study fracture healing in long bones.

In an axial transmission setup, two ultrasound transducers are placed on the same side of the bone. One of the transducers acts as the transmitter and the other as a receiver. These transducers may move with respect to each other in order to record an ultrasound pulse at multiple source-receiver distances. Alternatively,

the transmitter or receiver can consist of an array of transducers (see section 5.1). Speed of sound is deduced from the difference in the time of flight that it takes from the signal to travel the distance between successive receivers or receiver separations (fig. 10). All known AT devices and AT measurement setups work on this same basic principle, but their implementations vary related to the number of transducers, frequency, criteria for determining the time of flight and the bone site used for the measurement (Barkmann et al., 2000; Bossy et al., 2004a; Lefebvre et al., 2002; Minonzio et al., 2010; Moilanen et al., 2003; Prevrhal et al., 2001; Ta et al., 2006), (I).

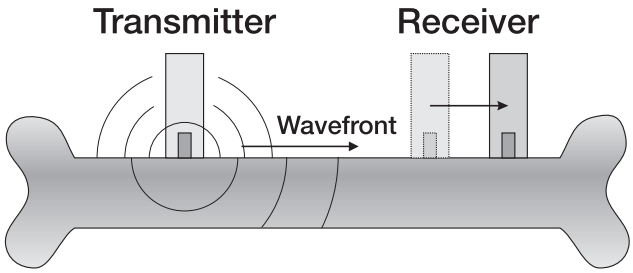

FIGURE 10 Principle of an axial transmission measurement. The flight time of an ultrasound pulse is recorded at various source-receiver distances to deduce the speed of sound in bone.

Typically axial transmission measurements are carried out on cortical bone shafts of human long bones, such as the radius and tibia, though smaller high frequency devices which support measurements on finger phalanges and metacarpal, capitate, patella, thoracic spine or calcaneus have also been used (Hans et al., 1999). Long bone shafts are ideal, because the geometry of a thin cortical layer and lack of subcortical, trabecular bone provide a plate like elastic waveguide for ultrasound. Radius and tibia also have a relatively thin layer of soft tissue embracing the bones. This is relevant, because too thick a layer of soft tissue would make it challenging to excite and detect ultrasound in bone (Camus et al., 2000; Moilanen et al., 2008).

An AT measurement can feature the assessment of a fast, first arriving signal (FAS) (see section 3.4.1), but it also allows for assessment of elastic guided waves, also known as Lamb waves (see sections 3.2.1 and 3.4).

Thus far three commercial devices based on AT have been introduced, all of which are based on a single US mode, the first arriving signal (section 3.4.1). SoundScan 2000 (Myriad Ultrasound Systems Ltd, Rehovot, Israel, now extinct) was the first device introduced in the 1990's. It operated at 250 kHz frequency and was designed to measure the tibia (Foldes et al., 1995). Later during the same decarde, Omnisense (BeamMed Ltd, Petah Tikva, Israel) was introduced (Hans et al., 1999; Barkmann et al., 2000). It operated at 1.25 MHz and featured some improvements with respect to SoundScan 2000 by correcting some influence of the coating of soft tissue. Omnisense is a multi-bone site ultrasonometer with a collection of probes dedicated to the radius, tibia and finger phalanges. Oscare Sono (OScare Medical Ltd, Helsinki, Finland) was introduced in 2013 and rep-

resents the latest development of commercial AT ultrasonometers. It operates at 250 kHz frequency and is based on an AT probe similar to the one reported in the present Thesis. In addition to these products, several experimental devices have been developed and tested. Currently research focus is on the development of multi-mode AT ultrasonometers based on Lamb modes (see section 3.4.2). Tatarinov et al. (2005); Tatarinov and Sarvazyan (2008) and Sarvazyan et al. (2009) were among the pioneers in using Lamb waves to detect bone properties, and their research, originating from the 1980's, has resulted in a dual-frequency AT ultrasonometer (100 and 500 kHz), also known as the Bone UltraSonic Scanner (BUSS, Artann Laboratories, Trenton, New Jersey, USA). This device is designed mainly for the tibia, but the exact operation principle behind it has not been divulged by the authors. The work of Minonzio et al. (2010) represents the latest development of multi-mode AT ultrasonometers, operating at 1 MHz centre frequency, and designed for the radius. Its clinical application is under development.

The present Thesis pursues the development of a multi-mode AT ultrasonometer that operates in a range of low US frequencies (20-400kHz).

3.4 Axial transmission and guided waves in bone

The shaft of cortical bone has been shown to support propagation of elastic guided waves consistent with Lamb wave modes (Lefebvre et al., 2002; Moilanen et al., 2007a; Ta et al., 2009). The advantage of guided waves is that they carry information about different aspects of bone quality (elastic properties, microporosity, bone mineral density, etc.) and geometry (cortical thickness), all of which are relevant in the characterization of bone fragility. Eventually, it should be possible to extract the impact of each independent bone property from measured velocities of guided waves. This requires solving of an inverse problem (Karim et al., 1990), bounded by parameters measurable from guided waves. To enable such an inversion, it is necessary to reduce the number of independent bone properties. It has recently been suggested that cortical bone can sufficiently be modelled by three independent parameters, mineral volume fraction, porosity and cortical thickness (Grimal et al., 2011). Other bone properties, such as e.g. coefficients of the three dimensional anisotropic elastic tensor can, with certain limitations, be derived from these parameters.

There is no consensus on the best suitable model for a theoretical prediction of guided waves in bone. The shaft of long bone is a solid tubular structure filled by a fluid like medium (fatty bone marrow) and embraced by another fluid like coating (soft tissue composed of fat and muscles). An exact model which would take the shape of the bone into account would require numerical simulation (Moilanen et al., 2007b,c) and would depend on information which is unattainable in the majority of clinical situations without use of more invasive methods (*i.e.* multiple pQCT scans of a limb). The most detailed purely analytical model features a solid anisotropic tube coated by a fluid layer and filled by

fluid, but in practical situations, it may be sufficient to use a more simple model, such as that for a coated empty tube (Moilanen et al., 2008), for a bilayer plate (Moilanen et al., 2006; Tran et al., 2013) or even for an uncoated plate (Lee et al., 2004; Chen et al., 2012), to predict the behaviour of Lamb modes in *in vivo* bone. Choice of the simplest suitable model depends on the significance of bone curvature (plate or tube) and significance of coupling between the layer subsystems (number of layers). Significance of curvature and coupling is determined by the absorption of ultrasound and the geometry (of bone and soft tissue), and details of the measurement setup (such as frequency). The present Thesis is limited to use of plate models (uncoated and bilayer).

3.4.1 First arriving signal (FAS)

FAS is an apparent (guided) mode which is observed as a transient in the time domain. This apparent mode can be interpreted as a superposition of Lamb modes (section 3.2.1) which are in the frequency range of an ultrasound measurement, but such an interpretation has not yet been used in the literature. Conventionally, FAS has been interpreted as a transition between lateral longitudinal wave and fundamental symmetric Lamb mode (S0) (Bossy et al., 2002). When the wavelength in the axial direction (λ) is short compared to cortical thickness, FAS propagates like it would in a semi-infinite solid, in which case its velocity is consistent with that of a lateral longitudinal wave (fig. 11). When λ is comparable or larger than the cortical thickness, velocity of FAS tends towards that of the S0 Lamb mode, eventually becoming consistent with it. More specifically, for an anisotropic (transversely isotropic) case, transition region occurs when the plate thickness is in the range from $\lambda/4$ to $\lambda/2$, and in an isotropic case this range is from $\lambda/8$ to λ (Bossy et al., 2002, 2004a). These predictions are consistent with experimental data (Nicholson et al., 2002; Prevrhal et al., 2001). FAS behavior with respect to cortical thickness has been explored in an *in vivo* study in I.

Velocity of FAS is thereby sensitive to thickness of the cortical wall, which explains part of its clinical potential in diagnosing osteoporosis. Fundamentally, FAS velocity is predicted however by a combination of elastic material properties and thickness. Raum et al. (2005) showed for *in vitro* radius specimens that 84% on the variability of the FAS velocity was predicted by a model composed of the acoustic impedance (represents an elastic coefficient C33), microporosity and cortical thickness. A number of *in vitro* (Muller et al., 2005) and *in vivo* studies (Prevrhal et al., 2001; Moilanen et al., 2003), (I) confirm that FAS velocity correlates with material properties (bone mineral density) and cortical thickness. Moreover, FAS velocity has been shown to be correlated with Young's (elastic) modulus (Lee et al., 1997; Muller et al., 2008).

Relative roles of bone properties in the multi-parametric models which predict the FAS velocity depend on the ratio of cortical thickness and wavelength. This ratio determines the sensitivity of velocity to cortical thickness, as expressed more specifically above. Moreover, wavelength determines the penetration depth of ultrasound into the bone (Bossy et al., 2004b). When the wavelength is suffi-

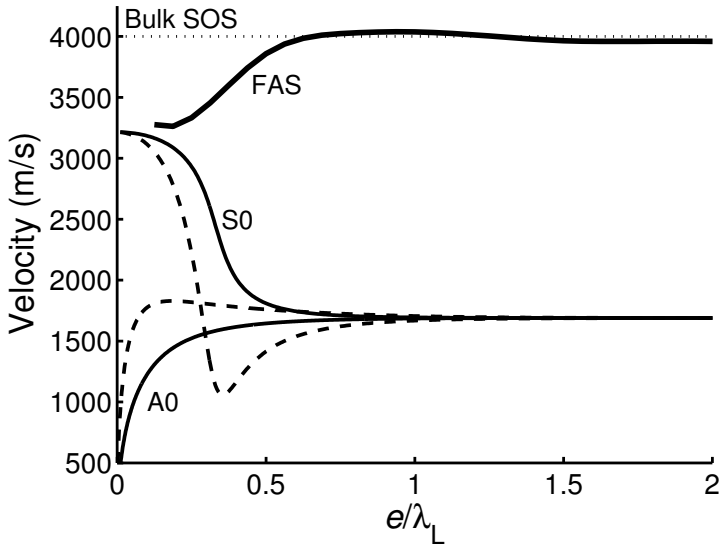

FIGURE 11 Apparent velocity of FAS as a function of the ratio of cortical wall thickness e to longitudinal wavelength λ_L (after Bossy et al. (2004b)). Phase velocities (thin solid curves) and group velocities (dashed curves) of S0 and A0 Lamb modes are shown for comparison. Moreover, compression bulk velocity is represented by dotted line.

ciently long for penetration through the entire cortical wall, FAS has an enhanced sensitivity to osteoporotic changes which primarily take place at or near the endosteal surface of the bone (Tatarinov et al., 2005; Haïat et al., 2009). For these reasons, use of low ultrasonic frequencies should enhance the sensitivity of FAS measurements in diagnosing osteoporosis.

A layer of soft tissue on top of the bone results in a significant bias in the time of flight of FAS, which must be corrected for a sufficient accuracy of the measured FAS velocity. As the fastest route for an ultrasound pulse requires travel through the soft tissue layer to the bone and back through it to the receiver, the determination of differences in the times of flight between successive receivers corrects for the presence of a soft tissue layer of uniform thickness; for each successive receiver, only the time spent travelling through bone will change. However, this approach presumes that there is no tapering in the soft tissue. To correct for the effect of soft tissue tapering, Bossy et al. (2004a) proposed a bidirectional technique (fig. 12). An ultrasound pulse is excited, sequentially, in two opposite directions, and the corrected apparent velocity c_{app} can be obtained as the harmonic mean of the unidirectional apparent (measured) velocities c_+ and c_-,

$$c_{app} = \frac{2}{\frac{1}{c_+} + \frac{1}{c_-}} cos\alpha, \tag{37}$$

where α is the angle of soft tissue tapering with respect to bone surface. Value of alpha is usually unknown, but if it is quite small, the corresponding term

can be neglected in the above equation ($cos(\alpha) \approx 1$) without causing a significant error. FAS velocity is called apparent to distinguish it from the phase and group velocity.

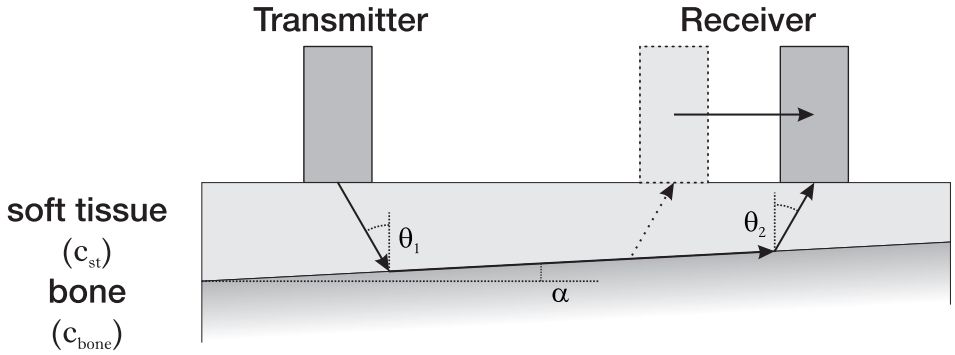

FIGURE 12 Axial transmission in the presence of soft tissue tapering. Shown is the case of a pulse propagating towards decreasing thickness of the soft tissue. The angle of tapering is denoted by α. θ is a function of the ratio of speeds of sound in soft tissue (c_{st}) and bone (c_{bone}).

3.4.2 Fundamental flexural guided wave (FFGW)

Fundamental flexural guided wave (FFGW), generally consistent with the A0 mode, has attracted interest in bone assessment because of its strong sensitivity to thickness (fig. 13). The phase velocity of this mode has shown to correlate well with cortical thickness, for instance, a study on *in vitro* samples of human radius has indicated that variability in the cortical thickness (pQCT) explaines at least 52% ($p < 0.001$) of the variability in the phase velocity of FFGW (Muller et al., 2005). The result in question was limited by correlation against average the cross-sectional cortical thickness at the measurement site, and comparisons against localized cortical thickness have later shown correlations higher than this (Moilanen et al., unpublished). In particular, it has been reported that it is possible to ultrasonically assess cortical thickness by fitting the measured phase velocity by a suitable theoretical model. For *in vitro* measurements on human radius, the ultrasonically determined cortical thickness has predicted 81% ($p < 0.001$) of the variability in localized cortical thickness (Moilanen et al., 2007a).

FFGW is, unlike FAS, associated with a single Lamb mode. This feature permits determination of the phase velocity of FFGW using two dimensional fast Fourier transform (2D-FFT) (Alleyne and Cawley, 1991; Moilanen et al., 2006). As mentioned above, there is no consensus on the simplest suitable model to predict FFGW experiments. Results for human radius (Moilanen et al., 2007a), and those for *in vivo* models mimicking the radius (Moilanen et al., 2008, 2014) suggest that curvature must be taken into account and that F(1,1) (fundamental flexural Lamb mode in tubular structures) is needed. Nevertheless, A0 or BL1 of the plate models have shown to be sufficient when analyzing FFGW measurements simulated in a two dimensional (2D) space. The present Thesis focuses on the 2D analysis

based on the A0 or BL1 prediction.

Presence of soft tissue embracing the bone has shown to be the main obstacle in the development of FFGW based assessment of cortical thickness *in vivo*. It can be predicted from displacement profiles of the BL1 mode (Yapura and Kinra, 1995) that FFGW has a small displacement amplitude in the fluid coating, while it features significant displacements inside the solid substrate (the bone). Moreover, it is predicted by Yapura and Kinra that the soft coating subsystem permits propagation of other modes which have significant displacements mainly in the coating. Such modes have shown to interfere with FFGW, and it has shown challenging to distinguish FFGW from this interference (Moilanen et al., 2008, 2014).

Our recent research has focused on developing solutions to the detectability problem of FFGW. Temporal gate windowing, called group velocity filtering (GF), has been proposed as a signal processing method to separate the region of the FFGW wave packet from interferences which arrive at different times of flight, determined by the group velocities characteristic of each mode. Although useful, this technique has shown to be insufficient to *in vivo* measurements because of overlapping times of flight. Tuning of the frequency of excitation and detection has shown to improve the signal to interference ratio (SIR, a power ratio between FFGW and interfering modes or noise[1]) of FFGW in coated bone phantoms. It has been shown that FFGW is optimally detected by tuning to low ultrasound frequencies (20-100 kHz) (Moilanen et al., 2014).

The present Thesis evaluates by numerical modelling further methods of improving the SIR of FFGW in coated bone.

3.4.3 Implementation of an array transducer

The earlier device used for AT QUS experiments in bone was composed of a fixed transmitter and a movable receiver (Moilanen et al., 2003). Mechanical scanning of the source-receiver distance by sequentially moving the receiver resulted in spatio-temporal signals for the assessment of FAS and FFGW. This device, although used in several *in vivo* (Nicholson et al., 2002; Moilanen et al., 2003; Määttä, 2009) and *in vitro* (Muller et al., 2005; Moilanen et al., 2007a; Muller et al., 2008) studies, and capable of producing accurate results in ideal conditions, was slow and bulky to operate, and exhibited significant limitations in the reproducibility and accuracy of *in vivo* measurements. The latter features appeared because it did not permit reproducible positioning, and soft tissue tapering was not sufficiently corrected in the FAS measurements.

To this end, the first half of the present Thesis focuses on developing and testing a new, custom made array transducer for rapid and reproducible *in vivo* measurements (I; II). The design goals of this transducer over the previous scan-

[1] The concept of SIR is common within communication technology, where it is used to express the ratio of average received modulated carrier power and the average received co-channel interference power (cross-talk). More generally, it is used to denote the ratio of the wanted signal level to the level of a disturbing signal, as measured under specified conditions. Herein the term is used in the latter context, i.e. to denote the level of the (wanted) FFGW signal to (unwanted) interfering modes.

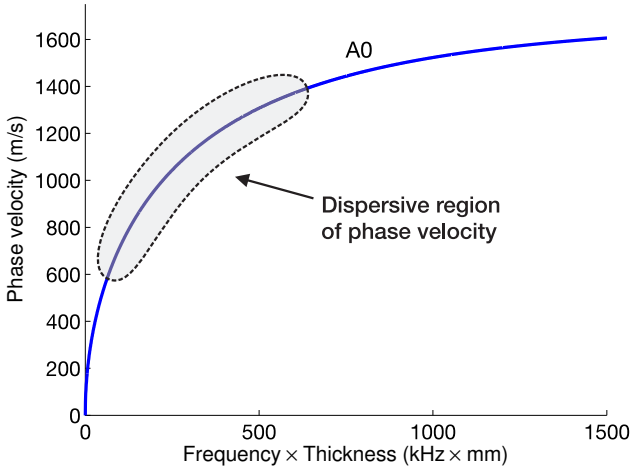

FIGURE 13 Dispersion curve of A0 for low values of frequency × thickness. As the phase and group velocity both tend towards zero, there is a region of substantial velocity dispersion, whose width depends on the phase velocity resolution of the measurement system.

ning ultrasound device were ease of use, especially in positioning, rapid measurements and a sufficient correction of soft tissue tapering.

This array transducer did not permit 2D-FFT analysis because of a coarse inter-element separation (6 mm) at the receiving array (see section 5.3.2 and fig. 22). To this end, alternative techniques were investigated to detect FFGW with the array transducer in III.

3.4.4 Phase-delayed excitation

While it is possible to improve the SIR ratio of FFGW by using low US frequencies (Moilanen et al., 2014), there are yet other options for a further SIR improvement.

A phase-delayed excitation has been reported to improve SIR in bone mimicking phantoms which have a soft tissue mimicking coating around a solid tube which represents the bone (Karppinen et al., 2013; Moilanen et al., 2013b). A phase-delayed excitation is a well known concept used for steering the wave field (sound waves or electromagnetic waves). A phase-delayed transmitter is composed of an arrangement of multiple sources in a way that the ensuing field superposition achieves the desired shape and intensity. It is widely used in surgery (cancer treatment), high intensity focused ultrasound (HIFU), imaging and other medical applications (Drinkwater and Wilcox, 2006; Dubinsky et al., 2007; Fan and Hynynen, 1996; Rebillard et al., 2008). In the context of axial transmission, individual transmitters of a linear phase-delayed array are launched with a shift in the phase of sequential transmitters so as to excite the FFGW or other guided mode with the corresponding speed. Excitation of each transmitter with a constructive phase of this mode thus amplifies its magnitude (fig. 14).

Phase-delayed excitation is tuned by the time delay (t_{pd}) in launching sub-

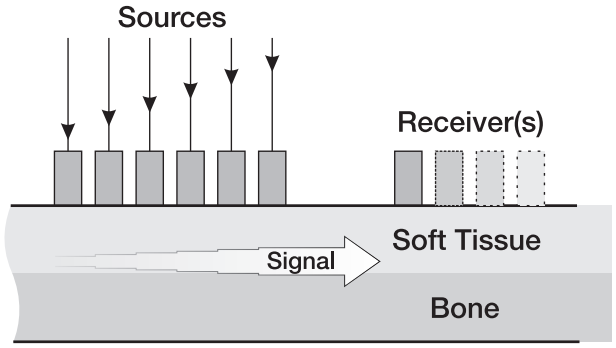

FIGURE 14 The basic concept of a phase-delayed excitation for axial transmission. Individual transmitters are launched sequentially, by tuning the time delay t_{pd} to match constructive phase of excitation at subsequent elements.

sequent elements. The time delay t_{pd} is tuned to match a constructive phase of excitation when (Karppinen et al., 2013)

$$t_{pd} = \frac{d}{c_{ph}(f)} - n\frac{1}{f}, \tag{38}$$

where d is the inter-element distance, $c_{ph}(f)$ the phase velocity of the desired US mode at frequency f and n is an arbitrary integer. An illustration of time delay curves thus tuned is shown in fig. 15. In an experimental situation, it is likely that $c_{ph}(f)$ is not known a priori. Therefore it is necessary to design an iterative method for automated tuning of the time delay using received magnitudes to determine the feedback.

In addition to using a constructive phase to amplify the FFGW mode, a phase-delayed excitation can also reduce the magnitude of interfering modes. These unwanted modes are reduced by tuning to their destructive phase, represented by a half-integer n in eq. (38). Tuning is often a tradeoff between maximization of the FFGW magnitude and minimization of the interference magnitude, as a single t_{pd} may not satisfy both of the two objectives. There is yet an option to tune t_{pd} by maximizing SIR directly. A phase-delayed excitation in bone mimicking coated waveguides is explored in IV.

3.4.5 Obstructing the propagation of interfering modes

Effective improvement of SIR requires yet further solutions as efficiency of the phase-delayed excitation is limited by matching the tuning so that it is constructive for FFGW and destructive for the interfering modes.

To this end we propose to obstruct US propagation in the layer of soft coating. Interference is predicted to be caused mostly by propagation of US modes in the soft coating, whereas most of FFGW is predicted to propagate in the bone subsystem (section 3.4.2). Therefore, by locally deforming the layer of soft coating (*i.e.* by a local indentation), it should be possible to reduce interfering modes which will pass less over the deformation because of their acoustic reflection back

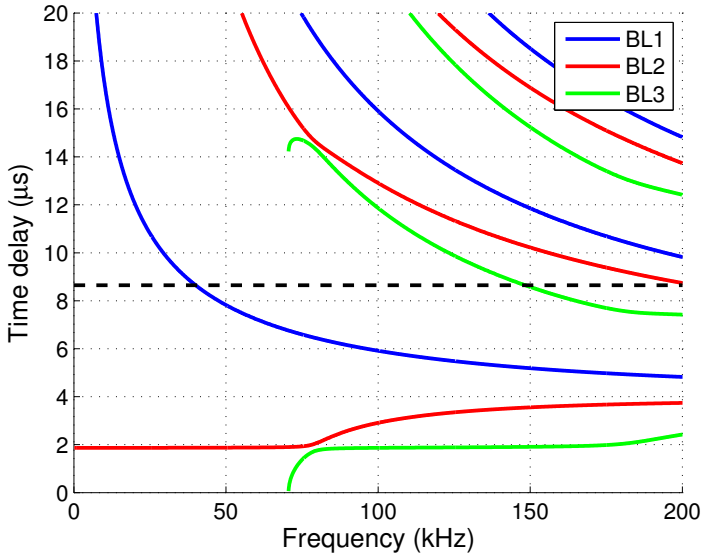

FIGURE 15 Dispersion of time delay parameter with respect to frequency for three modes (BL1–BL3) in a fluid-coated (7 mm) bone material plate (3 mm). The dashed black horizontal line represents a random time delay chosen. Modes that intersect with this line are predicted to be launched.

to the transmitter side. Such a deformation could be realized, for example, by a local mechanical compression of the soft tissue between the sources and receivers.

This method has been explored in Kilappa et al. (2014b).

4 OBJECTIVES AND COMPOSITION OF THE STUDY

The objectives of the study were:

1. To test the clinical feasibility of the conventional low frequency ultrasound method based on FAS (I and II)

2. To detect and automatically analyze an additional wave mode (FFGW) (III)

3. To solve the soft tissue -induced problem related to *in vivo* detection of FFGW (IV and Kilappa et al. (2014b))

Publications related to realization of each objective are cited in the brackets. Realization of objective 1 was divided into a correlation study (I) and fracture discrimination study (II). A specific aim of study I was to examine to which extent US measurements are predicted by reference bone property quantities assessed by clinical quantitative computed tomography. A specific aim of study II was to examine whether the US method is able to discriminate subjects with fragility fractures from non-fractured controls in postmenopausal subjects. Objective 2 was realized in III, where the specific aim was to examine a new signal processing method by modelling and experiments in bone phantoms and human bone *in vitro*. Realization of objective 3 was divided into analysis of phase-delayed excitation (IV), and analysis of obstruction of modes propagating in the soft tissue (Kilappa et al., 2014b). A specific aim of sub-studies IV and Kilappa et al. (2014b) was to examine by modelling the efficiency of these two methods proposed.

5 MATERIALS AND METHODS

5.1 Low frequency axial-transmission array transducer

A scematic view on a custom made array transducer, developed for this study, is shown in fig. 16. This array consists of a rigid frame, into which the individual transducers are attached. There are two transmitters and six receivers. Transmitters are isolated by air gaps to obstruct US cross talk between them. Futhermore they are embedded in a 9 mm thick layer of polyurethane. Material was chosen so that it had a strong absorption and a speed of sound slower than that in the soft tissue, so as to minimize its impact on US measurements. Transducer elements had a centre frequency of 200 kHz, bandwidth of 400 kHz (-16 dB) and diameter of 3 mm. The receiving unit has a 6 mm inter-transducer separation, and covers a source-receiver distance of 20–50 mm, symmetrically for both transmitters. The range covered is thus consistent with that of our earlier scanning US setup, while the latter permitted a finer pitch (typically <1 mm) (Moilanen et al., 2003).

Responses at each receiver were recorded at a sampling rate of 20 MHz and a voltage resolution of 8 bits by a digital oscilloscope (DAQCard-5102, National Instruments, Austin, TX, USA). Centre frequency of the resulting FAS wave packet appeared at approximately 400 kHz, while that of the FFGW wave packet appeared at 100-200 kHz.

Advantage of the new array transduced is that it permits correction in FAS measurements of the impact of soft tissue tapering. This correction is based on a bidirectional measurement technique (Bossy et al., 2004a), as expressed in section 3.4.1. To this end, each transmitter was excited separately, in a rapidly alternating sequence, and the resulting unidirectional FAS velocities were measured (c_+ and c_-, see eq. (37)). Times of flight for each of the six source-receiver distances were determined based on using the first maximum of the FAS wave front as the criterion. Linear regression was then used to determine the apparent unidirectional velocity. Bidirectional velocity of the FAS was then determined using eq. (37). Acronyms V_{FAS} and V_{LF} (low frequency) were used for the FAS velocity.

During recording, signals were averaged over 20 repeated pulses to reduce

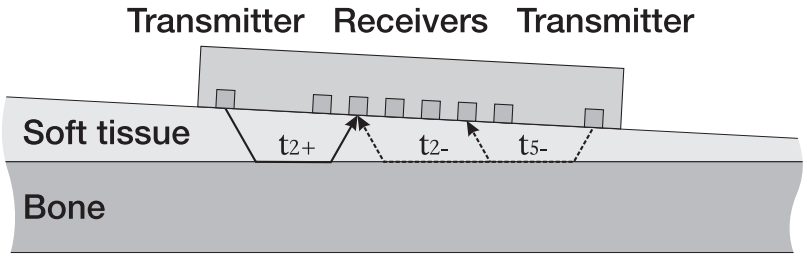

FIGURE 16 Schematic illustration of the array probe. Example signal paths from both transmitters to receivers 2 are marked with t_{2+}, t_{2-} and from the rightmost receiver to receiver 5 with t_{5-}.

noise. A single FAS measurement captured in this way required approximately one second to complete. The FAS measurement was then repeated 20 times, and inclusion of velocity data was then determined based on statistical criteria. During a measurement, the probe was held stationary once a proper positioning was found. Positioning was judged by the operator based on the quality of waveforms and velocity data seen on the screen. For both radius and tibia bone sites, this procedure was repeated three times with repositioning, in order to assess the reproducibility of results of the device and measuring method. In total, the complete measurement sequence for one bone site required about five minutes to complete. This was deemed rapid enough for clinical operation.

Performance of the array transducer in FAS measurements was evaluated in I and II. Suitability of the same array transducer for FFGW measurements was evaluated in III. In IV a modified version of the array was evaluated. In this case, the receiving array was considered as a phase-delayed transmitter and another multi-element array was used as the receiver.

5.2 Clinical studies

The first half of this Thesis is related to evaluation of the clinical performance of FAS measurements with a custom made LF AT QUS probe (section 5.1). This work was divided into two sub-studies, one of which assessed correlations between QUS and bone densitometry data (I) and second of which assessed the ability of QUS to discriminate fractures (II).

5.2.1 Subjects

Subjects of the study were those of a large family study CALEX (fractures in puberty cause implications at old age) in the Department of Health Sciences at the University of Jyväskylä, which had recruited (pre)pubertal females, their parents and grandparents from the Jyväskylä region so as to assess hereditary and nutrition effects on bone quality (Cheng et al., 2005, 2009; Völgyi et al., 2010). It focused on following the development of female bone quality through puberty

and its comparison with that of parents and grandparents.

The health background of subjects, including fracture information and personal physical activity, was estimated from a self-administrative questionnaire, and verified from medical records whenever possible. The time of terminus of menstruation was used to define the menopausal status. Of the persons participating in the ultrasound measurement part of the study, 291 were women of age 20 to 88 years. 9 of these were discarded due to missing health information, which was essential for their classification (menopause), and 16 were excluded as they had incomplete measurement sets (pQCT). Furthermore, the ultrasound V_{FAS} measurement failed for 12 of the subjects.

For the correlation study (I), persons with a history of low impact fractures ($n = 40$), or certain diseases (endocrinological diseases, liver disease, renal diseases or cancer) or medication (glucocorticoids, anticonvulsants, anti-osteoporosis medication, selective estrogen receptor modulator, thyroxine, contraceptives or hormone replacement therapy), which could have affected bone metabolism ($n = 100$), were not excluded from the study as this would have greatly decreased the number of subjects. Also, it was observed that their exclusion would not have significantly affected the correlation results. The final dataset contained 254 subjects, of whom 159 were pre- and 95 postmenopausal.

The fracture risk assessment used a subset of the above dataset, namely the 95 unexcluded postmenopausal subjects.

Similarly to FAS measurements, as the number of hormone replacement therapy users ($n = 32$) was large, no subjects were excluded because of medication which had affected bone metabolism in order to preserve a sufficient number of subjects. Six subjects were however discarded because of missing data (DXA), resulting in a total dataset of 89 postmenopausal women. This sample was representative of the general population with respect to DXA results, menopausal age, and medication (Kärkkäinen et al., 2010; Pakarinen et al., 2010).

Reported fractures were classified as low/moderate energy or high energy ones. Low/moderate energy (fragility) fractures were caused by e.g. a fall from the standing height or less, and high energy fractures were caused by a high energy trauma, e.g. a traffic accident or a crushing type of injury. In addition, fractures were classified according to the bone site and at what age the fracture happended.

Based on these data, subjects were divided into groups without fractures (NF, $n = 53$), those with low energy fractures during adulthood (21 years or older) (Fx, $n = 24$) and those with other fractures (OF, $n = 12$). The last group included high energy fractures and subjects, who had experienced toe or finger fractures, and subjects who had experienced fractures in childhood (20 years or younger).

Subjects were classified into four categories based on their reported physical activity in hours per week: none, about 1 h or less, about 2–3 h, and about 4 h or more.

Study protocol was approved by the ethical committee of the University of Jyväskylä and the Central Finland Health Care District. All subjects gave in-

formed consent prior to assessment.

The overall composition of the subject groups in the clinical studies is outlined in fig. 17.

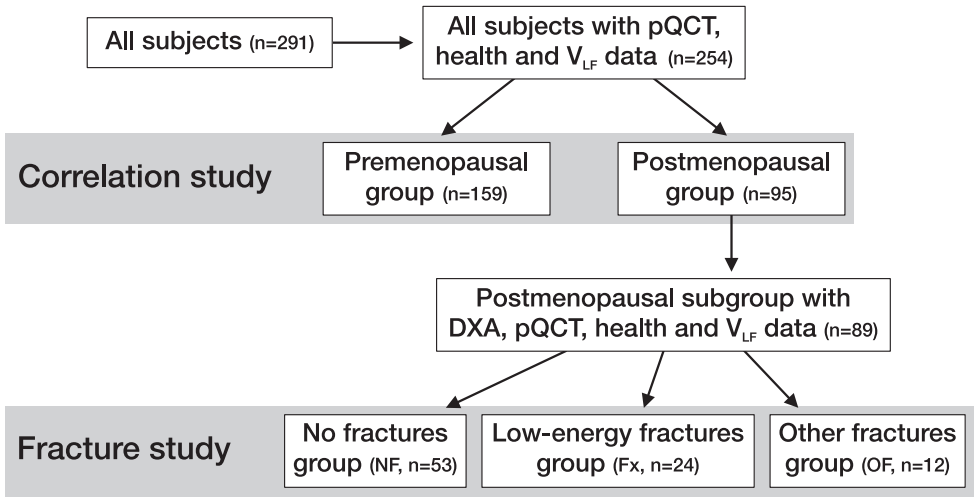

FIGURE 17 Flowchart describing the subject groups used in both the correlation and fracture studies.

5.2.2 QUS mesurement protocol

Assessment by low frequency axial-transmission ultrasound (LF-AT-QUS) was performed by our custom LF array probe (section 5.1 and fig. 16). Transmitter frequencies and the signal capture protocol are described above.

Measurements were performed at the distal end of the radius (probe centred at one third of the length of the radius to the proximal direction from the distal end) and tibia (probe centred at 60% of the length of the tibia from the lateral malleolus of the fibula in the proximal direction). Tangential positioning is shown in fig. 18.

Probe was aligned with the bone so that its centreline coincided with the location mentioned above in the proximal-distal direction. Probe was manually pressed against the radius, and mechanically against the tibia using a stepper motor. Compression load against the tibia was approximately 15 Newtons. The main reason for choosing the manual compression in the forearm was convenience, as forearm locations often had large amounts of soft tissue, and careful positioning was required for a stable measurement. In the case of tibia, the anteromedial ridge was typically covered by a very low amount of soft tissue, and a proper positioning of the probe was considerably more straightforward.

The longitudinal axis of the probe was aligned in the direction of the bone (radius or tibia). Proper alignment was expected to happen, when the apparent speed of sound had its maximum, and the successive signal delays in each transducer were similar. These properties suggested that the bone was at a similar or linearly changing depth below the soft tissue depth throughout the length of

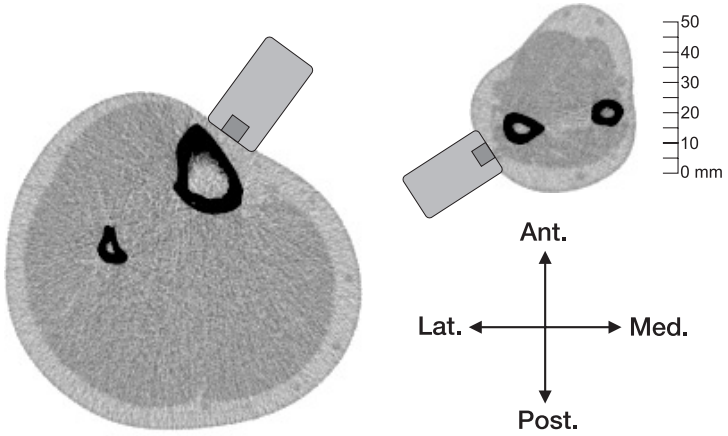

FIGURE 18 Tangential positioning of the array probe for both radius and tibia, superimposed with pQCT images of the measurement location.

the probe, and that none of the transducers was off the axis of bone. A completed measurement consisted of 20 signal samples. If their variance was too high, probe was repositioned and measurement was repeated. For each subject, at least three measurements were performed for the both radius and tibia, and the final result for each site was the average of these measurements.

5.2.3 Bone densitometry assessments

pQCT

Peripheral quantitative computed tomography (pQCT) measurements were performed with a Stratec XCT2000 device (Stratec Medizintechnik GmbH, Pforzheim, Germany) in the same physical locations as the V_{FAS} measurements. Properties investigated were the total bone mineral density (BMD), cortical BMD (CBMD), subcortical BMD (ScBMD) and cortical thickness (CTh).

All parameters were determined as averages over a single cross-sectional pQCT slice using the original Stratec software. Tissue types (cortical, subcortical, marrow, muscle, fat) were separated by their absorption coefficients. Voxel size was 0.59 mm. Scanning protocol and repeatability statistics were as in (Cheng et al., 2005; Wang et al., 2008; Xu et al., 2009). The coefficients of variation were less than 1% for the BMD measurements and 3.0% for the CTh measurements.

DXA

Dual energy X-ray absorptiometry (DXA; Prodigy, GE Lunar Corp., Madison, WI USA) was used to determine the areal bone mineral density (aBMD) of the whole body (WB), lumbar spine (L2–L4), femoral neck (FN) and total proximal femur (TF). A more detailed description of the DXA measurements has been given in (Cheng et al., 2005). The coefficient of variation for aBMD of WB, L2–L4, FN and TF varied between 0.9% and 1.3%.

5.2.4 Signal processing and statistical methods

SPSS version 15.0, later PASW Statistics version 18.0.0 (SPSS Inc. Chicago, IL, USA) and MATLAB (version 7.5, Mathworks Inc. Natick, MA USA) were used for statistical analysis of the data.

Correlation study

Pearson's correlation analysis was used to to assess the ability of bone mineralization and cortical thickness to predict V_{FAS}. In addition to single variable predictions, multivariate linear regression analysis was used to test whether more than one pQCT parameter in the same model could improve the V_{FAS} prediction. As the independent pQCT variables had known errors, we estimated also the total standard error of the estimate (SEE_{tot}) in order to assess the reliability of these models. This error can be defined such that (from Snedecor (1976))

$$SEE_{tot} = \sqrt{SEE^2 + \frac{PE_X^2/SD_X^2}{1 + PE_X^2/SD_X^2}(SD_Y^2 - SEE^2)}, \tag{39}$$

where SD_X and SD_Y are the standard deviations of the independent and dependent parameters, respectively. Imprecision of an individual estimate is given by

$$PE_{Est} = SEE_{tot}\sqrt{1 + \frac{1}{n} + \frac{(X - \overline{X})^2}{\sum(X_i - \overline{X})^2}}, \tag{40}$$

where n is the number of measurements used in the creation of the linear model.

Bland-Altman plots (Blake and Altman, 1986) were used to visually inspect the quality of the linear estimates.

The repeatability error CV_{RMS} of the *in vivo* measurements was determined from the reproducibility of the three successive measurements of the same subject with repositioning. This procedure was performed for the whole subject population and the obtained CV_{RMS} was 0.47% for the radius (95% CI: 0.11-0.95%) and 0.45% for the tibia (95% CI: 0.06-1.21%). In phantom calibration studies, the short term reproducibility of the array probe was only 0.07%, equal to a velocity error of 1.8 m/s, which suggests that the *in vivo* errors mostly arise from alignment and contact problems.

The standardized coefficient of variation (SCV), defined as CV_{RMS} over the range of measured values (which, in turn, is typically defined as 4×SD (Miller et al., 1993; Orgee et al., 1996)) for healthy individuals, were approximately 5.9% and 9.8% for the radius and tibia, respectively.

Fracture study

One way ANOVA was used to test differences between the NF, Fx and OF groups. Scheffé test was used for normally distributed variables. For non-normally distributed variables, comparison between groups was done using the Mann–Whitney U test. Chi-square test was used for comparison between groups of categorical variables. An independent sample Kruskal–Wallis test was used to compare the physical activity of the NF, Fx and OF groups. In order to assess the discriminatory ability of different measurements in the case of low/moderate trauma fractures (*i.e.* to discriminate the Fx group from the NF group), the odds ratios (OR) were determined using the binomial logistic regression analysis. ORs were expressed as increases in the estimated fracture risk per difference by one standard deviation.

In order to estimate the sensitivity and specificity of the different measurements in the discrimination of fracture subjects, the receiver operator characteristic (ROC) curves and the areas under these curves (AUCs) were determined. Age and body mass index (BMI) were used as covariates when determining adjusted ORs and AUCs. Differences between AUCs were compared statistically using the method of Hanley and McNeil (1983). T-scores were determined based on a small reference population consisting of 58 females of age 20–40 years. Validity of using this small reference population was confirmed against the established DXA reference data for Finland, and then used as a reference of young healthy adults in our study when determining the T-scores.

5.3 FFGW signal analysis

The main motivation for III was the necessity to find a method, in which the properties of FFGW could be extracted from an array transducer measurement. Before delving into a description of the method developed for the array probe, we outline the basic concepts needed to understand the results and the operation of our previous signal analysis method for AT scanning measurements (sections 5.3.1 and 5.3.2). In section 5.3.3, we focus on describing the replacement method for the array probe.

5.3.1 Representation of spatio-temporal signals (RT diagrams)

A distance-time (RT) diagram is a basic tool for visualization of axial transmission signals. It is a 2D representation of a spatio-temporal signal, where individual time domain signals from different distances are displayed beside each other, in order to give an impression of the evolution of the signal through the measurement range. A typical RT diagram from a scanning ultrasound measurement represented as a grayscale image is shown in fig. 19.

For signals recorded by an array transducer, where there are a limited num-

ber of source-receiver distances (6 in our case), it is useful to visualize the RT diagram directly as temporal waveforms, as shown in fig. 20.

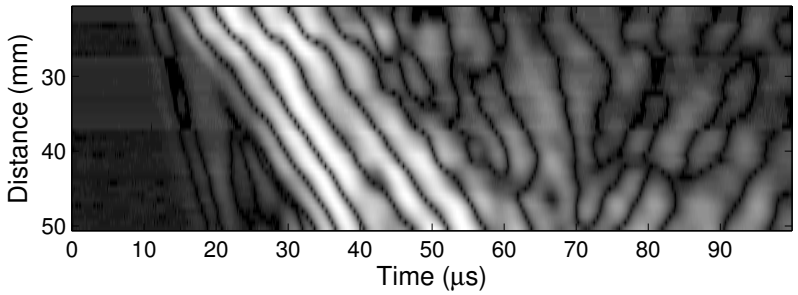

FIGURE 19 An RT diagram recorded by the scanning ultrasound device in an *in vitro* human radius. Since there was no soft tissue, FFGW wave packet is clearly visible as the most energetic contribution. FAS wave front appears as a fainter, straight slope on the left. The temporal and spatial resolutions in the image are 10 MHz and 0.75 mm.

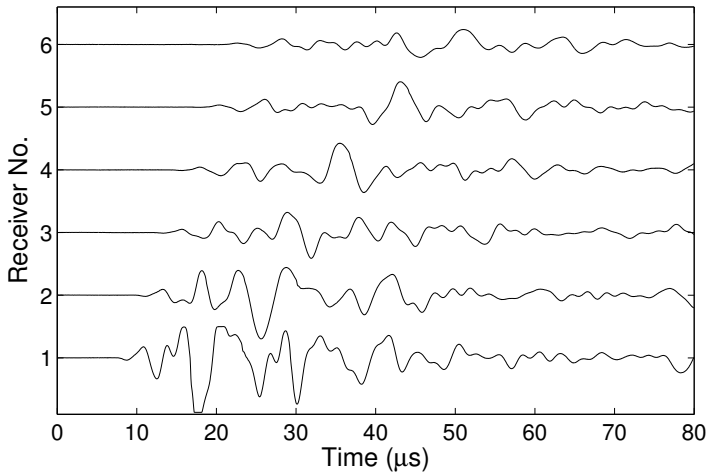

FIGURE 20 An RT diagram with six source-receiver distances recorded by the array transducer in an acrylic plate phantom, represented simply as a sequence of stacked time domain waveforms.

5.3.2 Mode separation by spectral analysis

This method had originally been developed for mode separation for the scanning US receiver (Moilanen et al., 2006), which permits a fine spatial inter-element separation (pitch). In the present work, the method was also used as a reference method for analyzing simulations, where it was possible to introduce a receiver with sufficiently small pitch.

Two dimensional fast Fourier transform (2D-FFT)

Two dimensional fast Fourier Transform (2D-FFT) (Alleyne and Cawley, 1991) was used as a reference method in III and as the main separation method in IV and in Kilappa et al. (2014b) for FFGW assessment. 2D-FFT is a method, wherein spatio-temporal signals are transformed into wave number–frequency space for mode separation and identification. A traditional FFT is first performed in the temporal dimension, to get a distance–frequency space, and after this, in the spatial dimension to get the wave number–frequency space desired (fig. 21). Wavenumbers can then be transformed into phase velocities so as to find a phase velocity–frequency diagram shown in fig. 8 by

$$c_{ph} = 2\pi f / k. \tag{41}$$

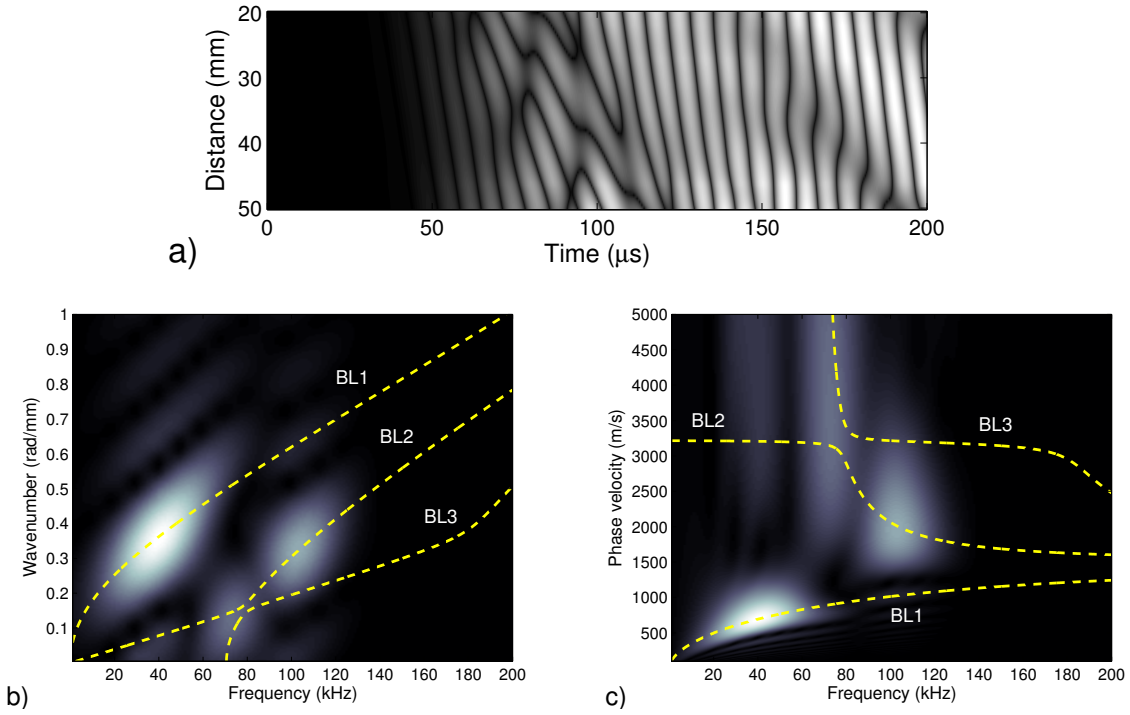

FIGURE 21 Mode separation by 2D-FFT. (a) Spatio-temporal signals, recorded in a simulated, fluid-coated (7 mm) bone material plate (3 mm thick), are represented by an RT diagram. Related 2D-FFT is represented (b) in the frequency–wavenumber plane and (c) frequency–phase-velocity plane. Observed loci of intensity maxima are identified based on related theoretical predictions superimposed (dashed curves). In this case, the RT diagram was post-processed by group velocity filtering, as illustrated in fig. 23.

Dispersion curves obtained in this way can be used to approximate the properties of the waveguide for which they were determined. Loci of the maxima in the frequency–velocity space are obtained, which can then be compared with

seminalytically determined dispersion curves. Best fits of loci by these semianalytically detemined curves with the elastic and/or geometric parameters as fitting parameters can be used to approximate these parameters (Karim et al., 1990; Moilanen, 2004; Moilanen et al., 2006).

Accuracy of the spectral representation relies on the resolution (both temporal and spatial sampling interval) of the signal data. Because of the Nyqvist-Shannon sampling theorem, the highest frequency (f_{max}) visible in the figure is $f_s/2$, where f_s is the sampling rate. The phase velocity range which can be investigated, on the other hand, is limited by the the highest and lowest wavenumbers which can be resolved for a given spatial sampling resolution. The highest measurable wavenumber is limited by the sampling interval in the distance domain. The Nyqvist-Shannon theorem requires that two samples are needed in the distance direction of the R–T diagram for the wave to be resolvable, so $k_{max} = 2\pi/(2d)$, where d is the inter-element separation, and this can be used with eq. (41) to find $c_{phmin} = 2\pi f/k_{max}$. A graphical representation of the limits induced by various inter-element separations is shown in fig. 22. It is evident from this figure that the six millimeter inter-element separation used in our array probe severely constrains the phase velocity range which can be observed, and as such, does not allow for a proper identification of guided wave modes by 2D-FFT.

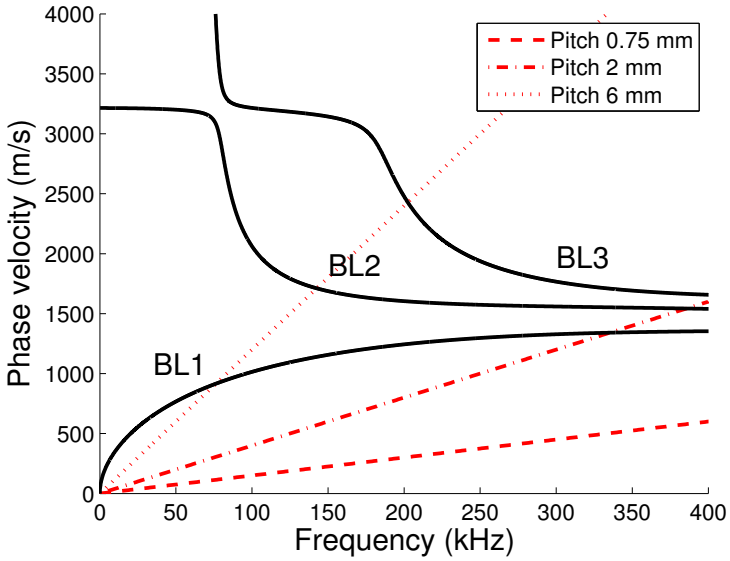

FIGURE 22 Nyqvist-shannon sampling theorem limits the lowest phase velocity resolvable by 2D-FFT. Effect of the lowest resolvable phase velocity for each frequency is shown for inter-element separations of 0.75 mm (lower dashed red line), 2 mm (middle dot-dashed red line) and 6 mm (upper dotted red line) 1 mm. Black curves correspond to semi-analytical predictions of dispersion curves for a bilayer model with a 3 mm bone material plate with 7 mm layer of soft coating.

Enhancement of mode separation by group velocity filtering (GF)

Group velocity filtering is a signal processing method, where a spatio-temporal (r,t) signal is masked by a stationary gate window so as to extract the time region of iterest prior to 2D-FFT is performed, and to mask out regions, whose presence is adverse to this operation. In practice, (r,t)-matrix is multiplied by a Hann windowing function with a pass region of the type

$$w_n = sin^2\left(\frac{\pi n}{N-1}\right), \tag{42}$$

where n is a sampling point inside the window and N is the total number of samples (indexed from 0 to $N-1$). Midpoint of the window is placed over the chosen region in the signal, and has a specific time-distance slope, determined either visually or by semianalytical expectations of the measurement scenario. A more precise form given in the (r,t)-space by

$$w(r,t) = \begin{cases} 0; & \text{if } t < t_d + \frac{r}{c_w} - t_w/2 \text{ or } t > t_d + \frac{r}{c_w} + t_w/2 \\ sin^2\left(\frac{\pi(t-\frac{r}{c_w}-t_d-t_w/2)}{t_w}\right); & \text{otherwise} \end{cases}, \tag{43}$$

where t_d is the delay of the window in time, measured at the centre of the window, t_w is its width and c_w is the speed (slope) of the window through the RT diagram (fig. 23).

This filter is used mainly for FFGW analysis (Moilanen et al., 2006). When the gate window covers the FFGW wave packet and as little of the rest of the signal as possible, including interference of FFGW with modes propagating in the soft tissue, the signal to 'noise' ratio is improved. The Hann function is commonly used as a windowing function in digital signal processing, as such a window is low aliasing, does not dramatically disturb the FFT and only slightly decreases the resolution.

A limitation of using GF is that tuning of the filter parameters needs a priori information about the time of flight of FFGW. On the other hand, choice of the filter parameters may affect the result of the 2D-FFT.

5.3.3 Method of mode separation for array transducers

Implementation of the array probe (section 5.1) is such that device does not scan along the measurement axis, and thus has a more limited spatial sampling resolution, constrained by the pitch of the receivers. In order to construct a spectral analysis method for this probe, we describe a method of spectral analysis for single transducer measurements, and outline how it can be used with a multi-ridge based method of mode separation and reconstruction.

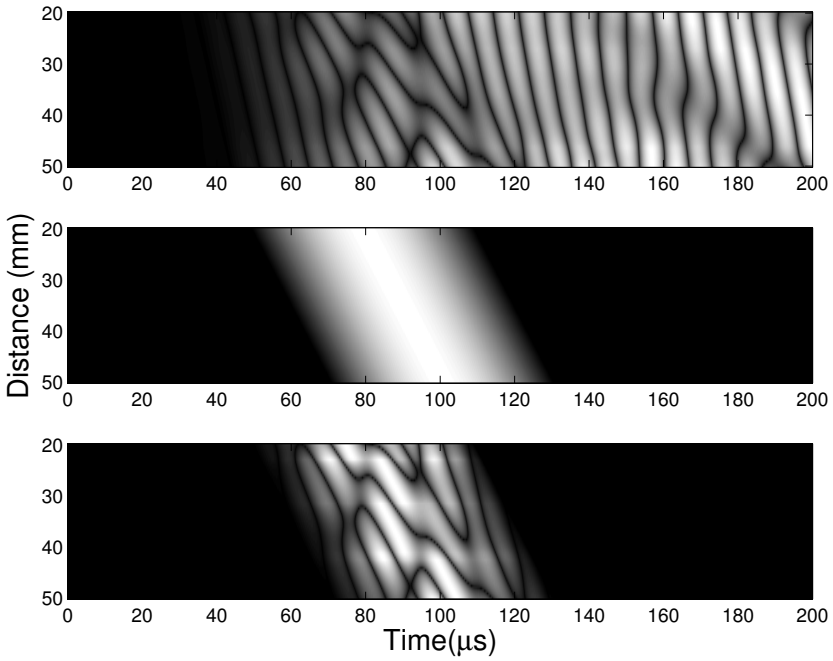

FIGURE 23 A group velocity filter multiplies a spatio-temporal signal (top panel) by a Hann window (middle panel), so as to extract the temporal region of interest (bottom panel) that in this case is associated to the FFGW wave packet. Signals were recorded in simulations in a 3 mm bone material plate with 7 mm layer of soft coating.

Short time Fourier transform and time-frequency representation

A time-frequency representation (TFR) is a view of a single temporal signal, displayed as a function of time and frequency. The objective of such a transformation is to provide insight into the frequency content of the signal at various time scales and loci, and to investigate the evolution of the frequency content over time. There are several methods for producing such representations with varying windows, distributions and transform types (Cohen, 1989; Daubechies, 1990), but here we focus on the short time Fourier transform (STFT). The basic principle of STFT is to use a Fourier transform after passing the original signal via a moving gate window, so as to determine the instantaneous frequency properties near a specific time. In our application, we used a so called Gabor transform, which means an STFT together with a Gaussian window. The width of the window was chosen to be $3\mu s$, which was an experimental compromise between accuracy in the time and frequency domains.

For a signal $s(t)$, STFT can be expressed in the form

$$TFR_{STFT(s(t))}(u,\omega) = \int_{-\infty}^{\infty} e^{-i2\pi\omega t} s(t) h(t-u) dt, \tag{44}$$

where $h(t)$ is the window function. Energy density of this transformation is the spectrogram, defined as $E(u,\omega) = |TFR_{STFT}(u,\omega)|^2$.

In the context of guided ultrasound modes, parts of the FFGW mode are typically visible and separate from other propagating modes, as they appear at different frequencies. An example of a TFR for a single time domain signal is shown in fig. 24. In this figure, mainly the contribution of the FFGW (A0) wave mode can be seen in the TFR.

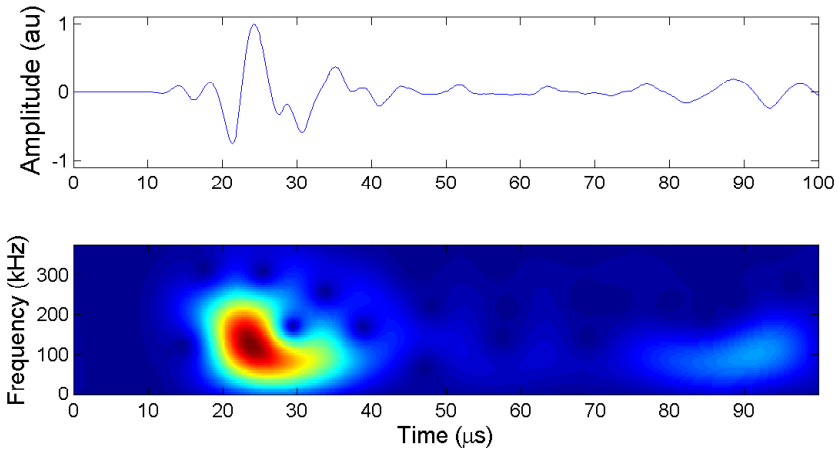

FIGURE 24 A time domain waveform recorded in a 2.8 thick acrylic plate (top panel) and related time-frequency representation (TFR; bottom panel). The magnitude of TFR is represented by a colour scale.

Enhancement of mode separation using multiridge analysis based on the crazy climber (CC) algorithm

As a replacement of GF filtering in the FFGW analysis, we evaluated a multiridge -based method of signal analysis and waveform reconstruction, as described by Xu et al. (2010), and based on the work of Carmona et al. (1999); Gilks et al. (1995). This method was used to identify guided wave modes from TFR of a recorded waveform by a so called crazy climber (CC) algorithm, and further to reconstruct individual FFGW waveforms from the separated modes. In the Thesis, the acronym CC is used to describe the signal processing, mode separation and reconstuction process in its entirety, but in this Section we introduce each step of this analysis separately.

After construction of TFR, an annealing signal processing algorithm based on the Markov chain Monte Carlo approach (Gilks et al., 1995) will be used on the resulting image to identify the local maxima of the signal. This algorithm operates on the positive frequency region ($D = (t > 0, f > 0)$) of the TFR space. A 2D image (fig. 24) $m(t,f)$ of the corresponding region is produced by discretizing the modulus of the TFR in both time and frequency space ($t = 0,\ldots,t_{L-1}$, $f = 0,\ldots,t_{M-1}$. In essence, $m(t,f)$ then simply becomes a real $L \times M$ matrix.

Operation of the climbers can be described such that (Xu et al., 2010):

1. Climbers are initialized by placing them in uniformly random positions in D, such that $X(t_0) = (j,k); j = 0,\ldots,t_{L-1}; k = 0,\ldots,k_{M-1}$. Temperature is set to $temp_0$.

2. Climbers are independent of each other so that it is sufficient to discuss the properties of a single climber. Assuming a climber at point $X(t) = (j,k)$ at time t, its position $X(t+1) = (j^*,k^*)$ at time $t+1$ will be arranged in two steps. Horizontal position (time) is adjusted first.
   If $1 \leq j \leq T_{L-1} - 1$, the climber can move to the either left or right with the same probability $P(j^* = j+1) = P(j^* = j-1) = \frac{1}{2}$. Then the vertical (frequency) adjustment is executed by moving the climber up $(k^* = k+1)$ or down $(k^* = k-1)$ with probabilities dependent upon the amplitude of the discretized TFR. If $|m(j^*,k^*)| > |m(j^*,k)|$, then $X(t+1) = (j^*,k^*)$, and if $|m(j^*,k^*)| < |m(j^*,k)|$, the climber will move to $X(t+1) = (j^*,k^*)$ depending on probability $P_t = exp((|m(j^*,k^*)| - |m(j^*,k)|)/temp_t)$, and to $X(t+1) = (j^*,k)$ with probability $1 - P$.
   After the movement step is done, temperature is decreased step by step. It has been proved that the system will converge to a global minimum if $temp_t = temp_0/log_2 t$.

3. The algorithm will terminate, when the temperature reaches a given threshold.

Thus, in essence, CC uses a specific random walker to traverse the potential field generated from the TFR image and when the transition probabilities are lowered, the climbers are localized in the neighbourhoods of the local maxima of the image. At this point, adjacent climbers are chained together, and stray ones, which do not form ridges of sufficient size (length), are discarded.

The completed, 'chained' ridges now mark the most energetic components of the measured signals in the time-frequency space, and can be used to reconstruct the corresponding temporal waveforms (Carmona et al., 1999; Xu et al., 2010). A separated waveform can be reconstructed by minimizing a sesquilinear functional with linear constraints determined from the TFR intensity of the corresponding ridge (fig. 25b). TFR ridge defines the reconstruction constraints, as for each time-frequency point of the ridge, the difference between the components of both the original and reconstructed TFR are minimized. For a more detailed description of the reconstruction process, see Xu et al. (2010).

For our purposes, it was crucial to focus on detecting FFGW, best detectable at low ultrasound frequencies (<100kHz). Given that in typical ultrasound measurements, FFGW is both the lowest frequency contribution and its group velocity can be predicted from semianalytical models, this was relatively straightforward. Once the component was identified, the aim was to determine its group velocity. For this purpose, local maxima at a given frequency in the time axis of the TFR image were used to indicate the times of flight (ToF) of the FFGW waveform envelope for each source-receiver distance fig. 26. Speed of sound, as determined by linear regression for the ToF points obtained, was then used to represent the group velocity of FFGW.

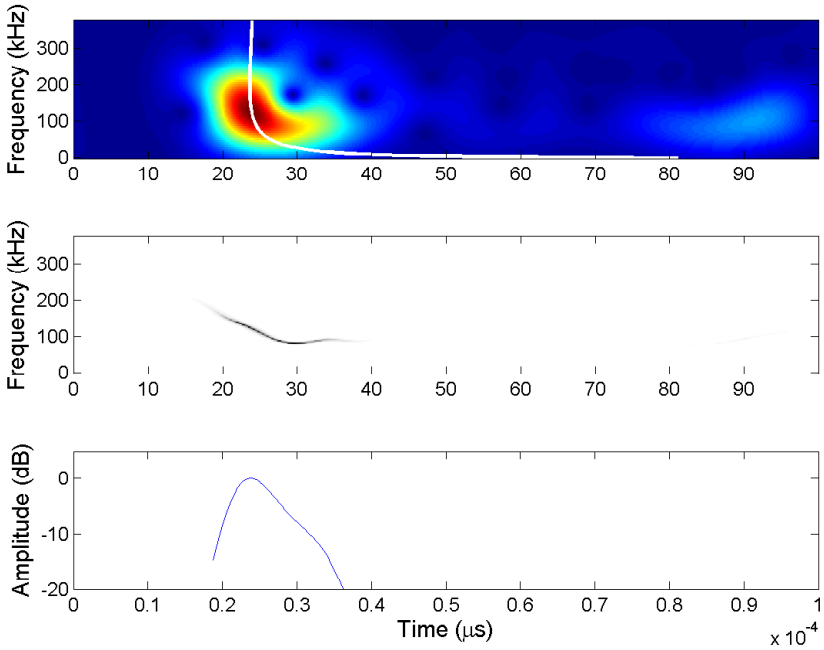

FIGURE 25 Phases of operation of the CC method. Loci of intensity maxima (red) observed in TFR plane is consistent with the time of flight (ToF) theoretically predicted by A0 (solid curve) group velocity at a known source-receiver distance (top panel). The detected loci of intensity maxima (middle panel). The TFR amplitude determined along the detected loci of intensity maxima (bottom panel). Results are illustrated for a 2.8 mm thick acrylic plate, measured by the scanning ultrasound device.

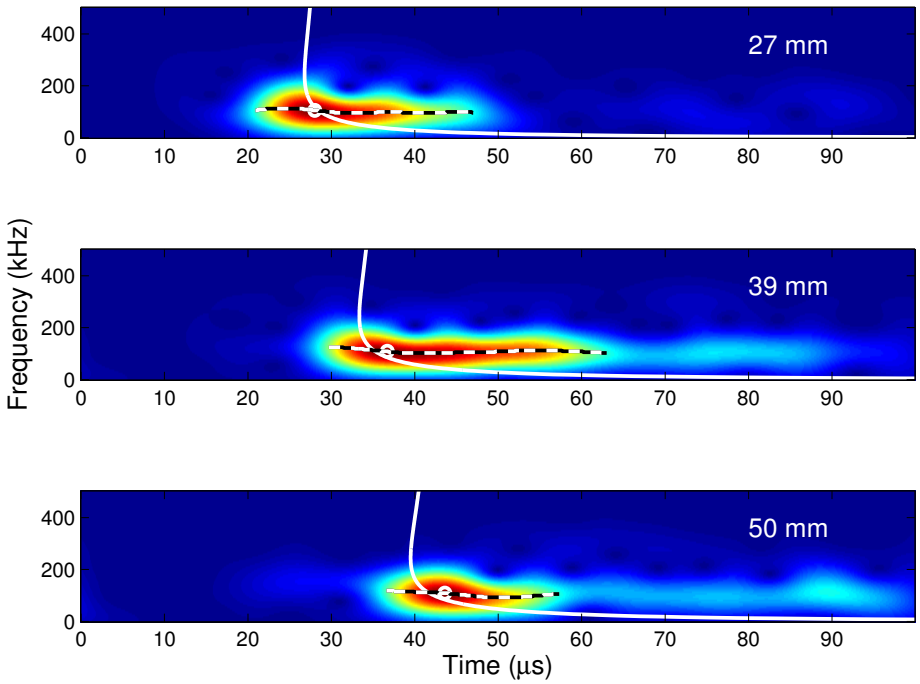

FIGURE 26 Assessment of ToF with respect to source-receiver distance by the CC method in an *in vitro* human radius. The local maxima of TFR magnitude (circles) determines the times of flight of FFGW. A theoretical prediction (A0 mode) is shown by the solid line (exact reference material properties and cortical thickess were not known, the prediction is based on 4000 m/s, 1800 m/s and 3 mm for the compression bulk velocity, shear bulk velocity and cortical thickness, respectively).

5.4 Measurements for FFGW signal analysis

5.4.1 Samples

Seven acrylic plates of 2–12 mm thickness were used as bone phantoms. In addition, former *in vitro* measurements on human radius specimens were reanalyzed (n=41) (Moilanen et al., 2007a; Muller et al., 2005, 2008).

5.4.2 Ultrasound measurements

Measurements with different AT ultrasound devices were used in this study. The new AT array probe was the main device which was tested (section 5.1). Reference measurements with a higher resolution in spatial sampling were obtained by the earlier AT scanning device (Moilanen et al., 2003).

As the objective was to study the possibility of recovering group velocity information about FFGW from measurements with a limited resolution in spatial sampling, both devices were used to measure the acrylic plates with a resolution of 6 different source-receiver distances across the scanning length, normalizing to the specifications of the ultrasound device with an array probe. Measurement position was centred on the plate, and the plates were large enough to avoid boundary effects. In addition, the scanning device was used to measure the acrylic plates also with a higher spatial resolution (40 distances), as opposed to the lower resolution of the array device (6 distances). Scanning length with both devices was 30 mm.

Bone samples had been measured earlier with the scanning AT ultrasonometer (Moilanen et al., 2007a; Muller et al., 2008). In these measurements, measurement position was centred at about 45% of the length of the bone, measured from the distal end, and measurement direction was towards the proximal end. Azimuthally, the probe had been positioned in the posterolateral direction. Cortical thickness and BMD from the same site had been determined by pQCT (XCT 2000 pQCT scanner, Stratec Medizintechnik GmbH, Pforzheim, Germany), as described in section 5.2.3, with the exception that the voxel size was 0.2 mm. As the original bone samples no longer were available, they could not be measured with the array device. Signals of a limited number of source-receiver distances were produced from the original measurements by the scanning device by selecting six evenly spaced source-receiver distances, corresponding to those of the array probe.

Aquasonic ultrasonic gel was used as a contact agent in all these situations. The AT scanning device measurements were used as the reference data. As the main purpose of the study was to determine, whether group velocity could be determined from AT array probe signals, it was not considered important that the measurement situations of the devices were not exactly analogous. The main distinguising factor was that the scanning measurements did not contain the bilayer effect of the polyurethane frame material of the array probe. However, this

matter was not considered relevant with respect to the signal processing methods investigated.

5.5 Finite element time-domain simulations

The time-domain finite element method was used to simulate ultrasound experiments in III; IV and Kilappa et al. (2014b). Advantage of numerical simulations in comparison with real experiments was that it permitted a parametric analysis based on a sufficient number of repeated experiments, by just letting the computer to do the parametric sweeps. Related analysis with real experiments would have been time consuming or even non-existent with the equipment we had available at the time. Moreover, numerical simulations permitted analysis of materials and geometrical details of the sample or measurement setups, which were not easily accessible for experiments. In simulations we also analyzed idelized waveguide geometries so as to provide an optimal similarity with theoretical assumptions. This reduced the impact of experimental uncertainty in the analyses, and aided us in the construction of the real equipment. Nevertheless, accuracy of the results was limited to some extent by limitations of the signal processing used.

Numerical simulations were realized by two approaches, a custom made FEM code based on the Numerrin platform and a FEM model based on Comsol Multiphysics (section 5.5.1). Simulation problems analyzed are summarized in sections 5.5.3 and 5.5.4.

5.5.1 Simulation tools

Numerrin

A custom made FEM code based on Numerrin (Numerola Ltd, Jyväskylä, Finland) had been developed for Moilanen (2004). This model had later been improved by adding a fluid coating, and then be used for simulations in III.

The Numerrin platform is a general FEM solver for differential equations. Our model realized the following equation for solids (Huttunen, 2004):

$$\rho \frac{\partial^2 \vec{u}}{\partial t^2} - \mu \Delta \vec{u} - (\lambda + \mu) \nabla (\nabla \cdot \vec{u}) = 0 \tag{45}$$

where $\vec{u}$ is the displacement field, and λ and μ are the Lamé constants for an isotropic elastic solid. The equation used for fluids was (Huttunen, 2004):

$$\frac{1}{\partial c^2} \frac{\partial^2 p}{\partial t^2} - \frac{1}{\rho} \nabla^2 p = 0 \tag{46}$$

where p is the pressure and ρ the mass density of the fluid. Transmission conditions between the fluid and solid are given by

$$T^{\vec{n_1}}(\vec{u_1}) \cdot \vec{n_1} = -p_2 \tag{47}$$

$$\omega^2 \vec{u_1} \cdot \vec{n_1} = -\frac{1}{\rho_2} \frac{\partial p_2}{\partial \vec{n_2}} \tag{48}$$

where domain 1 represents the solid and domain 2 the fluid: $\vec{n_1}$ and $\vec{n_2}$ are correspondingly unit vectors normal to the fluid-solid (solid-fluid) interface. T is a traction operator which maps a local displacement to a force (pressure) at the interface.

Equations (45) and (46) were discretized using the spectral element method and central differences, as described for example in (Cohen, 2001). For Eq. (45), this discretization process first lead to

$$M\frac{\partial^2 U}{\partial t^2} + KU = \vec{g}, \tag{49}$$

where K and M are the finite element mass and stiffness matrices, respectively, while $\vec{g}$ is the source signal. U contains the values of the displacement components in each node. Discretization in the time domain, such that timestep $i+1$ is calculated from the two previous timesteps, is given by[1]

$$MU_{i+1} = M(2U_i - U_{i-1}) - \Delta t^2 K U_i + \Delta t^2 \vec{g}_i. \tag{50}$$

Comsol Multiphysics

Simulations in IV and Kilappa et al. (2014b) were performed by COMSOL Multiphysics (versions 4.2-4.4; COMSOL Inc., Burlington, MA, USA). Advantage of this commercial FEM modelling software was the graphical user interface which permitted a flexible tuning of the simulation geometry, whereas the simulations implemented in the Numerrin platform consisted of a research code with limitations in flexibility. Fluid coated plates were modelled using a transient acoustic-structure interaction module.

5.5.2 Modelling of FFGW detection with an array transducer

For generating measurements similar to those with the array probe, a 2D model based on the custom made Numerrin code was used to model single layer and bilayer waveguides. The bilayer waveguide was used to mimic the coupling between the polyurethane frame material of the array probe and the plate it was used to measure. The scanning ultrasound experiments, on the other hand, were modelled by single-layer plates, as the scanning US setup was better represented by this geometry (fig. 27).

[1] Both eq. (49) and eq. (50) have an error in the original article. In the first equation, the partial derivative is with respect to r instead of t, and in the second equation, the text incorrectly talks about timestep i, when it should talk about $i+1$.

The soft polyurethane frame material of the probe was modelled as a layer of ideal fluid (9 mm) on top of the plate (and surrounding the transmitters). The air gaps in the real transducer between the three polyurethane blocks fig. 16 were ignored. Source was excited by a 120 kHz pulse to reproduce the centre frequency of FFGW observed in real experiments. The length and pitch of the simulated receiver arrays were consistent with that of the actual device being emulated (see section 5.1 and Moilanen et al. (2003)).

Known material properties from literature were used in the simulations (Bossy et al., 2002; Moilanen et al., 2006; Selfridge, 1985). For acrylic, the compression velocity is $c_L = 2730$ m/s, the shear velocity is $c_T = 1260$ m/s and the density was $\rho = 1.19$ g/cm^3. Bone was considered isotropic with a compression velocity of $c_L = 4000$ m/s, a shear velocity of $c_T = 1800$ m/s and a density of $\rho = 1.85$ g/cm^3. Polyurethane was modelled as an ideal fluid with a compression velocity of $c_F = 1760$ m/s and a density of $\rho = 1.10$ g/cm^3. Parametric analysis included repeating the experiments in 1–6 mm thick plates, so as to well cover the range of wall thicknesses typical of the human radius (Muller et al., 2005; Moilanen et al., 2007a).

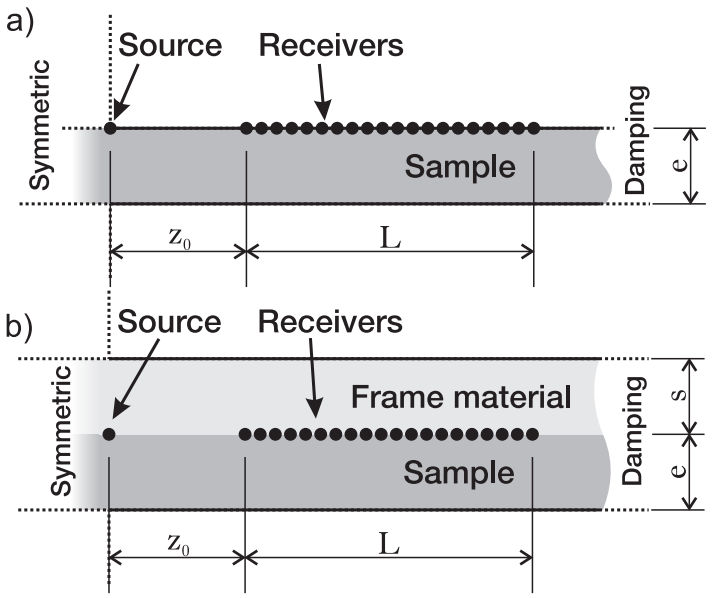

FIGURE 27 Simulation geometries corresponding to that of (a) the scanning ultrasound device and (b) device based on using the ultrasonic array probe. The solid black lines represent traction-free boundaries. The closest source-receiver distance was $z_0 = 20$ mm, scanning length was $L = 30$ mm, plate thickness was $e = 1$–6 mm and thickness of the soft frame material was $s = 9$ mm.

5.5.3 Modelling of tailored excitation with a phase-delayed array source

For modelling experiments with a phase-delayed excitation, a 2D COMSOL model was used.

In 2D simulations we used a solid plate covered by a layer of fluid, mimick-

ing bone covered by soft tissue (Bossy et al., 2002; Moilanen et al., 2008; Chen et al., 2012). Bone material was modelled as an isotropic linear elastic solid with a compression velocity of $c_L = 4000$ m/s, a shear velocity of $c_T = 1800$ m/s and a density of $\rho = 1.85$ g/cm^3 (Bossy et al., 2002, 2004a; Moilanen et al., 2007b). Soft tissue was modelled as an ideal fluid with a compression velocity of $c_F = 1481$ m/s and a density of $\rho = 1.00$ g/cm^3 (Camus et al., 2000; Dodd et al., 2006; Moilanen et al., 2008; Chen et al., 2012). Thickness of the plate was varied between 2 and 6 mm and that of the coating between 2 and 8 mm.

Source array was composed of six equally spaced elements (pitch 6 mm, 2 mm wide elements) placed on top of the fluid coating. Excitation at the transducer nodes was modelled by altering the acoustic pressure using a 50 kHz Gaussian modulated waveform with a 30 kHz bandwidth (-6 dB). For tuning a phase-delayed excitation (time delay parameter 0–15 μs), simulation was repeated with 0.2 μs intervals. An array of 61 virtual point receivers (pitch 0.5 mm, 30 mm long) was placed on top of the fluid, 20 mm away from the last source array transducer. An identical receiver array was placed at the same horizontal position, but on the fluid-solid interface. The receiving arrays recorded the normal components of particle velocities at each receiver. The reason for this was that particle velocity squared is linearly related to the power of the signal, independent of frequency, allowing a direct estimation of the power of the signals received.

On the top and bottom sides of the coated plate, traction-free boundary conditions were imposed (solid: free boundary model, fluid: sound-soft boundary model), corresponding to zero acoustic pressure at the fluid surface and zero stress at the solid surface. The vertical boundaries were absorbing (solid: low reflecting boundary model, fluid: plane wave radiation model) so as to damp reflections. Moreover, the simulation volume was sufficiently stretched at each end to avoid boundary effects and the propagation of any reflections into the regions of interest of the transmitter and receiver arrays.

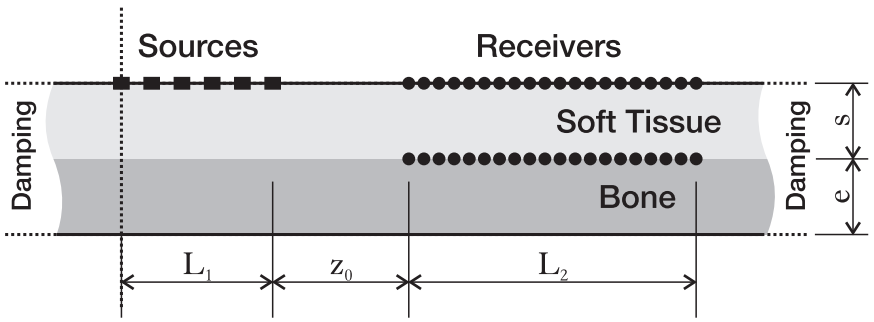

FIGURE 28 Geometry of simulated experiments with a phase-delayed array source. Plate thickness was $e = 2$–6 mm, thickness of soft coating was $s = 2$–8 mm, source-receiver separation was $z_0 = 20$ mm and length of the source and receiver arrays were $L_1 = L_2 = 30$ mm.

FFGW and the region of modes interfering with it were identified from the 2D-FFT mode maps recorded by the receiver array (fig. 29). Magnitude of FFGW was determined as a local maximum in the neighbourhood of the dispersion

curve predicted for the BL1 mode. Maximum of the signal typically appeared slightly above a frequency of 40 kHz. Magnitude of the other and especially interfering modes was determined as the maximum of the signal in the regions 60–125 kHz and 1500–10000 m/s. These regions covered the dispersion curves predicted for the BL2 and BL3 modes. These two modes predicted the interfering contributions observed. It was not possible however to distinguish the relative roles of the individual modes in a 2D-FFT mode map. The signal to interference ratio (SIR) was determined in decibels from the power ratio of FFGW and noise (incuding interfering contributions), such that magnitude squared represented the relative power. The magnitudes and SIR were evaluated within a limited time window extracted by group velocity filter (width 60 μs) aligned with the FFGW wave packet.

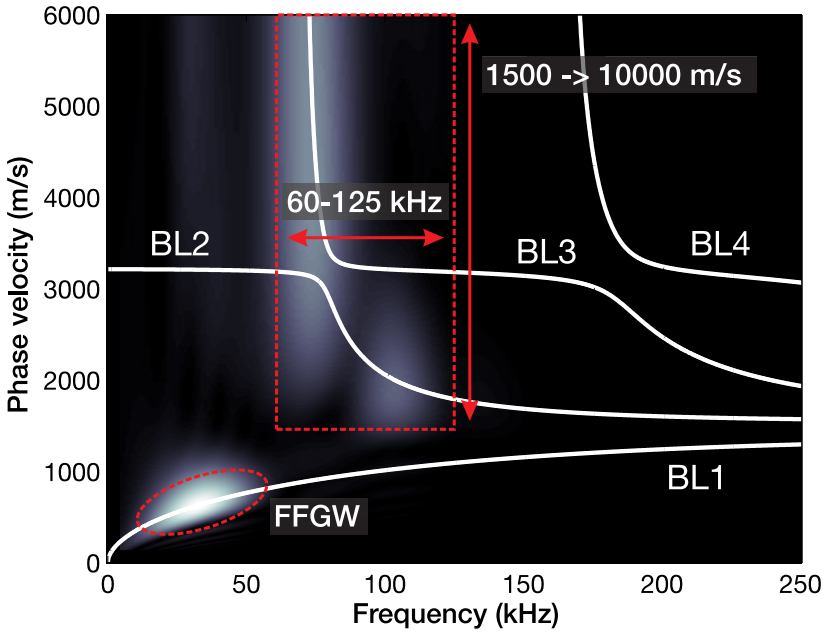

FIGURE 29 2D-FFT mode map of a recorded spatio-temporal signal. Regions of interest for identifying the FFGW and interfering modes are displayed. Theoretical predictions are shown by white curves.

5.5.4 Modelling obstruction of wave propagation in the soft coating

Modes interfering with FFGW have been shown to mainly propagate in the soft coating (Moilanen et al., 2008, 2014). It was hypothesized that such a propagation could be obstructed by introducing a localized deformation in the soft coating, e.g. by locally compressing the skin so as to test to what extent a localized indentation of the coating obstructs the formation of interference and consequently improves the SIR ratio of FFGW, the model expressed in section 5.5.3 was utilized. In addition, a localized indentation was introduced in the propagation path of modes between the source and receivers.

Deformation, mimicking the result of a localized compression, was modelled as an indentation of the sine function shape, with a total width of 14 mm. The depth of the indentation (the pek-to-peak amplitude) was altered from 0 mm (no compression) to 7 mm (full cutoff of the layer of soft coating). That layer was assumed to be incompressible, with the material properties of the surrounding fluid remaining constant regardless of the depth of the indentation (fig. 30).

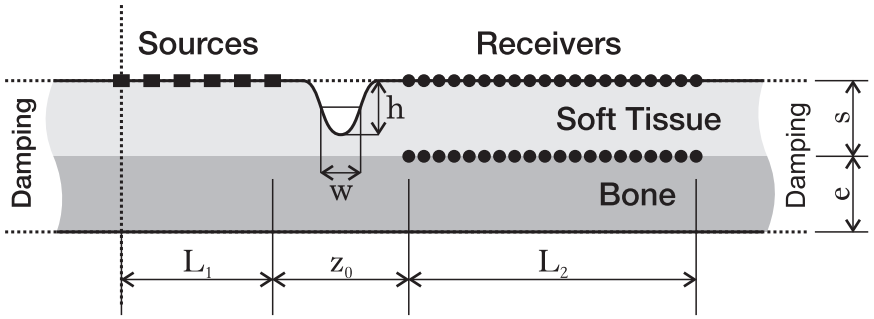

FIGURE 30 Geometry of simulated obstuction of wave propagation. Plate thickness was $e = 3$ mm, thickness of soft coating was $s = 7$ mm, half-width of the deformation was $w = 7$ mm, depth of the deformation was $h = 0$–7 mm, source-receiver separation was $z_0 = 20$ mm and length of the source and receiver arrays were $L_1 = L_2 = 30$ mm.

6 RESULTS

6.1 Clinical studies (first arriving signal)

All of the subjects in the clinical studies were measured with the array probe. Descriptive statistics of the *in vivo* data measured are summarized in table 3. For the purpose of the study (I), the data was divided into two subsets of subjects, premenopausal (starting from 20+ years, n=159) and postmenopausal (n=95) females.

Figure 31 shows the age dependence of V_{FAS} ultrasound data. The curves composed of age-stratified mean values represent an expected pattern of bone growth, peak mass and age-related detoriation. In the radius, V_{FAS} displayed a cleaner age dependence than in the tibia.

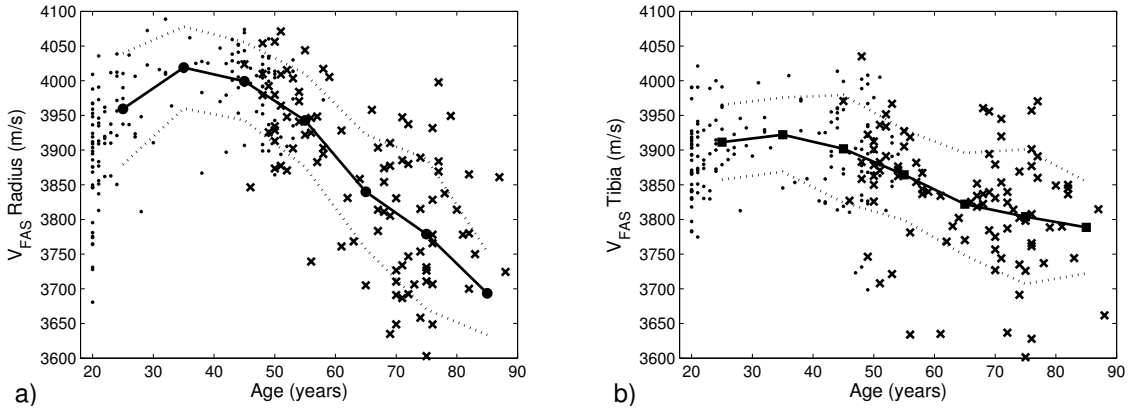

FIGURE 31 V_{FAS} as a function of age for (a) radius and (b) tibia (n=254). Data for premenopausal subjects are displayed by dots and those for postmenopausal ones by cross markers. Solid dotted lines represent age-stratified mean at 10 year intervals and dashed lines represent ± 1 SD.

Figure 32 shows the V_{FAS} data for radius and tibia as a function of the cortical thickness to compression wavelength ratio (e/λ). Compression wavelength

TABLE 3 Descriptive statistics of the *in vivo* data measured (n=254).

	Premenopausal (n = 159)		Postmenopausal (n=95)	
	Average (SD)	Range	Average (SD)	Range
Anthropometric				
Age (y)	34.0 (12.6)	20-58	65.1 (11.3)	45-88
Height (m)	166.2 (5.4)	148-178	161.7 (6.6)	148-179
Weight (kg)	64 (10.5)	45.1-98.8	68.0 (9.8)	45.9-91.9
BMI	23.2 (3.56)	15.9-35.9	26.0 (3.4)	18.4-35.9
Ultrasound				
V_{FAS} Radius (m/s)	3953 (81)	3681-4150	3854 (117)	3583-4071
V_{FAS} Tibia (m/s)	3897 (61)	3698-4035	3829 (88)	3597-4035
pQCT				
Radius BMD (g/cm^3)	962 (61)	733-1095	866 (105)	577-1042
Radius CBMD (g/cm^3)	1216 (23)	1146-1270	1180 (41)	1062-1247
Radius ScBMD (g/cm^3)	882 (139)	353-1201	684 (213)	192-1088
Radius CTh (mm)	2.69 (0.21)	2.01-3.22	2.38 (0.37)	1.52-3.02
Tibia BMD (g/cm^3)	759 (54)	640-884	704 (75)	513-854
Tibia CBMD (g/cm^3)	1144 (18)	1096-1192	1108 (40)	985-1186
Tibia ScBMD (g/cm^3)	416 (106)	192-656	350 (110)	109-605
Tibia CTh (mm)	4.45 (0.46)	3.17-5.89	4.06 (0.55)	2.80-4.91

was determined by assuming 4000 m/s compression velocity at 400 kHz (centre frequency of FAS). It is evident that data is consistent with the theoretical simulation model (Bossy et al., 2002, 2004b). The bias between the *in vivo* data and the prediction is explained mainly by the assumptions made. Scatter in the *in vivo* data is explained by undetermined variability in elastic properties of bone. Nevertheless, it is evident that cortical thickness explains some of the variation in V_{FAS} measurements. In particular, agreement between the experimental data and theoretical prediction with respect to e/λ suggests that the centre frequency of the array probe is optimized for the most dispersive thickness-to-wavelength ratio of V_{FAS}, so as to give an optimal sensitivity to both the cortical thickness and bone elastic properties.

6.1.1 Correlation study

Results of the correlation study confirm the observations made from fig. 32. Figure 33 shows that mineral density of the cortical bone (CMBD) was the best predictor of V_{FAS} ($r^2 = 0.723$, $p < 0.001$) for the radius of postmenopausal females. Cortical thickness still remained a significant predictor of V_{FAS} ($r^2 = 0.579$, $p < 0.001$). Results for the tibia were weaker, but consistent with those for the radius. In particular, higher correlations were obtained for the subset of postmenopausal females than for premenopaual ones. A more complete list of correlations is summarized in table 4. The standard errors of the estimate (SEEs) related to these models and their overall reliability are further discussed in I.

Multivariate linear regression was used to see to what extent a combination of pQCT variables explained V_{FAS}. As seen earlier, CBMD alone was shown to

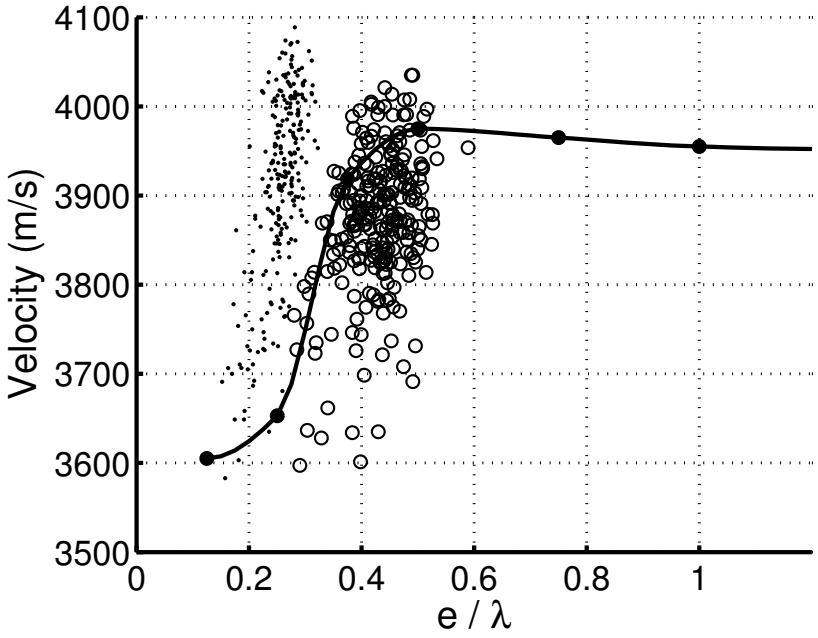

FIGURE 32 Experimental *in vivo* V_{FAS} data (n=254) from the radius (dots) and tibia (circles), together with the results of the 2D simulation model for FAS as a function of cortical thickness to wavelength ratio (after Bossy et al. (2004b)). FAS velocity was calculated for fixed, transversely isotropic elastic coefficients and for a fixed (assumed) f of 400 kHz.

explain 72.3% of the variability of V_{FAS} in postmenopausal women, but using the best additional predictor, ScBMD, the combined predictive power was increased to no more than 73.7%. In the premenopausal group, the best two variable model was also that of CBMD and ScBMD, and including sCBMD over CBMD increased the predictive power of the model from 49.9% to 52.8%. All of the models were highly significant ($p < 0.001$). These results suggest that the pQCT results were inter-correlated, and none of the ultrasound parameters could significantly improve the prediction by CBMD alone.

6.1.2 Fracture study

For the fracture study (II), the data set of postmenopausal females was divided into three subsets according to the history of fractures. There were a total of 47 fractures. The majority of fractures were in the upper extremities (59%), especially in the radius (47%). The fracture group (Fx) consisted of 24 subjects with 32 low energy fractures and the group of other fractures (OF) consisted of 12 subjects with 15 fractures. More than half of the fractures of the OF group were in toes and fingers, and only one radius fracture was recorded. A detailed list can be found in II.

Anthropometric data of the subjects is summarized in table 5. It is worth noting that the low energy fractures group (Fx) had a higher BMI and were older

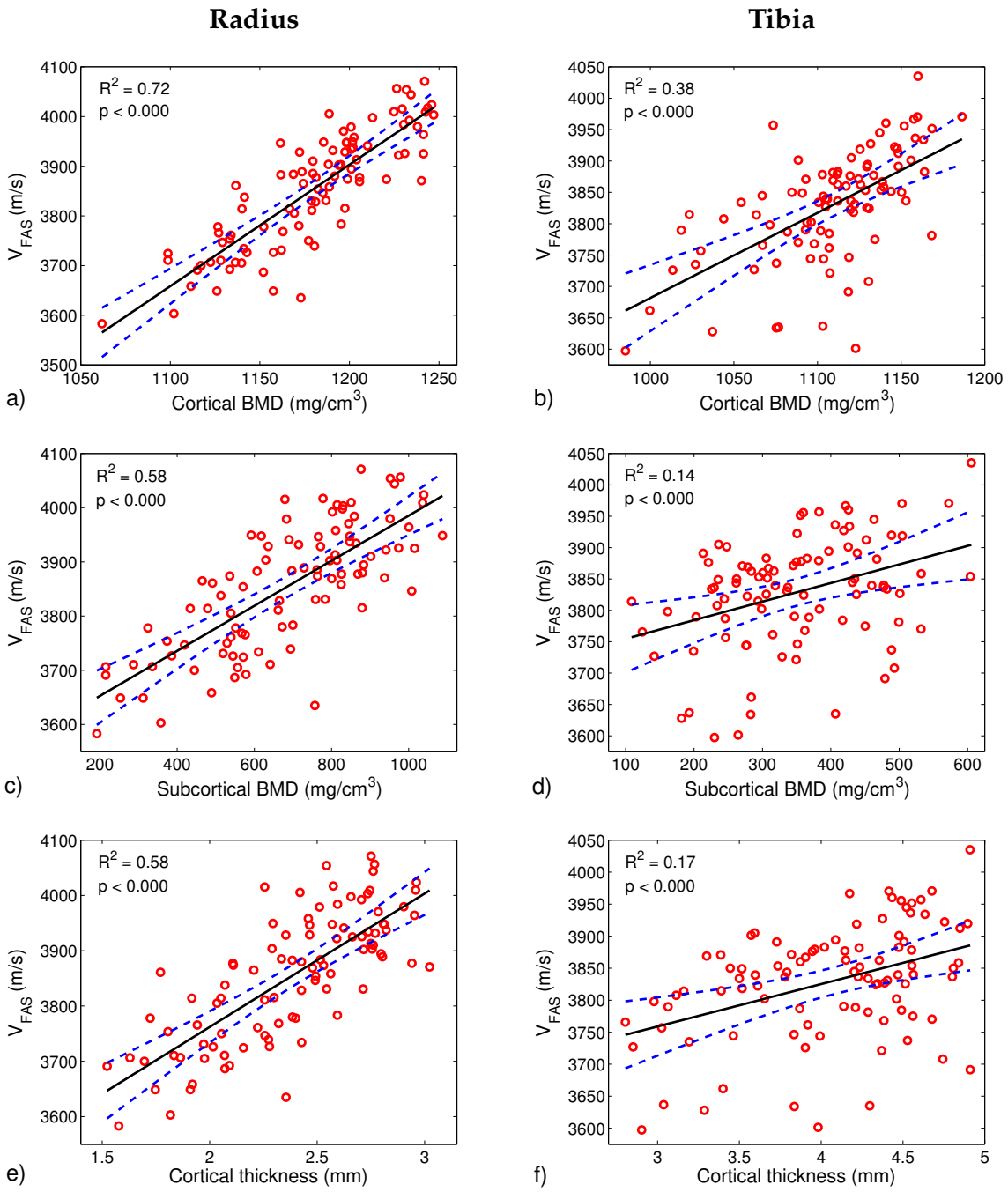

FIGURE 33 Linear regression between V_{FAS} assessment in the radius (left panel) and tibia (right panel) and pQCT CBMD (a,b), ScBMD (c,d) and CTh (e,f). Shown are the results for postmenopausal females (n=95). Dashed lines show a 95% confidence interval for the regression lines.

than the OF and NF groups ($p < 0.05$). There was no significant difference in age, weight, BMI or height between the NF and OF groups.

Overview of V_{FAS}, pQCT and DXA data are shown in table 6. In comparison with the NF group, the Fx group displayed significantly lower values for the radius V_{LF} ($p < 0.001$), CBMD and CTh, and the total BMD, CBMD, ScBMD and

TABLE 4 Correlation coefficients (r^2) between V_{FAS} and pQCT parameters in pre- and postmenopausal women.

	BMD	CBMD	ScBMD	CTh
Premenopausal ($n = 159$)				
V_{FAS} Radius	.163(***)	.499(***)	.081(***)	.102(***)
V_{FAS} Tibia	.038(*)	.176(***)	ns.	ns.
Postmenopausal ($n = 95$)				
V_{FAS} Radius	.621(***)	.723(***)	.576(***)	.579(***)
V_{FAS} Tibia	.235(***)	.377(***)	.135(***)	.171(***)

* $p < 0.05$; ** $p < 0.01$; *** $p < 0.001$

TABLE 5 Anthropometric data of the subjects analyzed for the fracture study (n=89).

	NF (n=53)	Fx (n=24)	OF (n=12)
Age (y)	62.6 (11.8)	70.6 (6.6)[a)]	58.8 (10.4)[b)]
Weight (kg)	67.7 (10.4)	70.4 (9.2)	69.1 (6.9)
Height (cm)	162.6 (5.8)	159.5 (7.2)	163.4 (6.6)
BMI (kg/m^2)	25.6 (3.6)	27.7 (3.0)[c)]	25.9 (2.5)
Age at menopause (years)	48.0 (5.1)	49.9 (6.3)	49.5 (6.0)
Calcium intakes (mg/day)	1081.0 (314.9)	1006.8 (321.0)	1070.8 (393.3)
Vitamin D intakes (μg/day)	7.0 (3.8)	7.4 (4.7)	6.1 (2.5)
Medication, n (%)	24 (45.3)	10 (40.0)	6 (54.5)
Disease, n (%)	6 (11.3)	5 (20.0)	0 (0.0)
Physical activity, n [1)]	4/22/18/9	2/7/11/4	1/2/4/5
Status of osteoporosis, % [2)]			
DXA_{WB}	53/36/11	33/33/33	83/0/17[b)]
DXA_{L2-L4}	62/27/11	38/33/29	67/25/8
DXA_{FN}	62/27/11	33/50/17	33/50/17
DXA_{TF}	55/43/2	38/50/12	59/33/8

Values are given as mean (SD) unless otherwise specified.
NF = non-fracture group, Fx = low energy fracture group, OF = other fractures group
aBMD = areal BMD, WB = whole body, L2–L4 = lumbar vertebrae 2–4, FN = femoral neck, TF = total proximal femur
[1)] physical activity categories: none / about 1h or less / about 2-3h / about 4h or more in a week
[2)] status of osteoporosis categories based on WHO criteria (WHO Scientific Group, 2003): normal / osteopenic / osteoporotic
[a)] $p < 0.01$ in comparison with the NF group, [b)] $p < 0.01$ in comparison with the Fx group, [c)] $p < 0.05$ in comparison with the NF group.

TABLE 6 Descriptive statistics of the fracture study dataset.

	NF (n=53)	Fx (n=24)	OF (n=12)
Ultrasound			
Radius VLF (m/s)	3883 (95)	3783 (100)[a)]	3915 (134)[e)]
Tibia VLF (m/s)	3839 (77)	3791 (99)	3862 (89)
pQCT			
Radius BMD (g/cm^3)	882.9 (86.1)	826.1 (92.3)	913.8 (120.5)[f)]
Radius CBMD (g/cm^3)	1187.9 (33.7)	1157.3 (32.6)[b)]	1202.3 (46.0)[e)]
Radius ScBMD (g/cm^3)	709.1 (185.0)	619.1 (194.4)	781.5 (253.6)[f)]
Radius CTh (mm)	2.46 (0.31)	2.20 (0.34)[b)]	2.54 (0.36)[f)]
Tibia BMD (g/cm^3)	715.4 (62.7)	661.2 (73.3)[a)]	755.2 (64.3)[d)]
Tibia CBMD (g/cm^3)	1114.4 (34.9)	1083.1 (41.8)[b)]	1134.8 (24.9)[d)]
Tibia ScBMD (g/cm^3)	367.4 (94.8)	298.6 (104.0)[c)]	410.9 (113.7)[e)]
Tibia CTh (mm)	4.13 (0.49)	3.80 (0.61)[c)]	4.39 (0.44)[e)]
DXA			
$aBMD_{WB}$ (g/cm^2)	1.155 (0.091)	1.090 (0.127)[c)]	1.150 (0.098)
(T-score)	-0.89 (1.26)	-1.79 (1.76)[c)]	-0.95 (1.36)
$aBMD_{L2-L4}$ (g/cm^2)	1.203 (0.173)	1.116 (0.226)	1.187 (0.167)
(T-score)	-0.57 (1.45)	-1.30 (1.90)	-0.71 (1.40)
$aBMD_{FN}$ (g/cm^2)	0.906 (0.128)	0.840 (0.145)	0.864 (0.108)
(T-score)	-1.21 (0.89)	-1.66 (1.00)	-1.50 (0.75)
$aBMD_{TF}$ (g/cm^2)	0.979 (0.128)	0.911 (0.142)	0.864 (0.130)
(T-score)	-0.85 (0.86)	-1.31 (0.95)	-1.09 (0.87)

Values are given as mean (SD) unless otherwise specified.
NF = non-fracture group, Fx = low energy fracture group, OF = other fractures group
aBMD = areal BMD, WB = whole body, L2–L4 = lumbar vertebrae 2–4, FN = femoral neck, TF = total proximal femur
[a)] $p < 0.001$ in comparison with the NF group, [b)] $p < 0.01$ in comparison with the NF group, [c)] $p < 0.05$ in comparison with the NF group, [d)] $p < 0.001$ on comparison with the Fx group, [e)] $p < 0.01$ in comparison with the Fx group, [f)] $p < 0.05$ in comparison with the Fx group

CTh of the tibia.

The V_{LF} odds ratio (OR) for the radius was 2.23 (95% CI 1.42–3.50). After adjusting for the age and BMI, OR remained significant (2.06; 95% CI 1.21–3.50) (table 7). Similar OR values varying between 1.35 and 2.15 were found for the pQCT and DXA results. The highest area under the ROC curve (AUC) was found for the total BMD of the tibia (0.81, 95% CI 0.71–0.90). Nevertheless, there were no significant differences between the measured AUC results, as is illustrated in fig. 34. This figure displays the 1-specificity with respect to sensitivity (true positives as a function of false positives) of radius and tibia V_{FAS}, radius CBMD, tibia ScBMD and total femur aBMD. Performance of the V_{FAS} variables is not significantly different from those of either the pQCT or DXA variables in this regard.

TABLE 7 Odds ratios (OR) and areas under the receiver operating characteristic curve (AUC) for ultrasound, pQCT and DXA measurements.

	OR (95% CI)	Nagelkerke R^2	AUC (95% CI)
Radius			
V_{FAS}	2.06 (1.21 - 3.50) [b)]	34%	0.80 (0.71 - 0.90) [a)]
BMD	1.28 (0.89 - 1.83) n.s.	24%	0.76 (0.65 - 0.86) [a)]
$CBMD$	1.54 (1.04 - 2.28) [c)]	29%	0.79 (0.69 - 0.89) [a)]
$ScBMD$	1.14 (0.77 - 1.69) n.s	22%	0.74 (0.63 - 0.85) [a)]
CTh	1.51 (1.05 - 2.18) [c)]	30%	0.78 (0.68 - 0.89) [a)]
Tibia			
V_{FAS}	1.22 (0.91 - 1.65) n.s.	24%	0.77 (0.67 - 0.88) [a)]
BMD	1.85 (1.12 - 3.08) [c)]	31%	0.81 (0.71 - 0.90) [a)]
$CBMD$	1.35 (1.03 - 1.76) [c)]	30%	0.80 (0.71 - 0.90) [a)]
$ScBMD$	2.15 (1.08 - 4.29) [c)]	30%	0.79 (0.68 - 0.89) [a)]
CTh	1.58 (0.97 - 2.58) n.s.	27%	0.77 (0.67 - 0.88) [a)]
DXA			
$aBMD_{WB}$	1.64 (1.02 - 2.64) [c)]	29%	0.78 (0.67 - 0.89) [a)]
$aBMD_{L2-L4}$	1.40 (0.97 - 2.03) n.s.	27%	0.79 (0.68 - 0.89) [a)]
$aBMD_{FN}$	1.52 (0.81 - 2.84) n.s.	24%	0.75 (0.65 - 0.86) [a)]
$aBMD_{TF}$	1.72 (0.87 - 3.43) n.s.	26%	0.77 (0.67 - 0.88) [a)]

Reference category is non-fractured.

NF = non-fracture group, Fx = low-energy fracture group, OF = other fractures group

CI = confidence interval, aBMD = areal BMD, WB = whole body, L2–L4 = lumbar vertebrae 2–4, FN = femoral neck, TF = total proximal femur

[a)] $p < 0.001$, [b)] $p < 0.01$, [c)] $p < 0.05$, n.s. = not significant.

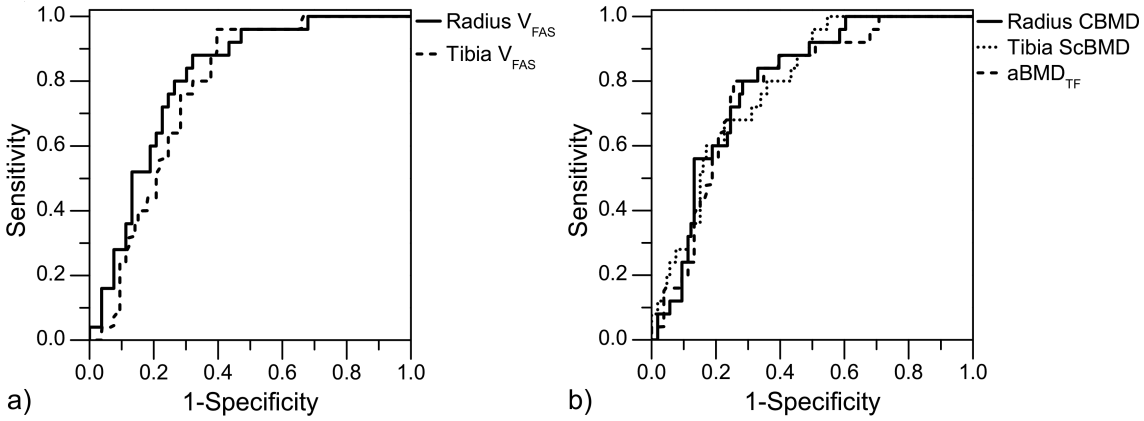

FIGURE 34 Receiver operating characteristic curves showing V_{FAS} in the radius and tibia (a), and radius CBMD, tibia ScBMD (from pQCT) and total femur aBMD (from DXA) versus categorization into the low-energy fracture (FX) group (b). Performance of V_{FAS} variables is not significantly different from those of the pQCT and DXA variables.

6.2 Detection of the fundamental flexural guided wave by an array transducer

6.2.1 Simulation results

Group velocity of signals simulated in uncoated and coated (polyurethane) acrylic and bone plates is shown in fig. 35. The group velocity of FFGW in uncoated plates was in excellent agreement with theoretical prediction (A0), while the results for coated plates exhibited a somewhat bigger deviation from that of the related prediction model (BL1). For free plates, the RMS deviation of the group velocities with respect to prediction were 23.1 m/s for acrylic and 22.6 m/s for bone material. They increased to 48.1 m/s and 41.7 m/s, respectively, for polyurethane-coated plates. The spatial sampling interval for all these results was limited to 6 source-receiver distances.

6.2.2 Experimental results

The method of group velocity assessment was also tested by experimental measurements. In phantom measurements with our earlier scanning ultrasound device, the FFGW data was in good agreement with prediction by the A0 mode. Reduction of the number of source-receiver distances (from 40 to 6) did not significantly affect velocity determination (fig. 36a). Phantom results recorded by the new array probe were compared to the BL1 prediction, as the frame material of the probe (polyurethane) forms a bilayer system with the plate (fig. 36b).

For human radius specimens, group velocity was analyzed from measurements by the scanning ultrasound device, where the number of source-receiver distances was limited (6) to mimic the array probe. Group velocity correlated

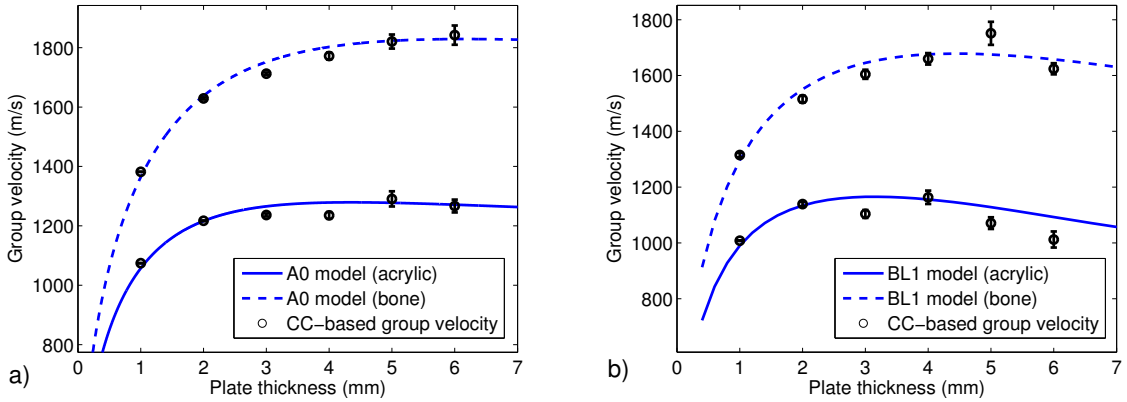

FIGURE 35 Group velocities of FFGW waveforms determined by the CC and GF methods from simulated ultrasound signals propagating in plates. Results are shown for (a) uncoated and (b) coated (9 mm of polyurethane) bone (upper curve) and acrylic (lower curve) plates (1–6 mm thick) at a frequency of 120 kHz.

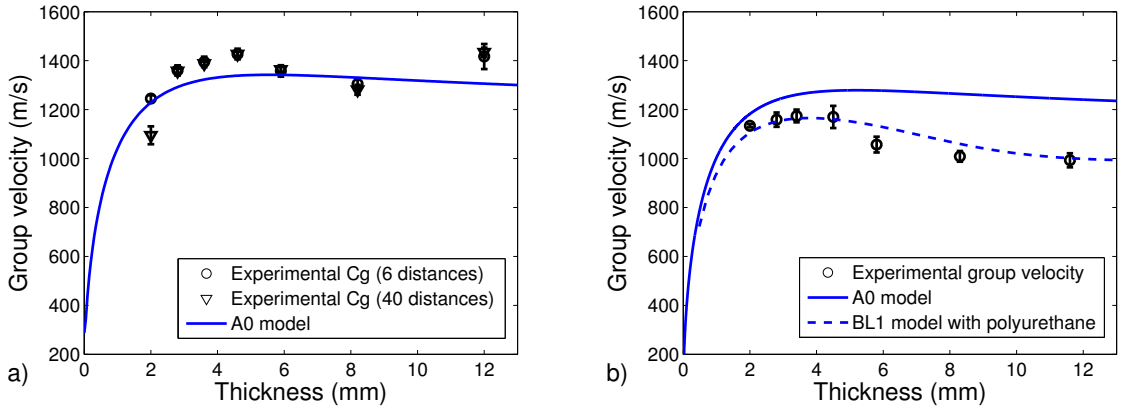

FIGURE 36 Experimental group velocity extracted by the cc method in acrylic plates. Signal souce is (a) the scanning ultrasound device and (b) the array probe. For the scanning ultrasound device, spatial resolution of the response waveforms was reduced to six source-receiver distances so as to mimic that of the array probe, but results for 40 source-receiver distances are also included. Theoretical dispersion curves for the a) A0 mode and b) A0 (upper curve) and BL1 (lower curve) modes are shown for comparison.

moderately ($r^2 = 0.51$, $p < 0.001$, n=39) with the cortical thickness determined by pQCT (fig. 37).

6.2.3 Comparison between CC and GF methods

We evaluated whether the CC based FFGW extraction yields consistent results with that used before (the GF method). Phase velocity was determined by 2D-

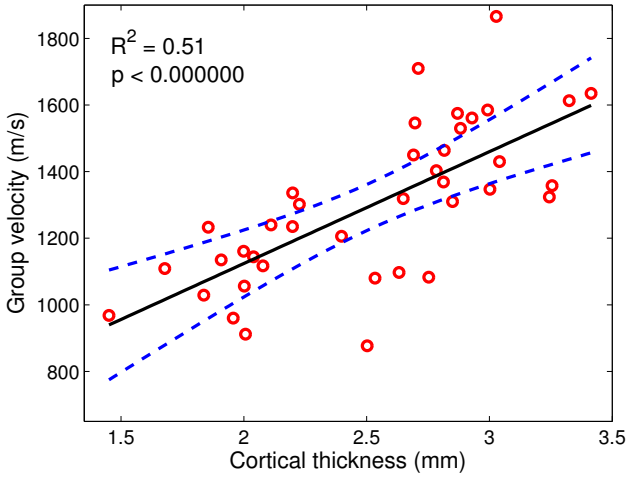

FIGURE 37 Group velocity correlated with cortical thickness in the FFGW waveforms determined by the CC method for *in vitro* measurements from human radii (n=39). Measurements had a limited spatial sampling resolution of 6 distances.

TABLE 8 Root mean square errors (m/s) for phase velocities of the FFGW waveforms determined by the CC and GF methods from simulated ultrasound signals propagating in uncoated and coated plates.

Plate geometry	CC method	GF method
Acrylic layer	8.4 ± 3.6	6.9 ± 2.7
Coated acrylic layer	15.1 ± 6.5	18.9 ± 7.9
Bone material layer	22.6 ± 7.3	16.3 ± 6.0
Coated bone material layer	55.5 ± 8.9	61.7 ± 24.4

FFT from waveforms recorded in simulations with a sufficient spatial sampling interval and processed by GF and CC methods. These results were excluded from III.

Results, together with the semianalytical prediction are shown in fig. 38. Agreement is excellent for the results of both uncoated (A0 prediction) and coated plates (BL1 prediction), and for both bone and acrylic materials. In particular, an automatic mode separation in the CC method exhibited consistent results with manually tuned separation in the GF method. Thus the CC based method is capable of extracting the FFGW phase velocity from simulated measurement signals. The RMSE errors of both mode separation methods against the theoretical curves are summarized in table 8.

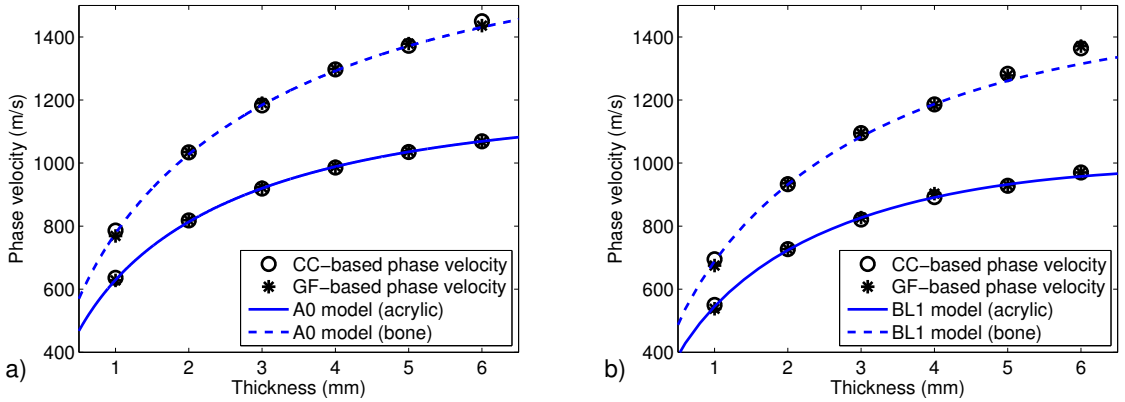

FIGURE 38 Phase velocities of FFGW waveforms determined by the CC and GF methods from simulated ultrasound signals propagating in plates. Results are shown for (a) uncoated and (b) coated (9 mm of polyurethane) bone (upper curve) and acrylic (lower curve) plates of varying thickness at a frequency of 120 kHz.

6.3 Tailored excitation: phase-delayed array

6.3.1 Observations from phase-delayed excitation

Figures 39 and 40 show both RT diagrams and the related 2D-FFTs for (group velocity filtered) simulated signals recorded from the surface of soft coating in a coated (7 mm) plate (3 mm). Figures (a) show results for a traditional excitation (with a single source) and figures (b) show related results for a phase-delayed excitation optimized by SIR. It is evident from fig. 39 and fig. 40b that it is very hard to observe FFGW for a traditional excitation, but that a phase-delayed excitation allows an easy identification of the FFGW mode.

6.3.2 Tuning of a phase-delayed excitation

Herein tuning of a phase-delayed excitation simply means selecting the phase delay parameter with respect to a specifically chosen criteria. An example of this is seen in fig. 41a, wherein magnitudes of FFGW and of the interference modes, simulated in a 3 mm plate with 7 mm soft coating, are displayed as a function of phase delay. The number of transmitter elements used was 6. Position of the observed maximum of FFGW magnitude was 8.2 ± 0.2 μs, which is close to the value predicted by a related semianalytical model (8.65 μs at 40 kHz). Maximum of SIR (and minimum of interference modes) was slightly off the FFGW maximum at 8.4 μs (fig. 41a).

Position of the FFGW maximum fluctuated around the semianalytical values by 0.9 ± 0.8 μs, for plates of 2–6 mm thickness. This suggests, that the maximum of FFGW magnitude was close to the predicted value and that the phase-

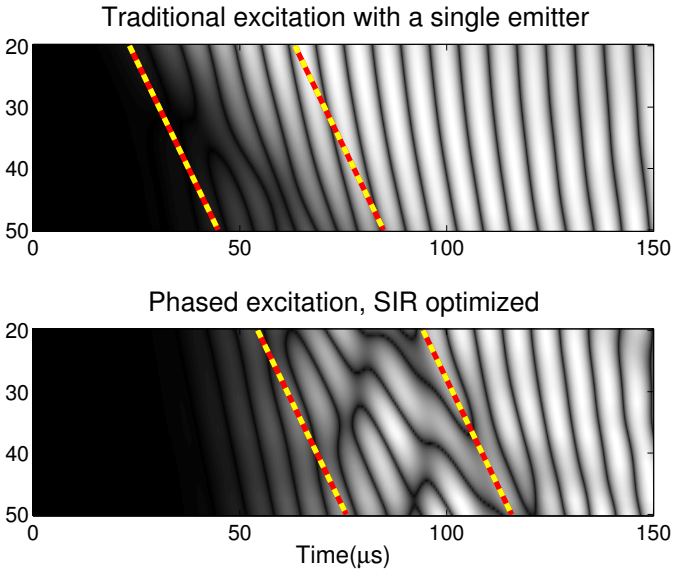

FIGURE 39 RT diagrams for a traditional excitation by a single emitter (top) and by phase-delayed excitation, tuned by maximizing SIR, with six emitters (bottom). Results are from simulations for a 3 mm plate with a 7 mm soft coating. Dashed lines show the region of interest which contains the FFGW wave front.

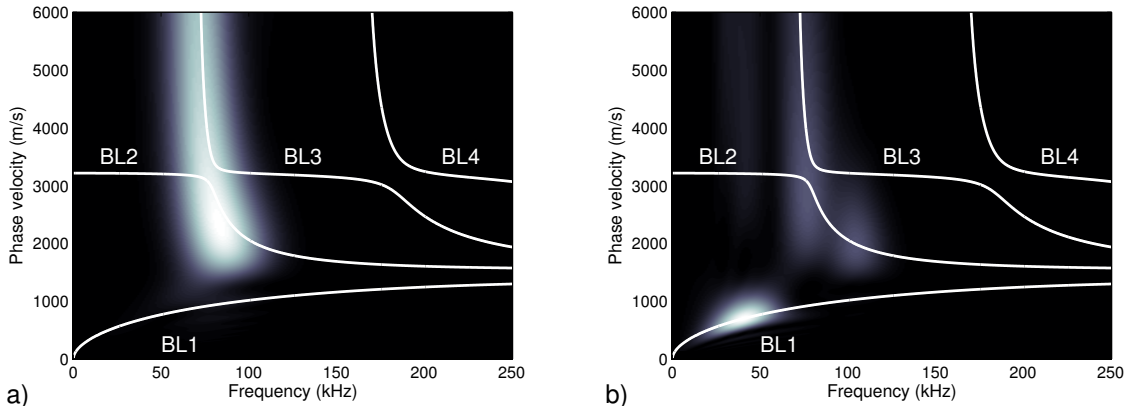

FIGURE 40 2D-FFT diagrams for (a) a traditional single-emitter excitation and (b) a phase-delayed excitation by six emitters, tuned by maximizing SIR. Results are from simulations for a 3 mm plate with a 7 mm soft coating. Bright intensity maxima correspond to detected guided modes. Theoretical predicted branches of guided wave modes are shown by solid lines.

delayed scheme of excitation worked as expected.

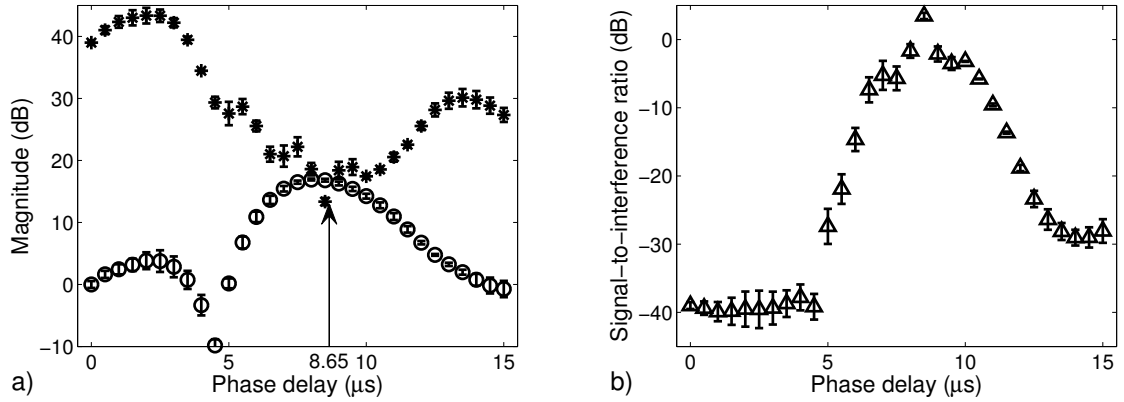

FIGURE 41 (a) Magnitudes of FFGW (open circles) and interference modes (stars), with respect to that of FFGW for zero delay, and (b) the signal-to-interfence ratio for FFGW as a function of phase delay in a 3 mm plate with a 7 mm soft coating. Arrow indicates the theoretically predicted value for the time delay which provides the maximal magnitude for FFGW.

6.3.3 Efficiency of a phase-delayed excitation as a function of the number of transmitter elements

We also investigated the effect of the number of emitters in the transmitter array on the efficiency of phase-delayed excitation, characterized by SIR and the magnitudes of FFGW and interference modes. The average magnitudes and SIRs as functions of the number of emitters, for plate thicknesses of 2–6 mm are visualized in fig. 42. These results illustrate that when the phase delay parameter was tuned by maximizing the FFGW intensity, the magnitude of interference was largely unaffected. As a consequence, SIR increased with the number of emitters. The gain in FFGW magnitude, averaged over all simulated plate thicknesses was 5.8 ± 0.5 dB$/2^N$ for each doubling of the number of emitters. As such, the average total gain was 14.9 ± 1.6 dB. In the same situation, the rate of SIR increase closely followed that of FFGW, being 6.2 ± 2.0 dB$/2^N$ for a total SIR gain of 18.4 ± 5.6 dB. Despite being superficially unaffected by the number of emitters, interference mode magnitude exhibited random fluctuations, resulting in large error bars and a large uncertainty in the SIR gain over the measurement range.

When the phase-delayed excitation (phase delay parameter) was tuned by maximizing SIR, best results were obtained when the magnitude of the interference modes was minimized. Increase of FFGW magnitude closely followed the results for tuning by FFGW magnitde, but the intensity of interference modes decreased significantly for two emitters and then closely followed the magnitude of FFGW. As a result, SIR did not improve as a function of the number of emitters after having a second emitter (fig. 43). Fluctuations in the interference magnitude inflated again the error bars in the SIR data.

On average, the FFGW gain, when maximizing SIR, was 5.6 ± 0.6 dB$/2^N$. As in this case interference modes were effectifely reduced by the phase-delayed

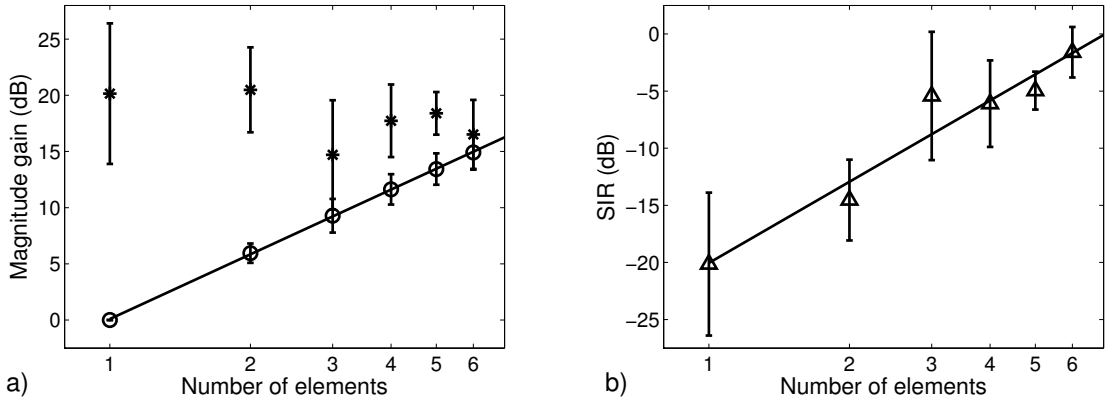

FIGURE 42 Results for a phase-delayed excitation tuned by maximizing the magnitude of FFGW, as a function of the number of emitters in the array transmitter. The magnitudes of FFGW (open circles) and interference modes (stars) are shown in (a) and the SIR of FFGW in (b). Results are averages over a 2–6 mm range of plate thickness (coating thickness 7 mm), and error bars represent one standard deviation. Solid curves are fits made by a linear regression to the data points. The one-emitter result represents a traditional, single emitter excitation.

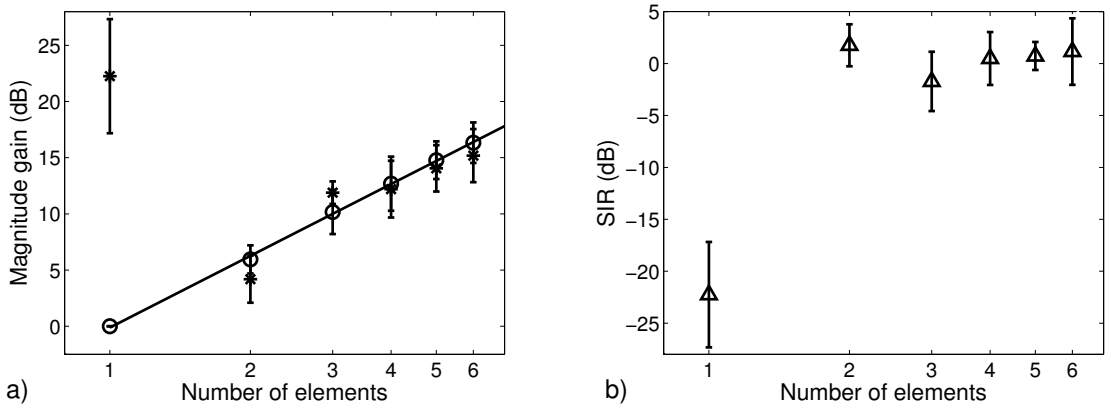

FIGURE 43 Results for a phase-delayed excitation tuned by maximizing SIR, as a function of the number of emitters in the array transmitter. The magnitudes of FFGW (open circles) and interference modes (stars) are shown in (a) and the SIR of FFGW in (b). Results are averages over a 2–6 mm range of plate thickness (coating thickness 7 mm) and error bars represent one standard deviation. Solid lines are fits made by a linear regression to the data points. The one-emitter result represents a traditional, single emitter excitation.

excitation, the SIR gain plateaued at 22.7 ± 5.3 dB, independent of the number emitters.

Results are reported in more detail in IV.

6.4 Obstruction of wave propagation

Obstuction of wave propagation in the soft coating was evaluated in a 3 mm plate of bone material with a 7 mm coating, which featured a localized indentation between the source and receivers.

Figure 44 shows results for a traditional excitation (a single source) when the depth of indentation was gradually increased. According to expectations, FFGW magnitude was largely unaffected by deformation (1.7 dB peak-to-peak fluctuation). Magnitude of interference modes decreased as a function of indentation depth, until reaching a plateau close to 4/7 of the maximum indentation. Even a full indentation (cutoff) of the layer of soft tissue did not further increase SIR. The total SIR gain achieved by locally deforming the soft coating was 20.3 ± 2.3 dB, while a 50% deformation provided 18.3 ± 2.7 dB.

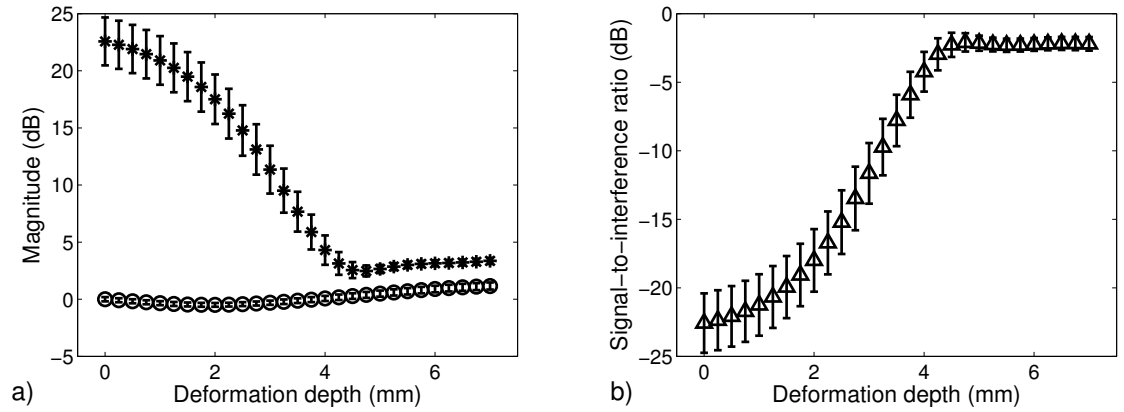

FIGURE 44 Results of localized deformation in the coating using a traditional excitation in a 3 mm plate with a 7 mm soft coating. Shown are (a) the magnitude of FFGW (circles) and interference modes (stars) and (b) related SIR as a function of deformation depth.

A phase-delayed excitation scheme (6-element array) with 50% deformation, displayed as a function of the phase delay parameter, is shown in fig. 45. The shape of the curve is almost identical to the case without obstruction by indentation (fig. 41). SIR was clearly increased by obstuction of the interference modes, although the magnitude of FFGW was essentially unaltered. The maximum of FFGW magnitude was found at 8.0 ± 0.5 μs (at 45 kHz), consistent with the theoretically predicted value (8.2 μs). Unlike the unobstructed case, also SIR had its maximum at the same delay, which indicates that in this case, the phase delay parameter was optimally tuned. The maximal SIR obtained was approximately 8.8 ± 1.3 dB.

Comparing this result with the case of only using a phased excitation, tuned by maximization of the FFGW magnitude, adding a localized indentation resulted in an additional 10.5 ± 1.7 dB gain in SIR. Alternatively, when phase-delayed excitation was tuned by SIR maximization, addition of localized inden-

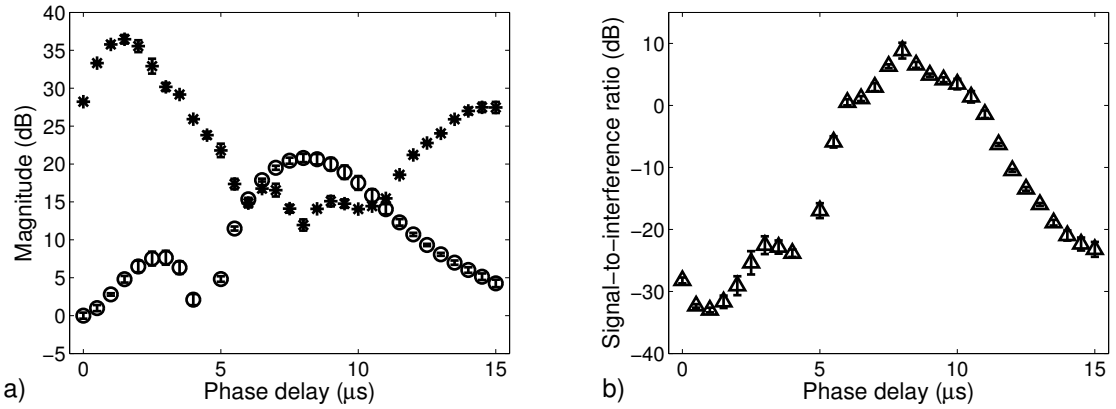

FIGURE 45 Results of the combination of a localized deformation in the coating and a phase-delayed excitation in a 3 mm plate with a 7 mm soft coating. Shown are the magnitude of FFGW (circles) and interference modes (stars) (a) and related SIR (b) as a function of the phase delay parameter.

tation resulted in a 5.4 ± 1.4 dB gain in SIR. The total SIR gain achieved by phase-delayed excitation combined with localized indentation of soft coating was 31.4 ± 2.6 dB.

7 DISCUSSION

A new array transducer was introduced in this study for low frequency ultrasound (f = 50–400 kHz) axial transmission measurements in the human radius and tibia. This new transducer was based on a scanning ultrasound device, developed earlier by our group for measuring two ultrasound modes, FAS and FFGW (Moilanen et al., 2003; Moilanen, 2004). The purpose of the new probe was to enable a rapid and reproducible *in vivo* assessment. Development of the probe was divided into two phases in terms of FAS and FFGW, because of different design requirements for measuring these two modes. We were ready to optimize the design for an *in vivo* assessment of FAS, and the first half of the Thesis included a performance analysis of the array probe. The second half of the Thesis focused on technical challenges related to an *in vivo* assessment of FFGW. Methods of improved signal processing and reduction of the interfering impact of the embracing soft tissue were modelled by computer simulations. Results of this Thesis should permit optimization of the array probe for a simultaneous *in vivo* assessment of FAS and FFGW.

7.1 Clinical studies (first arriving signal)

It was shown that the centre frequency of FAS (400 kHz) measurement, determined by the frequency band of the array probe, was consistent with the most dispersive (*i.e.* thickness sensitive) region of the V_{FAS} velocity in the radius and tibia. While it is known from earlier studies, both *in vitro* (Raum et al., 2005; Muller et al., 2005) and *in vivo* (Prevrhal et al., 2001; Moilanen et al., 2003) that V_{FAS} is determined by the combination of elastic properties and thickness of cortical bone, one can consider that the new array probe was tuned for maximal sensitivity to both of these two bone properties. In particular, the wavelength (8–10 mm) was sufficient for detection of material properties of also the endosteal layer at which osteoporotic resorption is known to begin. Thereby, the array probe is expected to have been tuned for an optimal sensitivity to osteoporotic changes in

particular.

Results of the correlation study (I) confirmed, to some extent, these predictions on the sensitivity of V_{FAS} measurement. In the radius, cortical BMD (indicative of the material properties) was the best predictor ($r^2 = 0.72$) of the variability in V_{FAS} data, while subcortical BMD (indicative of the material properties of endosteal layer) and cortical thickness alone remained significant predictors as well ($r^2 = 0.62$ and $r^2 = 0.58$, respectively). For the tibia the results were consistent, but weaker than those for the radius. It is interesting that multivariate regression did not result a model where V_{FAS} would have been explained by a combination of the bone properties. This is explained by the high covariance between the pQCT based estimates of real bone properties and can be regarded as a limitation of the study. Nevertheless, our findings support the assumption of a multi-parametric sensitivity of V_{FAS}.

To our knowledge, Publication (I) was the first *in vivo* study which analysed correlations between AT QUS and pQCT parameters in the radius. Related *in vitro* studies (Muller et al., 2005; Bossy et al., 2004c; Raum et al., 2005) have shown consistent but weaker correlations, assessed with a 1 MHz AT QUS. Increased correlations in our study may be explained by a lower centre frequency (400 kHz) and larger sample size measured. In the tibia, there are a few *in vivo* studies that have reported correlations consistent with those presented in our study (Prevrhal et al., 2001), with some of them reporting significant correlations only with CBMD (Sievänen et al., 2001; Moilanen et al., 2003). In particular, comparison against the study of Prevrhal et al. (2001) is interesting as they used a former 250 kHz AT QUS ultrasonometer (SoundScan, Myriad). The study in question reported correlations of $r^2 = 0.38$ with CTh and $r^2 = 0.44$ with CBMD, while our array probe reached approximately the same correlation with CBMD ($r^2 = 0.38$), but was not strongly correlated with cortical thickness ($r^2 = 0.17$).

Repeatability of V_{FAS} assessment by the array probe, characterized by CV_{RMS} (0.5%), was significantly improved in comparison with that typical of our earlier scanning ultrasound setup (0.9–1.1% by Moilanen et al. (2003), albeit without bidirectional scanning, or 2.2–2.9% by Määttä (2009)). A value of 0.5% is consistent to approximately 20 m/s uncertainty in the velocity of V_{FAS}, which can be regarded relatively good. Other groups have reported CV_{RMS} values of 0.25–0.90% (tibia, SoundScan) (Foldes et al., 1995; Stegman et al., 1995) and 0.2–0.55% (radius/tibia/phalanges, Omnisense) (Barkmann et al., 2000; Knapp et al., 2004; Weiss et al., 2000) for AT ultrasound devices. Our result is within these ranges.

So as to compare repeatability error with respect to the dynamic range of *in vivo* QUS data, we assessed standardized CV (SCV). Our SCV results (5.9% for the radius and 9.8% for the tibia) showed that the repeatability error was an order of magnitude smaller than the dynamic range of the V_{FAS} data, which suggests that the measurement is able to differentiate subjects. On the other hand, these SCV values were somewhat higher than those reported in the literature for other AT QUS devices, e.g. 1.01% (radius,tibia) for Sunlight Omnisense (Hans et al., 1999), 1.61% for Myriad SoundScan (Foldes et al., 1995) and 4.4–6.6% for our earlier scanning ultrasound device in the tibia (Määttä, 2009; Määttä et al., 2014).

Nevertheless, direct comparison of these results is difficult as SCV is sensitive to determination of the dynamic range, which is inconsistent between the studies. For instance, in Määttä's study the range was characterized by the standard deviation of V_{FAS} data in a population of elderly subjects, which was approximately twice as wide as that typical of younger individuals. By definition, the range should be based on the standard deviation of the population, *i.e.* on the standard deviation of young healthy adults. Yet, the reference group of young healthy adults may have been biased in our study by a low number of subjects (n=34). The reference standard deviations were approximately 2/3 of those reported elsewhere for AT QUS ultrasonometers.

In particular, the population standard deviation for V_{FAS} in the tibia ($SD = 46$ m/s) was smaller than that in the radius ($SD = 80$ m/s). This difference can explain the poorer sensitivity of the tibia results in comparison to those of the radius. The difference in sensitivity of the results, on the other hand, could be up to anatomical features of the tibia and radius. Radius is a smaller bone than the tibia, and the e/λ ratio was respectively smaller in the radius than in the tibia, allowing a better sensitivity of FAS to BMD and cortical thickness because of a deeper penetration of ultrasound. In particular, in the tibia the ultrasound probe was positioned (fig. 18) along the anterior ridge of the bone. The shape of tibia in this region is irregular and the cortical thickness is not well defined (see Moilanen et al. (2004)). Moreover, BMD of the anterior ridge may not represent differences between individuals at a similar rate as other, e.g. medial or lateral sides of the tibia shaft. The cross section of the radius had a relatively regular shape at the measurement site allowing for better definition of bone properties reflected by QUS measurement. Moreover, radius as a non-weight-bearing bone has been acknowledged as a good bone site for predicting peripheral fractures (Hans et al., 2003; Knapp et al., 2004; Nguyen et al., 2004; Talmant et al., 2009).

One may consider as a limitation of our *in vivo* studies that probe positioning was based on a stationary protocol with the proper positioning judged by the operator. This approach differs from the so-called "clinical protocol" suggested by other groups for improving the operator independence. In this latter approach, probe is scanned sideways back and forth across the correct tangential position, and inclusion of correct data is based on a statistical judgement (Weiss et al., 2000). In our approach, positioning was judged from the screen by observing the response waveforms, V_{FAS} and precision error characteristic of a linear regression of the time of flight with respect to distance data. Moreover, statistical methods were used to evaluate the consistency of rapidly repeated measurements to determine exclusion of outlier readings. We argue that a long wavelength (8–10 mm) made our approach not so sensitive to exact positioning of the probe, and the adopted protocol resulted in data, which featured a reproducibility comparable with those of 1 MHz ultrasonometers and sideways scanning.

In II, radius V_{FAS} discriminated subjects with a history of low impact fractures from those without retrospective fractures, based on OR (2.1) and AUC (0.8) (section 6.1.2). These results are in line with those reported in other studies. For instance, for ultrasonic fracture discrimination in female subjects, ORs of 1.69

(Myriad SoundScan, tibia, n=157 (Stegman et al., 1995)), 1.75–2.23 (Sunlight Omnisense, phalanx/radius/tibia, n=549 (Nguyen et al., 2004)), 1.47–2.69 (Sunlight Omnisense, phalanx/radius/tibia, n=323 (Damilakis et al., 2003)) and 1.81 (Bidirectional ultrasonometer, radius, n=166 (Talmant et al., 2009)) have been reported. The AUCs of these studies were between 0.66–0.77, which is slightly less than the AUC of V_{FAS} in our study, but mostly within its error bounds. This suggests that at an individual level, the array probe was equal or slightly better in predicting fractures than the existing devices.

In our study, V_{FAS} in the radius had the second highest discrimination capability of fractures, in comparison with any DXA or pQCT parameters measured, with the subcortical BMD having a slightly larger OR (2.2). In particular, V_{FAS} was the only parameter for which OR remained highly statistically significant ($p < 0.01$), with the BMD variables only being significant at the $p < 0.05$ level. This OR result suggests that at a population level the V_{FAS} measurement has a higher probability compared to any other parameters investigated to end up with a correct discrimination of the fracture status. On the other hand, the AUC results did not display significant differences between the methods, which suggests that QUS cannot improve the reliability of prediction at an individual level. Indeed, QUS in the radius featured a better fracture discrimination than that in the tibia, consistent with interpretation of the correlation results. Given a similar performance with the present gold standard (DXA), V_{FAS} could be suitable for screening. We also used our data to analyse to what extent V_{FAS} in the radius predicted correctly the diagnosis based on DXA (results were not published), and this resulted in very high AUCs with respect to the whole body (0.94, $p < 0.001$), femoral neck (0.85, $p < 0.001$) and lumbar spine (0.80, $p < 0.001$) T-scores (the data were divided into subsets of osteoporotic and healthy subjects using the T-score <= -2.5 as the threshold for osteoporosis). This result supports the objective of using QUS for screening.

It would not be an easy task to compete by QUS with diagnosis. While the present study analysed discrimination of fractures retrospectively, a large prospective study is needed to assess fracture prediction. Such a study would be heavy as it would require a long follow up and a huge number of subjects so as to have sufficient number of subjects for a proper statistical power in those subsets of subjects, where differences in comparative methods of diagnosis may finally occur. On the other hand, in the light of the present study it may also be the case that V_{FAS} alone may not have a significant diagnostic advantage over DXA. In the contrary, a combination of simultaneously measured QUS parameters (such as FAS and FFGW) may enhance the relevance of QUS based prediction. To this end, research is currently focused on development of multi-mode QUS methods.

7.2 Detection of the fundamental flexural guided wave by an array transducer

As has been mentioned, design requirements were different for the FAS and FFGW assessment. While a FAS wave front was observable as a transient in the time domain, it was hard to detect a FFGW wave packet from interference with other (disturbing) wave modes. Instead, spectral analysis based e.g. on 2D-FFT has been proposed by us for identification of FFGW (Moilanen et al., 2006). For the new array receiver, the Nyqvist-Shannon criterion between the spatial sampling interval and the wavelength of FFGW was however not satisfied, which prevented us from using 2D-FFT. To resolve this limitation, a method of multiridge based analysis (Xu et al., 2010), suitable for an array transducer and based on the crazy climber algorithm, short time Fourier transform (STFT) and linear regression for determining the group velocity of FFGW was employed in (III). As a further objective we attempted to replace temporal, manually tunable gate windowing (group velocity filtering) by an adaptive approach, which used said algorithm for mode extraction and reconstruction. The proposed method was tested by numerical simulations and experiments.

Times of flight, assessed by STFT at known source-receiver distances, are associated with dispersion of group velocity with respect to frequency. One of the most important findings of the study (III) was that an array of 6 receivers was sufficient for group velocity determination. Measurements with 40 and 6 inter-transducer separations did not differ significantly as for accuracy of the group velocity determined (fig. 36a).

It was also observed that the soft frame material (9 mm layer of polyurethane) interfered with the solid waveguide and had to be taken into account in the predictive model. This impact was very similar to that of the soft tissue coating, and was predicted by the same bilayer model. However, the impact of soft tissue was not discussed in III. Evaluation of the combined impact of the soft tissue coating and array probe's frame provides challenges for further research, not yet addressed within the present Thesis.

Relevance of the proposed method of group velocity assessment was also shown by retrospective analysis of earlier *in vitro* QUS experiments, carried out by our scanning AT QUS device in human radii (Muller et al., 2005). Indeed, the newly determined FFGW data displayed significant correlation ($r^2 = 0.51$, $p < 0.001$) with cortical thickness, independent of the number source-receiver distances (6 or 40) used in the assessment. These are somewhat weaker than our best correlations using phase velocity, where correlations of $r^2 = 0.73$ against average CTh and $r^2 = 0.81$ against site-matched CTh have been obtained (Moilanen et al., 2007a). Scatter of individual data points from the regression line can be explained by random uncertainties which arise from the impacts of elastic properties and interference with disturbing ultrasound modes supported by the bone wall. These issues, in relation to phase velocity analysis, have been discussed in detail in Moilanen et al. (2007a,b,c). Ultrasonic interference with disturbing

modes can directly affect determination of the time of flight based on the maximum of the envelope of FFGW wave packet and may thus play an important role in uncertainty of the proposed approach of group velocity assessment.

It was demonstrated in addition that the CC based mode separation followed by reconstruction of the temporal waveform can provide a method of adaptive replacement for the method of group velocity filtering, which requires manually chosen parameters. Simulations in (acrylic and bone material) plates, analysed with a sufficient inter-element separation and 2D-FFT, showed that the CC based method resulted in an exact agreement with the theoretically predicted phase velocity. Moreover, the agreement was good between CC and GF based extraction of the FFGW wave packet. The CC based approach could thus provide an alternative for GF.

Nevertheless, the proposed approach which is based on a combination of methods is relatively complicated, which may limit its suitability in practical applications. There may yet be simpler approaches for the group velocity determination. For instance, suitability of the Hilbert transform might be worth considering.

7.3 Tailored excitation: phase-delayed array

Publications IV and Kilappa et al. (2014b) evaluated new and innovative solutions to problems related to the *in vivo* assessment of FFGW. A real challenge with the *in vivo* assessment of FFGW is related to interference with waves that propagate in the combination of soft tissue coating and bone substrate. It has been discussed that such a bilayer waveguide supports propagation of energetic wave modes that mainly propagate in the soft tissue subsystem and interfere with FFGW (Moilanen et al., 2008, 2014). While FFGW, on the other hand, is rapidly damped by the coating, it is hard to distinguish it from these disturbing modes at the receiver which is placed on top of the soft coating. So as to resolve this challenge, it is necessary to find methods for improving the signal-to-interference ratio (SIR) of FFGW with respect to these disturbing modes.

Study IV showed by numerical simulations that by tailoring the excitation of FFGW it is possible to improve the magnitude and SIR of FFGW at receivers on top of the soft coating. In particular, we considered our 6-transducer array as a phase-delayed array, in which excitation of each transducer is delayed with respect to the previous one.

One of the key predictions by our simulations was that it is possible to automate the tuning of the inter-transducer delay, so as to maximize the magnitude and/or SIR of FFGW. Tuning of the delay parameter requires iteration of the excitation and monitoring its response to FFGW magnitude and SIR. In particular, it was predicted that tuning is a trade-off between the magnitude and SIR, as maximization of FFGW magnitude does not always minimize those of the disturbing modes, and SIR may remain limited. Tuning by SIR maximization, on the other

hand, may be limited by a reduced magnitude of FFGW. Nevertheless, our results predict that by a short array of 2–6 transducers it is possible to tune the source array so as to get a significant gain (15–20 dB) in the SIR of FFGW.

It is a limitation of this study that the performance of the method was evaluated in a simplified geometry of 2D simulations. Although these simulations feature an exact counterpart of a related semianalytical model (Yapura and Kinra, 1995; Moilanen et al., 2006), relevance of the analysis to real geometry of bone remains unexplored. Relevance of such simplified models for FFGW in real bone with tapering (axial direction) and an irregular tubelike cross section have been demonstrated earlier in Moilanen et al. (2007a,b,c, 2008). In the light of these earlier studies, the choice of a simplified geometry in the present work seems appropriate. Nevertheless, 2D simulations were necessary to permit a noticeable number of iterated simulations which, in the chosen form, already required several weeks to compute (with post-processing included).

It is obvious that the relevance of these predictions needs to be shown by further experimental work, which has already been initiated. Preliminary results of a phase-delayed excitation with our array transducer in coated bone-mimicking tubes were consistent with the simulated predictions. The proposed approach thus seems worth continuing. We have also successfully tested a photo-acoustic implementation of the array source, based on an array of laser diodes (Karppinen et al., 2013). Results for coated bone-mimicking tubes were consistent with the simulated predictions (Moilanen et al., 2013b).

Use of a photo-acoustic source provides certain advantages in comparison with traditional contact ultrasound transducers. Contact problems are avoided and the ultrasound source is created inside the tissue, close to the bone. It is important, that by a pulsed optical beam it is also possible to introduce a low-frequency source featuring a small foot print. All of this is essential for the excitation of FFGW. Development in our group is aiming towards a new photo-acoustic implementation of the AT QUS device. Its clinical prototype capable of *in vivo* measurements is now being developed.

7.4 Obstruction of wave propagation

So as to address the limitation of a phase-delayed excitation, related to the fact that the delay parameter cannot (always) be efficiently tuned to reduce the disturbing modes while magnifying FFGW, we proposed in Kilappa et al. (2014b) a supporting method, obstruction of wave propagation by mechanically deforming the soft tissue. This approach was based on assumptions that the unwanted, disturbing modes mainly arise from waves propagating in the soft tissue while, FFGW mainly relates to waves propagating in the solid subsystem. In this case, localized deformation of the soft coating should disturb propagation of the disturbances by reflecting them back to the transmitter side.

The composition of the study was identical to that discussed in section 7.3,

and as such, the same limitations apply. However, simulated predictions were promising, suggesting an additional 10 dB gain in SIR. Such a gain can prove useful in situations where SIR cannot be improved sufficiently with phase-delayed excitation alone, e.g. in the case of a thick coating of soft tissue. The simulations also suggested that a full indentation (cutoff) of the layer of soft tissue is not necessary, and that even a modest indentation is useful. As the soft tissue coating on top of the human radius or tibia is typically easily compressible, this gives hope that the method could be used *in vivo* by deforming the soft tissue by external compression.

8 CONCLUSION

In conclusion, it was shown that the low-frequency axial transmission quantitative ultrasound method (LF AT QUS), implemented with an array transducer, could permit multi-mode *in vivo* assessment of at least two wave modes, the first arriving signal (FAS) and the fundamental flexural guided wave (FFGW), in the human radius or tibia.

The first part of the Thesis showed that FAS is sensitive to clinically relevant properties (bone mineral density and cortical thickness) of the bone and that it can differentiate subjects with fractures from healthy controls consistently with dual-energy X-ray absorptiometry (DXA). It was thus suggested that FAS assessment may permit screening of osteoporotic individuals, prior to diagnosis by DXA. Results of the first part of the Thesis were utilized in the development of a commercial AT QUS ultrasonometer (OsCare Sono).

The second part of the Thesis focused on the remaining challenges of FFGW assessment. A method of signal processing was introduced to enable the detection of FFGW with an array receiver. Moreover, methods of excitation were introduced to enhance separation of FFGW from disturbing wave modes on top of a coating of soft tissue. Within a parallel project, the solutions analyzed in the Thesis are already being implemented in the development of a clinical, multi-mode ultrasonometer.

As FAS and FFGW are sensitive to different parameters of bone, their simultaneous *in vivo* assessment is expected to enhance the relevance of LF AT QUS in comparison with using either of these modes alone, similarly to any set of modes from which multiple different properties could be derived. Due to the advantages such a multi-mode assessment would provide, there is an increasing interest within the community of QUS researchers in shifting the research focus to multi-parametric ultrasound, and furthermore, to the standardization of different QUS approaches. Time will tell whether the next generation QUS becomes competitive with the established clinical standard of diagnosing osteoporosis. Yet, there is a call for a reliable and inexpensive screening, which QUS may well satisfy.

REFERENCES

Albanese, C. V. 2003. Clinical applications of body composition measurements using dxa. J Acoust Soc Am 6 (2), 75–85.

Alleyne, A. D., Teti, A. & Rucci, N. 2012. Bone cells and the mechanisms of bone remodelling. Front Biosci (Elite Ed) 4, 2302–2321.

Alleyne, D. & Cawley, P. 1991. A two-dimensional fourier transform method for the measurement of propagating multimode signals. J Acoust Soc Am 89 (3), 1159–1168.

Alzahouri, K., Bahrami, S., Durand-Zaleski, I., Guillemin, F. & Roux, C. 2013. Cost-effectiveness of osteoporosis treatments in postmenopausal women using frax^{TM} thresholds for decision. Joint Bone Spine 80 (1), 64–69.

Barkmann, R., Kantorovich, E., Singal, C., Hans, D., Genant, H. K., Heller, M. & Glüer, C.-C. 2000. A new method for quantitative ultrasound measurements at multiple skeletal sites. J Clin Densitom 3 (1), 1–7.

Barkmann, R., Laugier, P., Moser, U., Dencks, S., Klausner, M., Padilla, F., Haïat, G. & Glüer, C.-C. 2007. A device for in vivo measurements of quantitative ultrasound variables at the human proximal femur. IEEE Trans Ultrason Ferroelectr Freq Control 122, 1810–1817.

Baron, C., Talmant, M. & Laugier, P. 2007. Effect of porosity on effective diagonal stiffness coefficients (c_ii) and elastic anisotropy of cortical bone at 1 mhz: a finite-difference time domain study. J Acoust Soc Am 122, 1810–1817.

Baroncelli, G. I., Federico, G., Vignolo, M., Valerio, G., del Puente, A., Maghnie, M., Baserga, M., Farello, G. & Saggese, G. 2006. Cross-sectional reference data for phalangeal quantitative ultrasound from early childhood to young-adulthood according to gender, age, skeletal growth, and pubertal development. Bone 39, 159–173.

Beck, T. 2003. Measuring the structural strength of bones with dual-energy x-ray absorptiometry: principles, technical limitations and future possibilities. Osteoporos Int 14 Suppl 5, 81–88.

Black, D. M., Cummings, S. R. & Genant, H. K. 1992. Axial and appendicular bone density predicts fractures in older women. J Bone Miner Res 7, 633–638.

Blake, G. M. & Fogelman, I. 1997. Technical principles of dual energy x-ray absorptiometry. Semin Nucl Med 27 (3), 210–228.

Blake, G. M. & Fogelman, I. 2009. The clinical role of dual energy x-ray absorptiometry. Eur J Radiol 71 (3), 406–414.

Blake, G. M., Naeem, M. & Boutros, M. 2006. Comparison of effective dose to children and adults from dual x-ray absorptiometry examinations. Bone 38 (6), 935–942.

Blake, J. M. & Altman, D. G. 1986. Statistical methods for assessing agreement between two methods of clinical measurement. Lancet 1, 307–310.

Bolotin, H. H. & Sievänen, H. 2001. Inaccuracies inherent in dual-energy x-ray absorptiometry in vivo bone mineral density can seriously mislead diagnostic/prognostic interpretations of patient-specific bone fragility. J Bone Miner Res 16, 799–805.

Bossy, E., Defontaine, M., Patat, F. & Laugier, P. 2004a. Bidirectional axial transmission can improve accuracy and precision of ultrasonic velocity measurement in cortical bone: a validation on test materials. IEEE Trans Ultrason Ferroelectr Freq Control 51 (1), 71–79.

Bossy, E., Talmant, M. & Laugier, P. 2002. Effect of bone cortical thickness on velocity measurements using ultrasound axial transmission: a 2d simulation study. J Acoust Soc Am 112 (1), 297–307.

Bossy, E., Talmant, M. & Laugier, P. 2004b. Three-dimensional simulations of ultrasonic axial transmission velocity measurement on cortical bone models. J Acoust Soc Am 115 (5 Pt 1), 2314–2324.

Bossy, E., Talmant, M., Peyrin, F., Akrout, L., Cloetens, P. & Laugier, P. 2004c. An in vitro study of the ultrasonic axial transmission technique at the radius: 1-mhz velocity measurements are sensitive to both mineralization and intracortical porosity. J Bone Miner Res 19 (9), 1548–56.

Bousson, V., Meunier, A., Bergot, C., Vicaut, E., Rocha, M. A., Morais, M. H., Laval-Jeantet, A. M. & Laredo, J. D. 2001. Distribution of intracortical porosity in human midfemoral cortex by age and gender. J Bone Miner Res 16, 1308–1317.

Bouxein, M. L. 2006. Biomechanics of osteoporotic fractures. Clinical Reviews in Bone and Mineral Metabolism 4 (3), 143–153.

Bréban, S., Padilla, F., Fujisawa, Y., Mano, I., Matsukawa, M., Benhamou, C. L., Otani, T., Laugier, P. & Chappard, C. 2010. Trabecular and cortical bone separately assessed at radius with a new ultrasound device, in a young adult population with various physical activities. Bone 46, 1620–1625.

Buckwalter, J. A., Glimcher, M. J., Cooper, R. R. & Recker, R. 1995. Bone biology. part 1: structure, blood supply, cells, matrix and mineralization. J Bone and Joint Surg 77-A, 1256–1275.

Budhia, S., Mikyas, Y., Tang, M. & Badamgarav, E. 2012. Osteoporotic fractures: a systematic review of u.s. healthcare costs and resource utilization. Pharmacoeconomics 30 (2), 147–170.

Burge, R., Dawson-Hughes, B., Solomon, D. H., Wong, J. B., King, A. & Tosteson, A. 2007. Incidence and economic burden of osteoporosis-related fractures in the united states, 2005-2025. J Bone Miner Res 22 (3), 465–475.

Burr, D. B. 2011. Why bones bend but don't break. J Musculoskelet Neuronal Interact 11 (4), 270–285.

Camus, E., Talmant, M., Berger, G. & Laugier, P. 2000. Analysis of the axial transmission technique for the assessment of skeletal status. J Acoust Soc Am 108 (6), 3058–3065.

Carmona, R. A., Hwang, W. L. & Torrésani, B. 1999. Multiridge detection and time-frequency reconstruction. IEEE Trans Signal Process 47 (2), 480–492.

Chaffai, S., Roberjot, V., Peyrin, F., Berger, G. & Laugier, P. 2000. Frequency dependence of ultrasonic backscattering in cancellous bone: Autocorrelation model and experimental results. J Acoust Soc Am 108, 2403–2411.

Chappard, C., Laugier, P., Fournier, B., Roux, C. & Berger, G. 2012. Assessment of the relationship between broadband ultrasound attenuation and bone mineral density at the calcaneus using bua imaging and dxa. Osteoporos Int 7 (4), 316–322.

Chen, J., Foiret, J., Minonzio, J., Talmant, M., Su, Z., Cheng, L. & Laugier, P. 2012. Measurement of guided mode wavenumbers in soft tissue–bone mimicking phantoms using ultrasonic axial transmission. Phys Med Biol 57, 3025–3037.

Cheng, S., Lyytikäinen, A., Kroger, H., Lamberg-Allardt, C., Alen, M., Koistinen, A. & et al. 2005. Effects of calcium, dairy product, and vitamin d supplementation on bone mass accrual and body composition in 10-12-y-old girls: a 2-y randomized trial. Am J Clin Nutr 82 (1), 1115–1126.

Cheng, S., Volgyi, E., Tylavsky, F. A., Lyytikäinen, A., Törmakangas, T., Xu, L. & et al. 2009. Trait-specific tracking and determinants of body composition: a 7-year follow-up study of pubertal growth in girls. BMC Med 7, 5.

Cohen, G. C. 2001. Higher-order numerical methods for transient wave equations. New York: Springer.

Cohen, L. 1989. Time-frequency distributions – a review. Proceedings of the IEEE 77 (7), 941–981.

Cooper, C., Cole, Z. A., Holroyd, C. R., Earl, S. C., Harvey, N. C., Dennison, E. M., Melton, L. J., Cummings, S. R., Kanis, J. A. & on Fracture Epidemology, I. C. W. G. 2011. Secular trends in the incidence of hip and other osteoporotic fractures. Osteoporos Int 22 (5), 1277–1288.

Cummings, S. R., Bates, D. & Black, D. M. 2002. Clinical use of bone densitometry: scientific review. JAMA 288 (15), 1889–1897.

Cummings, S. R., Browner, W., Black, D., Nevitt, M., Genant, H. K., Cauley, J., Ensrud, K., Scott, J. & T. M. Vogt, M. 1993. Bone density at various sites for prediction of hip fracture. Lancet 341 (9937), 72–75.

Damilakis, J., Abrams, J. E., Guglielmi, G. & Link, T. M. 2010. Radiation exposure in x-ray based imaging techniques used in osteoporosis. Eur Radiol 20, 2707–2714.

Damilakis, J., Papadokostakis, G. & Vrahoriti, H. 2003. Ultrasound velocity through the cortex of phalanges, radius and tibia in normal and osteoporotic postmenopausal women using a new multisite quantitative ultrasound device. Invest Radiol 38 (4), 207–211.

Daubechies, I. 1990. The wavelet transform, time-frequency localization and signal analysis. IEEE Trans Information Theory 36 (5), 961–1005.

Diab, T., Condon, K. E., Burr, D. B. & Vashishth, D. 2006. Age-related change in the damage morphology of human cortical bone and its role in bone fragility. Bone 38 (3), 427–431.

Dodd, S. P., Cunningham, J. L., Miles, A. W., Gheduzzi, S. & Humphrey, V. F. 2006. Ultrasonic propagation in cortical bone mimics. Phys Med Biol 51, 4635–4647.

Drinkwater, B. E. & Wilcox, P. D. 2006. Ultrasonic arrays for non-destructive evaluation: A review. NDT&E international 39, 525–541.

Dubinsky, T. J., Cuevas, C., Dighe, M. K., Kolokythas, O. & Hwang, J. H. 2007. High-intensity focused ultrasound: current potential and oncological applications. Am J Roentgenol 190 (1), 191–199.

Evans, J. A. & Tavakoli, M. B. 1990. Ultrasonic attenuation and velocity in bone. Phys Med Biol 35 (10), 1387–1396.

Fan, X. & Hynynen, K. 1996. A study of various parameters of spherically curved phased arrays for noninvasive ultrasound surgery. Phys Med Biol 41, 591–608.

Foldes, A. J., Rimon, A., Keinan, D. D. & Popovtzer, M. M. 1995. Quantitative ultrasound of the tibia: A novel approach for assessment of bone status. Bone 17 (4), 363–367.

Gazis, D. C. 1958. Three-dimensional investigation of the propagation of waves in hollow circular cylinders i. analytical foundation. J Acoust Soc Am 31, 568–573.

Gilks, W. R., Richardson, S. & eds., D. J. S. 1995. Markov chain monte carlo in practice.

Glüer, C.-C., Eastell, R., Reid, D. M., Felsenberg, D., Roux, C., Barkmann, R., Timm, W., Blenk, T., Armbrecht, G., Stewart, A., Clowes, J., Thomasius, F. E. & Kolta, S. 2004. Association of five quantitative ultrasound devices and bone densitometry with osteoporotic vertebral fractures in a population-based sample: the opus study. J Bone Miner Res 19, 782–792.

Glüer, C.-C. 1997. Quantitative ultrasound techniques for the assessment of osteoporosis: expert agreement on current status. the international quantitative ultrasound consensus group. J Bone Miner Res 12, 1280–1288.

Glüer, C.-C. 2008. A new quality of bone ultrasound research. IEEE Trans Ultrason Ferroelectr Freq Control 55, 1524–1528.

Graff, K. F. 1991. Wave Motion in Elastic Solids. New York: Dover.

Gray, H. 1918. Anatomy of the Human Body, revised and re-edited by Warren H. Lewis (20th edition). Philadelphia: Lea & Febriger.

Griffith, J. F. & Genant, H. K. 2008. Bone mass and architecture determination: state of the art. Best Prac Res Clin Endocrinol Metab 22 (5), 737–764.

Griffith, J. F. & Genant, H. K. 2012. New advances in imaging osteoporosis and its complications. Endocrine 42 (1), 39–51.

Grimal, Q., Rus, G., Parnell, W. J. & Laugier, P. 2011. A two-parameter model of the effective elastic tensor for cortical bone. J Biomech 44, 1621–1625.

Hall, S. 2007. Basic Biomechanics (4th edition). McGraw-Hill Humanities/Social Sciences/Languages.

Hanley, J. A. & McNeil, B. J. 1983. A method of comparing the areas under receiver operating characteristic curves derived from the same cases. Radiology 148, 839–843.

Hans, D., Dargent-Molina, P., Schott, A. M., Sebert, J. L., Cormier, C., Kotzki, P. O., Delmas, P. D., Pouilles, J. M., Breart, G. & Meunier, P. J. 1996. Ultrasonographic heel measurements to predict hip fracture in elderly women: the edipos prospective study. Lancet 348, 511–514.

Hans, D., Genton, L., Allaoua, S., Pichard, C. & Slosman, D. O. 2003. Hip fracture discrimination study: Qus of the radius and the calcaneum. J Clin Densitom 6 (2), 163–172.

Hans, D., Srivastav, S. K., Singal, C., Barkmann, R., Njeh, C. F., Kantorovich, E., Glüer, C.-C. & Genant, H. K. 1999. Does combining the results from multiple bone sites measured by a new quantitative ultrasound device improve discrimination of hip fracture. J Bone Miner Res 14 (4), 644–651.

Haïat, G., Naili, S., Grimal, Q., Talmant, M., Desceliers, C. & Soize, C. 2009. Influence of a gradient of material properties on ultrasonic wave propagation in cortical bone: application to axial transmission. J Acoust Soc Am 125 (6), 4043–4052.

Heaney, R. P., Avioli, L. V., Chesnut, C. H. I., Lappe, J., Recker, R. R. & Brandenburger, G. H. 1995. Ultrasound velocity through bone predicts incident vertebral deformity. J Bone Miner Res 10, 341–345.

Hernandez, C. J. & Keaveny, T. M. 1996. A biomechanical perspective on bone quality. Bone 39, 1173–1181.

Hind, K. & Burros, M. 2006. Weight-bearing exercise and bone mineral accrual in children and adolescents: A review of controlled trials. Bone 40, 14–27.

Hooven, F. H., Adachi, J. D., Adami, S., Boonen, S., Compston, J., Cooper, C., Delmas, P., Diez-Perez, A., Gelback, S., Greenspan, S. L., LaCroix, A., Lindsay, R., Netelenbos, J. C., adn C. Roux, J. P., Saag, K. G., Sambrook, P., Silverman, S., Siris, E., Watts, N. & Jr, F. A. A. 2009. The global longtitudinal study of osteoporosis in women (glow): rationale and study design. Osteoporosis Int 20 (7), 1107–1116.

Hughes, D. E., Dai, A., Tiffee, J. C., Li, H. H., Mundy, G. R. & Boyce, B. F. 1996. Estrogen promotes apoptosis of murine osteoclasts mediated by tgf-β. Nat Med 2, 1132–1136.

Huttunen, T. 2004. The ultra weak variational formulation for ultrasound transmission problems. Doctoral dissertation. University of Kuopio, Department of applied physics. Ph. D. Thesis.

Iwamoto, J., Takeda, T. & Ichimura, S. 2001. Effect of exercise training and detraining on bone mineral density in postmenopausal women with osteoporosis. Orthopaedic Science 6, 128–132.

Jergas, M. & Genant, H. K. 1993. Current methods and recent advances in the diagnosis of osteoporosis. Arthritis Rheum 36 (12), 1649–1662.

Johnell, O. & Kanis, J. A. 2005. Epidemology of osteoporotic fractures. Osteoporos Int 16, S3–S7.

Johnell, O. & Kanis, J. A. 2006. An estimate of the worldwide prevalence and disability associated with osteoporotic fractures. Osteoporos Int 17 (12), 1726–1733.

Kaczmarz, S. 1937. Angenäherte auflösung von systemen linearer gleichungen. Bulletin International de l'Académie Polonaise des Sciences et des Lettres. Classe des Sciences Mathématiques et Naturelles. Série A, Sciences Mathématiques. 35, 355–357.

Kanis, J. A. & Johnell, O. 2005. Requirements for dxa for the management of osteoporosis in europe. Osteoporos Int 16 (3), 229–238.

Kanis, J. A., Oden, A., McCloskey, E. V., Johansson, H., Wahl, D. A., Cooper, C., on Epidemiology, I. W. G. & of Life, Q. 2012. A systematic review of hip fracture incidence and probability of fracture worldwide. Osteoporos Int 23 (9), 2239–2256.

Kannus, P., Niemi, S., Pakkari, J., Palvanen, M., Vuori, I. & Järvinen, M. 2006. Nationwide decline in incidence of hip fracture. J Bone Miner Res 21 (12), 1836–1838.

Karim, M. R., Mal, A. K. & Bar-Cohen, Y. 1990. Inversion of leaky lamb wave data by simplex algorithm. J Acoust Soc Am 88, 482–491.

Karjalainen, J., Riekkinen, O., Töyräs, J., Kröger, H. & Jurvelin, J. 2008. Ultrasonic assessment of cortical bone thickness *in vitro* and *in vivo*. IEEE Trans Ultrason Ferroelec Freq Control 55 (10), 2191–2197.

Karppinen, P., Salmi, A., Moilanen, P., Karppinen, T., Zhao, Z., Myllylä, R., Timonen, J. & Haeggström, E. 2013. Phase-delayed laser diode array allows ultrasonic guided wave mode selection and tuning. J Appl Phys 113 (14), 144904.

Kaufman, J., Luo, G. & Siffert, R. S. 2007. A portable real-time ultrasonic bone densitometer. J Appl Phys 33 (9), 1445–1452.

Keene, G. S., Parker, M. J. & Pryor, G. A. 1993. Mortality and morbidity after hip fractures. BMJ 307, 1248–1250.

Khaw, K. T., Reeve, J., Luben, R., Bingham, S., Welch, A., Warenham, N., Oakes, S. & Day, N. 2004. Prediction of total and hip fracture risk in men and women by quantitative ultrasound of calcaneus: Epic-norfolk prospective population study. Lancet 363, 197–202.

Kilappa, V., Moilanen, P., Salmi, A., Zhao, Z., Haeggström, E., Timonen, J. & Myllylä, R. 2014a. Tailoring the excitation of fundamental flexural guided waves in coated bone by phase-delayed array: two-dimensional simulations. J Acoust Soc Am submitted for publication.

Kilappa, V., Moilanen, P., Salmi, A., Zhao, Z., Haeggström, E., Timonen, J. & Myllylä, R. 2014b. Obstructing propagation of interfering modes improves detection of guided waves in coated bone models. 2014 IEEE International Ultrasonics Symposium Proceedings, 1332–1335.

Kilappa, V., Moilanen, P., Xu, L., Nicholson, P. H. F., Timonen, J. & Cheng, S. 2011a. Low-frequency axial ultrasound velocity correlates with bone mineral density and cortical thickness in the radius and tibia in pre- and postmenopausal women. Osteoporos Int 22 (4), 1103–1113.

Kilappa, V., Xu, K., Moilanen, P., Heikkola, E., Ta, D. & Timonen, J. 2011b. Assessment of the fundamental flexural guided wave in cortical bone by an ultrasonic axial-transmission array transducer. Ultrasound Med Biol 39 (7), 1223–1232.

Knapp, K. M., Blake, G. M., Spector, T. D. & Fogelman, I. 2004. Can the who definition of osteoporosis be applied to multi-site axial transmission quantitative ultrasound? Osteoporos Int 15, 367–374.

Knapp, K. M., Welsman, J. R., Hopkins, S. J., Fogelman, I. & Blake, G. M. 2012. Obesity increases precision errors in dual-energy x-ray absorptiometry measurements. J Clin Densitom 15 (3), 315–319.

Kärkkäinen, M., Tuppurainen, M., Salovaara, K., Sandini, L., Rikkonen, T., Sirola, J., Honkanen, R., Jurvelin, J., Alhava, E. & Kröger, H. 2010. Effect of calcium and vitamin d supplementation on bone mineral density in women aged 65-71 years: a 3-year randomized population-based trial (ostpre-fps). Osteoporos Int 21 (3), 2047–2055.

Lamb, H. 1917. On waves in an elastic plat. Proc Roy Soc London Series A 93, 114–128.

Langton, C. M., Palmer, S. B. & Porter, R. W. 1984. The measurement of broadband ultrasonic attenuation in cancellous bone. Eng Med 13, 89–91.

Laugier, P., Giat, P., Chappard, C., Roux, C. H. & Berger, G. 1997. Clinical assessment of the backscatter coefficient in osteoporosis. Proc IEEE Ultrason Symp, 1104–1105.

Laugier, P. 2008. Instrumentation for in vivo ultrasonic characterization of bone strength. IEEE Trans Ultrason Ferroelectr Freq Control 55 (6), 1179–1196.

LeBlanc, A. D., Spector, E. R., Evans, H. J. & Sibonga, J. D. 2007. Skeletal responses to space flight and the bed rest analog: A review. J Musculoskelet Neuronal Interact 7 (1), 33–47.

Lee, K. I., Coan, B. S. & Bouxein, M. L. 1997. Tibial ultrasound velocity measured in situ predicts the material properties of tibial cortical bone. Bone 21 (1), 119–125.

Lee, K. I., Coan, B. S. & Bouxein, M. L. 2004. Feasibility of bone assessment with leaky lamb waves in bone phantoms and bovine tibia. J Acoust Soc Am 115, 3210–3217.

Lefebvre, F., Deblock, Y., Capistron, P., Ahite, D. & Fabre, J. J. 2002. Development of a new ultrasonic technique for bone and biomaterials in vitro characterization. J Biomed Mater Res 63, 441–446.

Lindsay, R., Cosman, F., Lobo, R. A., Wash, B. W., Harris, S. T., Reagan, J. E., Liss, C. L., Melton, M. E. & Byrnes, C. A. 1999. Addition of alendronate to ongoing hormone replacement therapy in the treatment of osteoporosis: A randomized, controlled clinical trial. The Journal of Clinical Endocrinology & Metabolism 84 (9), 3076–3081.

Love, A. E. H. 1911. Some problems of geodynamics. London: Cambridge University Press.

Lowe, M. J. S. 1995. Matrix techniques for modeling ultrasonic waves in multilayered media. IEEE Trans Ultrason Ferroelectr Freq Control 42, 525–542.

Macdonald, H., Kontulainen, S., Petit, M., Janssen, P. & McKay, H. 2006. Bone strength and its determinants in pre- and early pubertal boys and girls. Bone 39, 598–608.

Manolagas, S. C. 2000. Birth and death of bone cells: Basic regulatory mechanisms and implications for the pathogenesis and treatment of osteoporosis. Endocrine reviews 21 (2), 115–137.

Maravic, M., Bihan, C. L., Landais, P. & Fardellone, P. 2005. Incidence and cost of osteoporotic fractures in france during 2001. a methodological approach by the national hospital database. Osteoporos Int 16 (12), 1475–1480.

Marks, R. 2011. Physical activity and hip fracture disability: a review. J Aging Res 741918.

Marshall, D., Johnell, O. & Wedel, H. 1996. Meta-analysis of how well measures of bone mineral density predict occurrence of osteoporotic fractures. BMJ 312 (7041), 1254–1259.

Martin, R. B. 1991. Determinants of the mechanical properties of bones. J Biomech 24 (Suppl 1), 79–88.

Miller, C. G., Herd, R. J., Ramalingam, T., Fogelman, I. & Blake, G. M. 1993. Ultrasonic velocity measurements through the calcaneus: which velocity should be measured? Osteoporos Int 3 (1), 31–35.

Minonzio, J. G., Talmant, M. & Laugier, P. 2010. Guided wave phase velocity measurement using multi-emitter and multi-receiver arrays in the axial transmission configuration. J Acoust Soc Am 127 (5), 2913–2919.

Moilanen, P., Kilappa, V., Nicholson, P. H. F., Timonen, J. & Cheng, S. 2004. Thickness sensitivity of ultrasound velocity in long bone phantoms. Ultrasound Med Biol 30 (11), 1517–1521.

Moilanen, P., Määttä, M., Kilappa, V., Xu, L., Nicholson, P. H. F., Alén, M., Timonen, J., Jämsä, T. & Cheng, S. 2013a. Discrimination of fractures by low-frequency axial transmission ultrasound in postmenopausal females. Osteoporos Int 24 (2), 723–730.

Moilanen, P., Nicholson, P., Kilappa, V., Timonen, J. & Cheng, S. 2006. Measuring guided waves in long bones: Modeling and experiments in free and immersed plates. Ultrasound Med Biol 33, 709–719.

Moilanen, P., Nicholson, P. H. F., Kilappa, V., Cheng, S. & Timonen, J. 2007a. Assessment of the cortical bone thickness using ultrasonic guided waves: Modelling and in vitro study. Ultrasound Med Biol 33, 254–262.

Moilanen, P., Nicholson, P. H. F., Kärkkäinen, T., Wang, Q., Timonen, J. & Cheng, S. 2003. Assessment of the tibia using ultrasonic guided waves in pubertal girls. Osteoporos Int 14, 1020–1027.

Moilanen, P., Salmi, A., Karppinen, P., Kilappa, V., Zhao, Z., Myllylä, R., Haeggström, E. & Timonen, J. 2013b. Photo-acoustic phase-delayed excitation of guided waves in coated bone phantoms. Joint UFFC, EFTF and PFM Symposium, 2080–2083.

Moilanen, P., Talmant, M., Bousson, V., Nicholson, P. H. F., Cheng, S., Timonen, J. & Laugier, P. 2007b. Ultrasonically determined thickness of long cortical bones: Two-dimensional simulations of in vitro experiments. J Acoust Soc Am 122 (3), 1818–1826.

Moilanen, P., Talmant, M., Kilappa, V., Nicholson, P. H. F., Cheng, S., Timonen, J. & Laugier, P. 2008. Modeling the impact of soft tissue on axial transmission measurements of ultrasonic guided waves in human radius. J Acoust Soc Am 124 (4), 2363–2373.

Moilanen, P., Talmant, M., Nicholson, P. H. F., Cheng, S., Timonen, J. & Laugier, P. 2007c. Ultrasonically determined thickness of long cortical bones: Three-dimensional simulations of in vitro experiments. J Acoust Soc Am 122 (4), 2439–2445.

Moilanen, P., Zhao, Z., Karppinen, P., Karppinen, T., Kilappa, V., Pirhonen, J., Myllylä, R., Haeggsrtöm, E. & Timonen, J. 2014. Photo-acoustic excitation and optical detection of fundamental flexural guided wave in coated bone phantoms. Ultrasound Med Biol 40, 521–531.

Moilanen, P. 2004. Ultrasonic guided wave measurements in bone. University of Jyväskylä, Department of Physics. Ph. D. Thesis.

Muller, M., Mitton, D., Moilanen, P., Bousson, V., Talmant, M. & Laugier, P. 2008. Prediction of bone mechanical properties using qus and pqct: Study of the human distal radius. Medical Engineering & Physics 30, 761?-767.

Muller, M., Moilanen, P., Bossy, E., Nicholson, P. H. F., Kilappa, V., Timonen, J., Talmant, M., Cheng, S. & Laugier, P. 2005. Comparison of three ultrasonic axial transmission methods for bone assessment. Ultrasound Med Biol 31 (5), 633–642.

Määttä, M., Moilanen, P., Timonen, J., Pulkkinen, P., Korpelainen, R. & Jämsä, T. 2014. Association between low-frequency ultrasound and hip fractures - comparison with dxa-based bmd. BMC Musculoskeletal Disorders 15, 208.

Määttä, M. 2009. Assessment of osteoporosis and fracture risk – axial transmission ultrasound and lifestyle-related risk factors. University of Oulu, Department of Medical Technology. Ph. D. Thesis.

Määttä, M. 2012. Assessment of osteoporosis and fracture risk. University of Oulu, Department of Medical Technology. Ph. D. Thesis.

Nguyen, N. D., Pongchaiyakul, C., Center, J. R., Eisman, J. A. & Nguyen, T. V. 2005. Identification of high-risk individuals for hip fracture: a 14-year prospective study. J Bone Miner Res 20 (11), 1921–1928.

Nguyen, T. V., Center, J. R. & Eisman, J. A. 2004. Bone mineral density-independent association of quantitative ultrasound measurements and fracture risk in women. J Bone Miner Res 15, 942–947.

Nicholson, P. H., Moilanen, P., Kärkkäinen, T., Timonen, J. & Cheng, S. 2002. Guided ultrasonic waves in long bones: modelling, experiment and in vivo application. Physiol Meas 23 (4), 755–768.

Nikitovic, M., Wodchis, W. P., Krahn, M. D. & Cadarette, S. M. 2013. Direct health-care costs attributed to hip fractures among seniors: a matched cohort study. Osteoporos Int 24 (2), 659–669.

Njeh, C. F., Fuerst, H. D., Glüer, C.-C. & Genant, H. K. 1999b. Quantitative Ultrasound: Assessment of Osteoporosis and Bone Status. CRC Press.

Njeh, C. F., Hans, D., Li, J., Fan, B., Fuerst, T., He, Y. Q., Tsuda-Futami, E., Lu, Y., Wu, C. Y. & Genant, H. K. 2000. Comparison of six calcaneal quantitative ultrasound devices: precision and hip fracture discrimination. Osteoporos Int 11 (12), 1051–1062.

Njeh, C. F., Hans, D., Wu, C., Kantorovich, E., Sister, M., Fuerst, T. & Genant, H. K. 1999a. An in vitro investigation of the dependence on sample thickness of the speed of sound along the specimen. Medical Engineering & Physics 21, 651–659.

Nurmi, I., Narinen, A., Luthje, P. & Tanninen, S. 2003. Cost analysis of hip fracture treatment among the elderly for the public health services: a 1-year prospective study in 106 consecutive patients. Arch Orthop Trauma Surg 123 (10), 551–554.

Orgee, J. M., Foster, H., McCloskey, E. V., Khan, S., Coombes, G. & Kanis, J. A. 1996. A precise method for the assessment of tibial ultrasound velocity. Osteoporos Int 6 (1), 1–7.

Padilla, F., Jenson, F. & Laugier, P. 2006. Estimation of trabecular thickness using ultrasonic backscatter. Ultrason Imag 28, 3–22.

Pakarinen, M., Raitanen, J., Kaaja, R. & Luoto, R. 2010. Secular trend in the menopausal age in finland 1997?2007 and correlation with socioeconomic, reproductive and lifestyle factors. Maturitas 66, 417–422.

Parker, M. & Johansen, A. 2006. Hip fracture. BMJ 333 (7557), 27–30.

Pavlakovic, A. M. 1998. Leaky Guided ultrasonic waves in NDT. Imperial College of Science, Technology and Medicine. Ph. D. Thesis.

Peterlik, H., Roschger, P., Klaushofer, K. & Fratzl, P. 2006. From brittle to ductile fracture of bone. Nat Mater 5 (1), 52–55.

Piscitelli, P., Tarantino, U., Chitano, G., Argentiero, A., Neglia, C., Agnello, N., Saturnino, L., Feola, M., Cell, M., Raho, C., Distante, A. & Brandi, M. L. 2011. Updated incidence rates of fragility fractures in italy: extension study 2002–2008. Clinical Cases in Mineral and Bone Metabolism 8 (3), 54–61.

Prevrhal, S., Fuerst, T., Fan, B., Njeh, C., Hans, D., Uffman, M., Srivastav, S. & Genant, H. K. 2001. Quantitative ultrasound of the tibia depends on both cortical density and thickness. Osteoporosis Int 12 (1), 28–34.

Radon, J. 1917. Uber die bestimmung von funktionen durch ihre integralwerte langs gewisser mannigfaltigkeiten. Ber. Saechsische Akad 29, 262.

Raum, K., Cleveland, R. O., Peyrin, F. & Laugier, P. 2006b. Derivation of elastic stiffness from site-matched mineral density and acoustic impedance maps. Phys Med Biol 51, 747–758.

Raum, K., Leguerney, I., Chandelier, F., Bossy, E., Talmant, M., Saied, A., Peyrin, F. & Laugier, P. 2005. Bone microstructure and elastic tissue properties are reflected in qus axial transmission measurements. Ultrasound Med Biol 31, 1225–1235.

Raum, K., Leguerney, I., Chandelier, F., Talmant, M., Saied, A., Peyrin, F. & Laugier, P. 2006a. Site-matched assessment of structural and tissue properties of cortical bone using scanning acoustic microscopy and synchrotron radiation μct. Phys Med Biol 51, 733–746.

Rayleigh, J. W. S. 1885. On waves propagated along the plane surface of an elastic solid. Proc London Mat Soc 17 (1), 4–11.

Rebillard, X., Soulie, M., Chartier-Kastler, E., Davin, J.-L., Mignard, J.-P., Moreau, J.-L. & Coulange, C. 2008. High-intensity focused ultrasound in prostate cancer; a systematic literature review of the french association of urology. BJU Int 101 (10), 1205–1213.

Reginster, J. Y., Dethor, M., Pirenne, H., Dewe, W. & Albert, A. 1998. Reproducibility and diagnostic sensitivity of ultrasonometry on the phalanges to assess osteoporosis. Gynecology & Obstetrics 63, 21–28.

Riekkinen, O., Hakulinen, M. A., Lammi, M. J., Jurvelin, J. S., Kallioniemi, A. & Töyräs, J. 2007. Acoustic properties of trabecular bone – relationships to tissue composition. Ultrasound Med Biol 33, 1438–1444.

Riekkinen, O., Hakulinen, M. A., Töyräs, J. & Jurvelin, J. S. 2008. Dual-frequency ultrasound – new pulse-echo trechnique for bone densitometry. Ultrasound Med Biol 34 (10), 1703–1708.

Rose, J. L. 1999. Ultrasonic waves in solid media. Cambridge, UK: Cambridge University Press.

Rosen, C. R. 2004. Anatomy, physiology and disease *in C. M. Langton and C. F. Njeh, eds.* The Physical Measurement of Bone. Bristol, UK: Institute of Physics Publishing.

Royer, D. & Dieulesaint, E. 2000. Elastic Waves in Solids I. Berlin Heidelberg 2000, Germany: Springer-Verlag.

Sarvazyan, A., Tatarinov, A., Egorov, V., Airapetian, S., Kurtenok, V. & Gatt, C. J. 2009. Application of the dual-frequency ultrasonometer for osteoporosis detection. Ultrasonics 49, 331–337.

Sasso, M., Haïat, G., Yamato, Y., Naili, S. & Matsukawa, M. 2008. Dependence of ultrasonic attenuation on bone mass and microstructure in bovine cortical bone. Journal of Biomechanics 41, 347–355.

Seeman, E. & Delmas, P. D. 2006. Bone quality – the material and structural basis of bone strength and fragility. N Engl J Med 354 (21), 2250–2361.

Seeman, E. 2003. Invited review: Pathogenesis of osteoporosis. J Appl Physiol 95, 2142–2151.

Seeman, E. 2008. Bone quality: the material and structural basis of bone strength. J Bone Miner Metab 26 (1), 1–8.

Seghal, C. M. & Greenleaf, J. F. 1984. Scattering of ultrasound by tissues. Ultrason Imag 6, 60–80.

Selfridge, A. R. 1985. Bone quality – the material and structural basis of bone strength and fragility. IEEE Transactions on Sonics and Ultrasonics 32 (3), 381–394.

Siegel, I. M., Anast, G. T. & Fields, T. 1958. The determination of fracture healing by measurement of sound velocity across the fracture site. Surg Gynec Obstet 107, 327–332.

Sievänen, H., Cheng, S., Ollikainen, S. & Uusi-Rasi, K. 2001. Ultrasound velocity and cortical bone characteristics in vivo. Osteoporos Int 12 (5), 399–405.

Siu, W. S., Qin, L. & Leung, K. S. 2003. pqct bone strength index may serve as a better predictor than bone mineral density for long bone breaking strength. J Bone Miner Metab 21, 316–322.

Snedecor, G. W. 1976. Statistical methods (6th edition). Ames, Iowa, USA: The Iowa State University Press.

Stegman, M. R., Heaney, R. P., Travers-Gustafson, D. & Leist, J. 1995. Cortical ultrasound velocity as an indicator of bone status. Osteoporosis International 5, 349–353.

Stegman, M. R., Recker, R. R., Davies, K. M., Ryan, R. A. & Heaney, R. P. 1996. Fracture risk as determined by prospective and retrospective study designs. Osteoporosis International 2, 290–297.

Stein, E. M., Rosete, F., Young, P., Kamanda-Kosseh, M., McMahon, D. J., Luo, G. M., Kaufman, J. J., Shane, E. & Siffert, R. S. 2013. Clinical assessment of the 1/3 radius using a new desktop ultrasonic bone densitometer. Ultrasound Med Biol 39 (3), 388–395.

Stone, K. L., Seeley, D. G., Lui, L. Y., Cauley, J. A., Ensrud, K., Browner, W. S., Nevitt, M. C., Cummings, S. R. & 2003, O. F. R. G. 2003. Bmd at multiple sites and risk of fracture of multiple types: long-term results from the study of osteoporotic fractures. J Bone Miner Res 18 (11), 1947–1954.

Stoneley, R. 1924. Elastic waves at the surface of separation between two solids. Proc Roy Soc London Series A 106 (738), 416–428.

Sund, R., Juntunen, M., Lüthje, P., Huusko, T. & Häkkinen, U. 2011. Monitoring the performance of hip fracture treatment in finland. Ann Med 43 (Suppl 1), 39–46.

Ta, D., Huang, K., Wang, W., Wang, Y. & Le, L. H. 2006. Identification and analysis of multimode guided waves in tibia cortical bone. Ultrasonics 44, 279–284.

Ta, D., Wang, W., Wang, Y., Le, L. H. & Zhou, Y. 2009. Measurement of the dispersion and attenuation of cylindrical ultrasonic guided waves in long bone. Ultrasound Med Biol 35 (4), 641–652.

Talmant, M., Kolta, S., Roux, C., Haguenauer, D., Vedel, I., Cassou, B., Bossy, E. & Laugier, P. 2009. In vivo performance evaluation of bi-directional ultrasonic axial transmission for cortical bone assessment. Ultrasound Med Biol 35 (6), 912–919.

Tang, B. M. P., Eslick, G. D., Nowson, C., Smith, C. & Bensoussan, A. 2007. Use of calcium or calcium in combination with vitamin d supplementation to prevent fractures and bone loss in people aged 50 years and older: a meta-analysis. Lancet 370, 657–666.

Tarantino, U., Cannataa, G., Lecce, D., Celi, M., Cerocchi, I. & Iundusi, R. 2008. Incidence of fragility fractures. Aging clinical and experimental research 19 (4 suppl), 7–11.

Tatarinov, A. & Sarvazyan, A. 2008. Topography of acoustical properties of long bones: From biomechanical studies to bone health assessment. IEEE Trans Ultrason Ferroelec Freq Control 55 (6), 1287–1297.

Tatarinov, A., Sarvazyan, N. & Sarvazyan, A. 2005. Use of multiple acoustic wave modes for assessment of long bones: model study. Ultrasonics 43 (8), 672–680.

Tran, T. N. H. T., Stieglitz, L., Gu, Y. J. & Le, L. H. 2013. Analysis of ultrasonic waves propagating in a bine plate over a water half-space with and without overlying soft tissue. Ultrasound Med Biol 39 (12), 2422–2430.

Turner, C. H., Wang, T. & Burr, D. B. 2001. Shear strength and fatigue properties of human cortical bone determined from pure shear tests. Calcified Tissue International 69 (6), 373–378.

Turner, C. H. 2006. Bone strength: Current concepts. Ann N Y Acad Sci 1068, 429-446.

Viktorov, I. A. 1967. Rayleigh and Lamb Waves - Physical Theory and Application. Moscow: Acoustics Institure, Academy of Sciences of the USSR.

Völgyi, E., Tylavsky, F. A., Xu, L., Lu, J., Wang, Q., Alén, M. & Cheng, S. 2010. Bone and body segment lengthening and widening: a 7-year follow-up study in pubertal girls. Bone 47, 773–782.

Wang, Q., Nicholson, P. H. F., Timonen, J., Alen, M., Moilanen, P., Suominen, H. & Cheng, S. 2008. Monitoring bone growth using quantitative ultrasound in coparison with DXA and pQCT. J Clin Densitom 11 (2), 295–301.

Wang, X., Shen, X., Li, X. & Agrawal, C. M. 2002. Age-related changes in the collagen network and toughness of bone. Bone 31 (1), 1–7.

Wasnich, R. D., Ross, P. D., Heilbrun, L. K. & Vogel, J. M. 1987. Selection of the optimal skeletal site for fracture risk prediction. Clin Orthop 216, 262–269.

Wasnich, R. D. 1999. Epidemology of osteoporosis *in M. J. Famus, ed.* Primer on the Metabolic Bone Diseases and Disorders of Mineral Metabolism. Lippincott, Williams and Wilkins.

Wear, K. & Armstrong, D. W. 2000. The relationship between ultrasonic backscatter and bone mineral density in human calcaneus. IEEE Trans Ultrason Ferroelect Freq Control 47, 777–780.

Wear, K. & Garra, B. S. 1998. Assessment of bone density using ultrasonic backscatter. Ultrasound Med Biol 24 (5), 689–695.

Wear, K. & Laib, A. 2003. The relationship between ultrasonic scattering and micro-architecture in human calcaneus. IEEE Trans Ultrason Ferroelect Freq Control 50, 979–986.

Weiss, M., Ben-Shlomo, A. B., Hagag, P. & Rapoport, M. 2000. Reference database for bone speed of sound measurement by a novel quantitative multi-site ultrasound device. Osteoporos Int 11, 688–696.

Xu, K., Ta, D. & Wang, W. 2010. Multiridge-based analysis for separating individual modes from multimodal guided wave signals in long bones. IEEE Trans Ultrason Ferroelectr Freq Control 57 (11), 2480–2490.

Xu, L., Nicholson, P. H. F., Wang, Q., Alen, M. & Cheng, S. 2009. Bone and muscle development during puberty in girls: a seven-year longitudinal study. J Bone Miner Res 24 (10), 1693–1698.

Y. Hasegawa, P. S. & Reiners, C. 2001. Age, sex, and gripstrength determine architectural bone parameters assessed by peripheral quantitative computed tomography (pqct) at the human radius. Journal of Biomechanics 34, 497–503.

Yapura, C. L. & Kinra, V. K. 1995. Guided waves in a fluid-solid bilayer. Wave Motion 21, 35–46.

Zebaze, R. M., Ghasem-Zadeh, A., Bohte, A., Iuliano-Burns, S., Miriams, M., Price, R. I., Mackie, E. J. & Seeman, E. 2010. Intracortical remodelling and porosity in the distal radius and post-mortem femurs of women: a cross-sectional study. Lancet 375 (9727), 1729–1736.

Zethraeus, N., Stromberg, L., Jonsson, B. & ang G. Ohlen, O. S. 1997. The cost of a hip fracture. estimates for 1709 patients in sweden. Acta Orthop Scand 68 (1), 13–17.

American College of Radiology 2008. ACR Practice Guideline for the Performance of Quantitative Computed Tomography (QCT) Bone Densitometry. American College of Radiology.

WHO Scientific Group 2003. Prevention and Management of Osteoporosis, Report of a WHO Scientific Group. Geneva: World Health Organisation. WHO Technical Report Series No. 921.

ORIGINAL PAPERS

I

LOW-FREQUENCY AXIAL ULTRASOUND VELOCITY MEASUREMENTS IN CHILDREN AND ADULTS: CORRELATIONS WITH BONE MINERAL DENSITY AND CORTICAL THICKNESS IN THE RADIUS AND TIBIA

by

V. Kilappa, P. Moilanen, L. Xu, P. H. F. Nicholson, J. Timonen, S. Chen 2011

Osteoporos Int, 22(4):1103

II

DISCRIMINATION OF FRACTURES BY LOW-FREQUENCY AXIAL TRANSMISSION ULTRASOUND IN POSTMENOPAUSAL FEMALES

by

P. Moilanen, M. Määttä, V. Kilappa, L. Xu, P. H. F. Nicholson, M. Alén, J. Timonen, T. Jämsä, S. Cheng 2013

Osteoporos Int, 24(2):723–730

III

ASSESSMENT OF THE FUNDAMENTAL FLEXURAL GUIDED WAVE IN CORTICAL BONE BY AN ULTRASONIC AXIAL-TRANSMISSION ARRAY TRANSDUCER

by

V. Kilappa, K. Xu, P. Moilanen, E. Heikkola, D. Ta, J. Timonen 2013

Ultrasound Med Biol, 39(7):1223–1232

IV

TAILORING THE EXCITATION OF FUNDAMENTAL FLEXURAL GUIDED WAVES IN COATED BONE BY PHASE-DELAYED ARRAY: TWO-DIMENSIONAL SIMULATIONS

by

V. Kilappa, P. Moilanen, A. Salmi, Z. Zhao, E. Haeggström, J. Timonen, R. Myllylä 2014

submitted for publication